UC Berkeley
UC Berkeley Electronic Theses and Dissertations

Title

First-principles studies of complex functional oxides and chalcogenides

Permalink

https://escholarship.org/uc/item/8pv5b9qx

Author

Peterson, Elizabeth

Publication Date

2022

Peer reviewed|Thesis/dissertation

eScholarship.org Powered by the California Digital Library
University of California

First-principles studies of complex functional oxides and chalcogenides

By

Elizabeth Peterson

A dissertation submitted in partial satisfaction of the

requirements for the degree of

Doctor of Philosophy

in

Physics

in the

Graduate Division

of the

University of California, Berkeley

Committee in charge:

Professor Jeffrey B. Neaton, Chair
Professor Steven G. Louie
Professor Mark Asta

Spring 2022

First-principles studies of complex functional oxides and chalcogenides

Copyright 2022
by
Elizabeth Peterson

Abstract

First-principles studies of complex functional oxides and chalcogenides

by

Elizabeth Peterson

Doctor of Philosophy in Physics

University of California, Berkeley

Professor Jeffrey B. Neaton, Chair

The development of the physical principles underlying novel materials to power the technological needs of the modern world is dependent on having a detailed knowledge of the electronic and structural properties of these materials. First-principles electronic structure theory methods are used here to calculate the structural and electronic properties of complex functional materials with an eye toward applications in artificial photosynthesis and "Beyond Moore's Law" information technology. The details of the methods employed are discussed in Chapter 2.

Artificial photosynthesis, the photocatalytic conversion of water and carbon dioxide into solar fuels such as hydrogen gas and hydrocarbons, is a critical technology for future green energy applications. There are numerous challenges to be overcome in the development of high performing photocatalyst materials. Here, first-principles calculations are used to understand and tune the electronic structure of complex materials for artificial photosynthesis catalysis, in particular ternary metal oxides and layered two-dimensional materials.

- In Chapter 3 we present the results of an experimental collaboration investigating n-type $FeWO_4$ as a high photovoltage photoanode material. We perform electronic structure calculations to shed light on the potential mechanism driving this high photovoltage.
- In Chapter 4 we perform absolute band edge energy calculations on a series of $MoS_{2(1-x)}Se_{2x}$ alloys to corroborate the results obtained from experimental collaborators. We find that the band edges of these alloys can be tuned between the band edges of pristine MoS_2 and those of pristine $MoSe_2$ when the alloys assume certain crystal structures. We identify one form of these alloys that does not behave as expected upon incorporation of Se into MoS_2 and perform a deeper analysis of the properties of these systems.

- In Chapter 5 we study the effect that biaxial in-plane and uniaxial out-of-plane strain have on heterostructures of monolayer Janus WSSe and monolayer ZnO, both polar materials. We find that the absolute band edges of these heterostructures can be tuned to higher and lower energies via application of different types of strain.

Quantum information is a broad field that encompasses novel ways of storing information, both via beyond-transistors forms of storing binary quantities and via quantum computing. Here, first-principles calculations are performed to study two-dimensional materials for use in valleytronics and in tunable exchange bias.

- In Chapter 6 we develop general design principles for maximizing valley splitting in transition metal dichalcogenides (TMDs) via magnetic substrates. We perform a systematic analysis of the effects of proximity, alignment, and magnetic moment of the magnetic ions in a magnetic substrate and the degree to which these factors affect the magnitude of the calculated valley splitting. We then develop a superexchange model to rationalize these calculated values and elucidate the mechanism driving valley splitting in TMDs via magnetic substrates.
- In Chapter 7 we study the magnetic ordering of a novel, layered metal-organic framework that our experimental collaborators found to exhibit tunable exchange bias. Our calculations support the experimental results indicating that this material is a frustrated antiferromagnet and is a spin glass at low temperatures.

Finally, an overview and outlook are provided in Chapter 8.

To the girls who raise their hands

Contents

Contents **ii**

List of Figures **v**

List of Tables **xii**

1 Introduction **1**

2 Methods **7**
2.1 Density Functional Theory 7
2.2 Exchange-correlation Functionals 9
2.3 Hubbard U Corrections 10
2.4 Hybrid Functionals 11
2.5 van der Waals Dispersion Forces 12
2.6 Kohn-Sham Electronic Structure 13
2.7 Basis Functions 13
2.8 Pseudopotentials 14
2.9 Relativistic Effects 16
2.10 Supercells for Low-Dimensional Materials 17
2.11 Electrostatic Potential and Absolute Band Edge Calculations 19
2.12 Phonon Calculations 21
2.13 Codes 22

3 High photovoltage and oxygen vacancies in n-type $FeWO_4$ **23**
3.1 Introduction to Oxide Photoanodes 23
3.2 Photovoltage 24
3.3 Experimental Results 25
3.4 Electronic Structure Calculations 27
3.5 Nonequilibrium Synthesis 29
3.6 Outlook 32

4 Band edge tuning of few-layer $MoS_{2(1-x)}Se_{2x}$ alloys for carbon dioxide reduction catalysis **33**

4.1 Introduction . . . 33
4.2 Experimental Results . . . 35
4.3 Crystal Structure Candidates . . . 35
4.4 Electronic Structure and Absolute Band Edges . . . 37
4.5 Interfacial Dipole Effects in Small Domains . . . 39
4.6 Outlook . . . 43

5 Band edge tuning of Janus WSSe-ZnO heterostructures 44
5.1 Introduction . . . 44
5.2 Electronic Structure Methods . . . 46
5.3 Crystal Structures . . . 48
5.4 In-plane Biaxial Strain and Out-of-plane Uniaxial Strain . . . 50
5.5 Electric Field . . . 59
5.6 Photocatalytic Applications . . . 60
5.7 Outlook . . . 62
5.8 Appendix I: Comparison of band structures at PBE and HSE levels of theory 64
5.9 Appendix II: Phonon band structures and energetics of strained heterostructures 65
5.10 Appendix III: Band edge alignment to HER and OER redox potentials for varying pH . . . 67
5.11 Appendix IV: Band gaps of Janus TMD-ZnO heterostructures with an applied out-of-plane electric field . . . 69

6 Superexchange-induced valley splitting in two-dimensional transition metal dichalcogenides 70
6.1 Introduction to Valley Splitting . . . 70
6.2 Electronic Structure Methods . . . 71
6.3 Model TMD+Fe Monolayer System Band Structure and Eigenvalues . . . 73
6.4 Calculated Valence Band Splitting . . . 76
6.5 Superexchange Model Hamiltonian . . . 79
6.6 General Design Principles for Valleytronics Interfaces . . . 83
6.7 Model System: WSe_2+(111)-$BiFeO_3$ . . . 84
6.8 Outlook . . . 86
6.9 Appendix I: Effects of Hubbard U on Valley Splitting Calculations . . . 87
6.10 Appendix II: Calculated Valence Band Eigenvalues . . . 88
6.11 Appendix III: Justification for taking perturbative approach to second order 89
6.12 Appendix IV: Derivation of Canted Spin VB Splitting . . . 90

7 Exchange bias in a 2D metal-organic framework spin glass 94
7.1 Introduction . . . 94
7.2 Exchange Bias . . . 95
7.3 Experimental Results . . . 96

7.4 First-principles calculations 97
7.5 Outlook 100

8 Conclusions and Outlook **102**

Bibliography **104**

List of Figures

1.1 Schematic summarizing key processes underlying artificial photosynthesis. Photoexcited holes at a material's surface catalyze oxidation reactions, such as the oxidation of water to O_2 gas, and photoexcited electrons at a material's surface catalyze reduction reactions, such as the reduction of protons to H_2 gas or the reduction of CO_2 to hydrocarbons. 2
1.2 Crystal structures of various 2D and layered materials discussed in this dissertation. (a) Side view of a bulk MX_2 TMD, with layers held together by vdW dispersion forces instead of chemical bonds. (b) Top view of a monolayer MX_2 TMD, exhibiting the bipartite hexagonal lattice. (c) Top view of monolayer ZnO, discussed in Chapter 5. (d) Side view of Janus WSSe, discussed in Chapter 5. (e) Top view of $Mn_3(C_6S_6)$, discussed in Chapter 7. 5

2.1 A supercell of a monolayer TMD with a large vacuum region above the monolayer to reduce spurious interactions between periodically repeated monolayers in the c-direction. 17
2.2 The band structure of MoS_2 calculated (a) without and (b) with vdW dispersion corrections. The valence band maximum is marked with a green circle and the conduction band minimum is marked with a red circle. The band structure calculated without dispersion corrections erroneously exhibits an indirect band gap. 19
2.3 The plane-averaged electrostatic potential of a monolayer TMD along the c-axis direction, with the relevant crystal structure for reference. The energy scale has been shifted so that the electrostatic potential is 0 in the vacuum region. The difference between the vacuum region electrostatic potential and the valence band maximum (VBM) is taken to be the absolute position of the VBM. 20

3.1 Schematic of flat band potentials (left), band bending at the surface of an n-type material (middle), and photoexcited carrier induced band unbending, with the degree of band unbending indicated as the photovoltage ΔV (right). 25
3.2 Photocurrent measurements of Fe-W-Bi combinatorial library by (a) position space and (b) composition space. Reproduced from [1]. 26

3.3 Turn-on potential of $Fe_{0.56}W_{0.38}Bi_{0.06}O_z$ sample in the light (solid lines) and in the dark (dashed lines) and with (SLF9) and without (OER9) a sacrificial hole acceptor at pH=9. Reproduced from [1]. 26
3.4 The crystal structure of $FeWO_4$ and the two magnetic configurations considered in first-principles calculations (a) FM and (b) AFM. Fe ions are gold, W ions are silver, and O ions are red. 28
3.5 The band structures of $FeWO_4$ in the (a) FM and (b) AFM magnetic configurations. In both cases, the bands are relatively flat with minimal dispersion. . . . 29
3.6 The element-projected density of states of $FeWO_4$ in the (a) FM and (b) AFM magnetic configurations. In both cases the VB is characterized by localized Fe states and the CB is characterized by localized W states. 30
3.7 The energy above hull of Fe-W oxides at 883 K at varying partial pressures of oxygen gas. At higher partial pressures of oxygen Fe_2O_3 and WO_3 are the most energetically stable whereas at very low partial pressures of oxygen $FeWO_4$ is the most energetically stable. 31

4.1 Absolute band edge positions of several TMDs relative to vacuum. The pH=0 redox potentials for the oxygen evolution reaction and hydrogen evolution reaction are indicated with red dashed lines. The redox potentials for reduction of CO_2 to various hydrocarbons are indicated as well. Note that under operating conditions these redox potentials will fall at different energies depending on many factors such as pH. This figure and the reported band edge energies are adapted from [12]. 34
4.2 Schematic of $MoS_{2(1-x)}Se_{2x}$ alloy synthesis procedure. (a) Few-layer MoS_2 was synthesized and Se was then substitutionally incorporated into S sites. (b) The Se substitution in MoS_2 was performed by using gas to sprinkle Se powder onto the few-layer MoS_2 sample. (c) The experimentally measured band edges. This figure is reproduced from [89]. 36
4.3 Schematics of three different candidate $MoS_{2(1-x)}Se_{2x}$ alloy crystal structures (a) lateral heterostructures with small domains of $MoSe_2$ (b) vertical heterostructures with Se only substituted on the top layers (c) homogeneous alloys with Se homogeneously distributed throughout the crystal. The calculated absolute band edges of each of these three candidate crystal structures are shown in (d), (e), and (f) respectively. This figure is reproduced from [89]. 38
4.4 The experimental band edges of MoS_2 and $MoSe_2$, the expected naive band edge positions, and the actual calculated band edges of the small lateral domain structure with 15% Se content, with empirical corrections. Red bars represent dominant contributions from MoS_2 at the indicated band edge, blue bars represent dominant contributions from $MoSe_2$, and purple bars represent mixed contributions from both regions. Dashed lines indicate the positions of the experimental band edges for each pristine TMD for visual clarity and to emphasize the discrepancy between the calculated values and the expected band edges. 39

4.5 The square of the wavefunction at the VBM and CBM of a small lateral domain heterostructure. (a) The VBM is distributed throughout both regions of the heterostructure. (b) The CBM is localized in the $MoSe_2$ region. 40
4.6 The band edges of $MoSe_2$ at varying degrees of in-plane biaxial strain. On the right $MoSe_2$ has its equilibrium lattice parameters. On the left, the lattice parameters have been compressed to those of MoS_2. 41
4.7 Calculation of the dipole moment across the MoS_2/$MoSe_2$ interface. (a) Each Mo site on which the on-site electrostatic potential is calculated. (b) The on-site electrostatic potential for each Mo site along the diagonal for the heterostructure with 10% Se, indicating a change that occurs as the interface is crossed. Representative MoS_2, Interface, and $MoSe_2$ regions are indicated with labelled yellow bars. 42

5.1 Stacking configurations of Janus WSSe-ZnO heterostructures. (a) Side view with Se on the same side as ZnO (AB-I-Se). The buckling Δz in ZnO gives rise to its dipole moment. (b) Top view in Type I registry with AB stacking with W and Zn aligned and Se on the same side as ZnO (AB-I-Se) (c) Top view in Type II registry with AB stacking with W and O aligned and Se on the same side as ZnO (AB-II-Se). 47
5.2 The phonon band structures of the three stacking configurations with the largest binding energies (a) AB-I-S (WSeS-ZnO), (b). AB-I-Se (WSSe-ZnO), and (c) AB-II-Se. AB-II-Se exhibits imaginary optical modes indicating that the structure is not stable. 49
5.3 The effect of biaxial in-plane strain on the buckling in monolayer ZnO. (a) Magnitude of the buckling (Δz) in ZnO layer as a function of in-plane biaxial strain for the two heterostructures studied, calculated as the difference between the Cartesian z-position of the O ion and that of the Zn ion. (b) Magnitude of the electrostatic potential energy difference across a monolayer of ZnO for each buckling value and a linear fit (black line). (c) Schematic of the difference of the Cartesian z-positions of the O ion and the Zn ion, with Δz corresponding to the Zn-O buckling values. 52
5.4 Band structures of the Janus TMD-ZnO heterostructures for WSSe-ZnO (a,b,c) and WSeS-ZnO (d,e,f) at 5% compressive strain (a,d), no strain (b,e), and 5% tensile strain (c,f). The orbital projections are color coded so that orbitals with more WSSe character are purple and those with more ZnO character are yellow, as indicated by the color bars. 53

5.5 Schematics of band edge alignments under in-plane biaxial strain. Band edge alignment of monolayer WSSe on the (a) Se side and (b) the S side. Band edge alignment of WSSe-ZnO on the (d) Se/ZnO side and (e) S/WSSe side. Band edge alignment of WSeS-ZnO on the (g) S/ZnO side and (h) Se/WSSe side. Schematics of (c) monolayer WSSe, (f) WSSe-ZnO and (i) WSeS-ZnO with labels indicating what Se side, S side, ZnO side and WSSe side refer to. Green or yellow bars indicate that the band edges are calculated from the electrostatic potential relative to the vacuum level on the Se side or S side of WSSe respectively. The redox potentials for the hydrogen evolution reaction and the oxygen evolution reaction at pH=0 are indicated in red lines. The potentials for pH=7 and pH=14 are shown in Appendix III Figure 5.12. 55
5.6 Electrostatic potential differences across WSSe, ZnO, and the heterostructures under study. (a) The electrostatic potential difference between the ZnO (or top) side and WSSe (or bottom) side of monolayer WSSe, monolayer ZnO, and the two most stable stacking configurations WSSe-ZnO and WSeS-ZnO. Compressive strain tends to make the electrostatic potential difference more negative. (b) The electrostatic potential difference between the ZnO side and WSSe side of the two most stable stacking configurations as a function of displacement of the ZnO from the equilibrium separation. Vertical compression tends to make the electrostatic potential difference more positive. 56
5.7 Summaries of band edge alignments under out-of-plane uniaxial strain. Band edge alignment of the most stable stacking configurations on the ZnO side of the heterostructure (a,b) and the WSSe side of the heterostructure (c,d) for (a,c) WSSe-ZnO and (b,d) WSeS-ZnO as a function of the vertical displacement of the ZnO relative to the equilibrium separation of ZnO and WSSe in each heterostructure. ZnO side and WSSe side are defined as in Figure 5.5f,i. Green or yellow bars indicate that the band edges are calculated from the electrostatic potential relative to the vacuum level on the Se side or S side of WSSe respectively. The redox potentials for the hydrogen evolution reaction and the oxygen evolution reaction at pH=0 are indicated in red lines. The potentials for pH=7 and pH=14 are shown in Appendix III Figure 5.13. 58
5.8 Band structures with orbital projections of WSSe and ZnO for WSSe-ZnO calculated via (a) HSE and (b) PBE. Similarly, band structures of WSeS-ZnO calculated via (c) HSE and (d) PBE. In both cases, the HSE band structures exhibit Type I band alignment and the PBE band structures exhibit Type II band alignment. 64
5.9 Phonon band structures of the WSeS-ZnO heterostructure under (a) 0% (b) 1% and (c) 5% in-plane biaxial compressive strain. The structures under biaxial compressive strain exhibit phonon modes with imaginary frequencies indicating a lack of dynamical stability. The imaginary modes are primarily confined to the ZnO layer, indicating that while WSSe is stable under biaxial compressive strain, ZnO is not stable under biaxial compressive strain. 65

5.10 The phonon band structures of the WSeS-ZnO heterostructure under out-of-plane uniaxial compressive strain at (a) the equilibrium vertical separation (b) 0.5 Å of vertical compression and (c) 2 Å of vertical compression. For small amounts of vertical compression the heterostructure exhibits dynamical stability, however at larger amounts of vertical compression the heterostructure becomes structurally unstable. 66
5.11 The energy per atom of Janus TMD-ZnO heterostructures as a function of vertical displacement, represented as a percent on the x axis with inset numerals indicating the number of Å by which the vertical separation differs from the equilibrium separation. There is a large energy barrier to vertical compression beyond 30% decrease in the vertical separation. 66
5.12 Reproduction of Figure 5.5. The redox potentials for the hydrogen evolution reaction and the oxygen evolution reaction at pH=0, 7, and 14 are indicated in purple, pink, and orange respectively with the hydrogen evolution potentials indicated by solid lines and the oxygen evolution potentials indicated by dashed lines. 67
5.13 Reproduction of Figure 5.7. The redox potentials for the hydrogen evolution reaction and the oxygen evolution reaction at pH=0, 7, and 14 are indicated in purple, pink, and orange respectively with the hydrogen evolution potentials indicated by solid lines and the oxygen evolution potentials indicated by dashed lines. 68

6.1 (a) Side and top view of a monolayer TMD crystal structure with the transition metal in turquoise and the chalcogen in yellow (b) Diagram of hexagonal 2D Brillouin zone (c) Spin-valley coupled valence and conduction bands at K and K' without (left) and with (right) time-reversal symmetry breaking because of a magnetic field (yellow arrow) or magnetic substrate. 72
6.2 (a) The band structure of pristine WSe_2 with the spin character of W in each state indicated in red and blue for positive and negative respectively (b) The band structure of WSe_2 with 100% coverage of Fe atoms that are 4.4 Å above the W atom, with valley splitting clearly visible. (c) The band structure of WSe_2 with 33% coverage of Fe atoms that are 4.4 Å above the W atom, with K and K' folded into Γ (d) Schematic of Fe atoms above TMD monolayer indicating x and z displacements (e) Schematic of Fe atoms above TMD monolayer at 100% coverage (left) and 33% coverage (right). 74
6.3 Spherical harmonics projections on the band structure of WSe_2. (a) Spherical harmonics projections $|\langle Y_l^m | n\mathbf{k}\sigma\rangle|^2$ centered on W sites, Y_2^{+2} in green, Y_2^{-2} in magenta and Y_2^0 in yellow. (b) Spherical harmonics projections for Se orbitals. Y_1^{+1} in orange and Y_1^{-1} in blue. Some mixing occurs in the conduction band at K', however the dominant contribution comes from Y_1^{+1} 75

6.4 DFT-PBE Valley splitting (Eq. 6.1) for WSe_2 + Fe at 100% coverage (red) and difference between valley splitting (band gap split) and valence band splitting (Eq. 6.4) (black). The difference between the valley splitting and the valence band splitting is generally less than 5 meV and for the closest separations (< 4.5 Å) the difference is less than 10%. 76
6.5 (a) Schematic illustrating definition of the valence band (VB) splitting (b) Valence band splitting of WSe_2 and MoS_2 with Fe atom at 100% and 33% coverage at variable Fe-W separations z. Circles and triangles are data points, solid lines are exponential fits. (c) Valence band splitting of WSe_2 and MoS_2 with Fe atom at 100% coverage with variable lateral position x and with z fixed at 4.4 Å. Lateral position is represented here as a fractional position along the a-axis (x/a) following the direction of the a-axis displayed in (Figure 6.1a). Circles are data points, solid lines are fits to cosines. (d) Schematic of canted Fe atom spin and definition of z component of magnetic moment. (e) Valence band splitting of WSe_2 and MoS_2 at 100% coverage with the magnetic moment of the Fe atom at variable angles with respect to the c axis, causing the z component of the magnetic moment to take different values. Circles are data points, solid lines are linear fits. (f) Valence band splitting of WSe_2 in the presence of different magnetic atoms, Fe, Cr and Zn. Circles are data points, solid lines are exponential fits. 77
6.6 (a) Schematic of spin-orbit coupling (SOC) splitting at K and K' of TMD valence bands in the presence of Fe atom (b) Change in SOC splitting at K and K' relative to no Fe system for WSe_2+Fe atom system at 100% coverage and Fe directly above W with interpolation between data points. The absolute value of the SOC splitting in the absence of Fe is 459 meV. (c) Change in SOC splitting at K and K' relative to no Fe system for MoS_2+Fe atom system at 100% coverage and Fe directly above Mo. The absolute value of the SOC splitting in the absence of Fe is 146 meV. 79
6.7 (a) Valence band splitting for WSe_2 and MoS_2 for 100% coverage and 33% coverage (with the Fe atoms positioned directly on top of the W and Mo atoms), same as Fig. 6.5b, and fits to the valence band splitting model (b) Fitted values of effective exchange J arising from the superexchange interaction for WSe_2 and MoS_2 for 100% and 33% coverage. 82
6.8 The crystal structure of a WSe_2+(111)-$BiFeO_3$ with (a) the experimentally observed magnetic ordering and O termination and (b) the fictitious version of (111)-$BiFeO_3$ with out-of-plane magnetic ordering and Fe termination. The definition of z, the separation between W and Fe ions is indicated in (b). W ions are turquoise, Se ions are yellow, Fe ions are brown, Bi ions are purple, and O ions are red. 85
6.9 The calculated valley splitting in the fictitious WSe_2+(111)-$BiFeO_3$ heterostructure as a function of (a) vertical proximity and (b) out-of-plane magnetic moment. The valley splitting at the equilibrium separation is indicated with the purple circle in (a). 85

6.10 (a) Valence band splitting of WSe_2 with 100% coverage of Fe atoms at fixed 4.4 Å Fe-W separation as a function of effective Hubbard U. (b) Corresponding magnetic moment of Fe atom as a function of effective Hubbard U. (c) Element-specific orbital projected band structures of WSe_2+Fe with various Hubbard U values applied to the d states of Fe. 87
6.11 (a) Schematic of valence band eigenvalues measured relative to the Fermi energy (b) Variation in valence band eigenvalues of WSe_2 + Fe system at 100% coverage with varying W-Fe separation z (c) Variation in valence band eigenvalues of MoS_2 + Fe system at 100% coverage with varying Mo-Fe separation z. 88
6.12 Comparison of the valence band eigenvalues of (a) WSe_2 and (b) MoS_2 calculated via DFT (red and blue) and calculated using Eq. 6.42 and 6.43 with the approximations outlined above. μ_z^{Fe} corresponds to $2M_s^{Fe}\cos\theta$ 93

7.1 Illustration of exchange bias. (a) Schematic of FM/AFM interface in which exchange bias would be expected. (b) Schematic of a shifted hysteresis curve, indicating the presence of exchange bias. 95
7.2 The crystal structure of a single layer of $Mn_3(C_6S_6)$. 96
7.3 The inverse magnetic susceptibility of $Mn_3(C_6S_6)$ versus temperature. 97
7.4 The hysteresis curves of $Mn_3(C_6S_6)$ when zero-field cooled (ZFC) and field cooled (FC) at ±1 T. The center of the hysteresis curves shifts depending on the orientation of the applied field during cooling. (b) is a zoomed in version of the curves in (a) to make the shift more clearly visible. 98
7.5 The five magnetic orderings considered for monolayer $Mn_3(C_6S_6)$. 98
7.6 The band structure and element projected density of states for monolayer $Mn_3(C_6S_6)$ in the most stable AFM magnetic ordering. 100
7.7 The band structure and element projected density of states for bulk $Mn_3(C_6S_6)$ in the most stable AFM magnetic ordering. 101

List of Tables

3.1 DFT-GGA+U lattice parameters for $FeWO_4$ for both magnetic configurations studied along with experimental values. The a-lattice parameter for the AFM configuration is taken as half the value of the a-lattice parameter of the 2x1x1 supercell. 28

5.1 Binding energies and relaxed in-plane lattice parameters of WSSe-ZnO heterostructures with different stacking orientations. AA and AB refer to the stacking pattern, whether the two hexagonal lattices are aligned on top of one another or shifted. I and II refer to whether the W is aligned below the Zn or the O atom of ZnO. S and Se refer to which chalcogen is facing the ZnO. 48
5.2 Band gaps of monolayer WSSe, monolayer ZnO, and the two most stable stacking configurations. The band gaps of the heterostructures are very similar to that of monolayer WSSe. 50
5.3 The interlayer distance between the top-most chalcogen and the ZnO layer and the HSE band gaps for 5% compressive strain, no strain, and 5% tensile strain for the WSSe-ZnO and WSeS-ZnO stacking configurations. 50
5.4 The HSE band gaps for the WSSe-ZnO and WSeS-ZnO stacking configurations under application of an out-of-plane electric field. The band gaps do not change considerably. 69

6.1 Experimental and DFT-PBE+U a-lattice parameter for a $\sqrt{3} \times \sqrt{3}$ supercell of WSe_2 and (111)-$BiFeO_3$. 84

7.1 The relative energies of different magnetic configurations for monolayer $Mn_3(C_6S_6)$. 99

Acknowledgments

First and foremost, I want to thank my advisor, Jeff. I am so lucky to have had the privilege to work for a professor who manages to be unbelievably kind, endlessly supportive, and exceptionally scientifically rigorous, all despite having a workload that would take several elephants to tow. Your approach to science, waiting until a paper has something impactful to say that has been examined from every angle rather than just publishing the second you have results, has been so meaningful in shaping how I think about how science should be done. Thank you for teaching me how to explore new ideas. Thank you for being patient with me when I was obtuse. Thank you for believing in me when I had trouble doing that myself.

My research would not have been possible without my scientific collaborators. I owe a huge thank you to John Gregoire at Caltech, with whom I have had the pleasure of collaborating on numerous projects throughout my PhD and who has been nothing but supportive. Also to the Gregoire group members, especially Lan Zhou and Matthias Richter. I am also grateful for having had the opportunity to collaborate with so many other great scientists, including Yi-Rung Lin and Harry Atwater at Caltech and Ryan Murphy and Jeff Long at UC Berkeley.

I have been so lucky to work with such amazing people in the Neaton group. It's incredibly special to work with people who are both intellectual powerhouses from whom I have learned so much science and also warm wonderful friends. Thank you to Sebastian for getting me up and running in the group and teaching me how to do DFT. Jonah, I don't think the words thank you are strong enough for how grateful I am to have been friends and colleagues with you through my PhD. I have grown so much as a scientist working with you and listening to you share your enormously broad body of knowledge. But more importantly, thank you so much for being an incredible friend – for always being willing to listen and letting me draw upon your bottomless well of empathy. Thank you to Stephanie for bringing joy to the group with your delightful goofiness and for being there for me during tough times. I am honored that you dressed up as me for Halloween (and totally nailed the look too!) To Sophie, thank you for being the most reliable lunch buddy and for your spot-on comments that were the perfect balance of deadpan, funny, and real. I am so glad I was able to come to your wedding and share such a special day with you (even if we had to dance with masks on). Marina, I am always wowed by your balance of kindness, groundedness, and out-of-this-world scientific talent. Thank you for always being supportive and optimistic. You and Tony are truly special people. To Samia, thank you for bringing levity and openness to the group and for being one of the most authentic people I know. Thank you to Marisa for being the behind-the-scenes magic that keeps the entire group running. To the rest of the Neatonians, thank you for all the great times – I'm excited to see the amazing things that I know all of you will accomplish.

Outside of the Neaton group, I have been lucky to have a number of incredible women support me before and during my PhD. To Mareike, thank you for being my best nerd girl friend for nearly a decade. I feel so lucky that we both got to go on our journeys from

the figuring-it-out stages of our lives to being (almost) PhDs together. To Tianrui, thank you for your kindness, your realism, and all the deep, thoughtful conversations. To Bridge, my boss and mentor when I worked in tech, thank you for seeing something in me and for encouraging me to pursue graduate school. You were right.

My family played an outsize role in supporting my educational achievements. Thank you to my dad, Brian Peterson, for always being ready to explain math to me that I hadn't learned in school yet in intuitive ways – that played a huge role in shaping my academic confidence. Thank you to my mom, Dorothy Peterson, for teaching me so many things, from how to read to how to do calculus. Importantly, also, for making sure I was well-versed in Pride and Prejudice.

Finally, thank you to my partner Sam. Meeting you is arguably the most important thing I got out of grad school, even more than the PhD at the end. Thank you for supporting me and loving me throughout the journey from first year grad students to graduation. Thank you for encouraging me to not give up on a career in research. I can't wait to start the next chapter in our lives together.

Chapter 1

Introduction

The modern world has been made possible by the discovery, development, and optimization of crystalline and amorphous materials, from the silicon in our computer chips to the graphite in our number 2 pencils. One could argue that humans have encountered condensed matter physics, without realizing it, for thousands of years, dating back to the early metallurgists who discovered how to form bronze from copper and tin. In modern condensed matter physics, the primary problem to be solved is to find solutions to the many-body Hamiltonian describing the interactions between the electrons and ions in a solid state material in order to understand, for example, the structural and electronic properties of these materials, as is discussed in Chapter 2. This Hamiltonian cannot be exactly solved, making the use of approximations necessary.

Two primary approaches are commonly used in the theoretical study of condensed matter physics. The first is the model Hamiltonian approach, in which the many-body Hamiltonian is reduced to the simplest possible Hamiltonian, and then extra degrees of complexity are subsequently added on, in a bottom-up approach. This approach can provide insight into and physical understanding of complex phenomena observed in condensed matter systems, however, without chemical specificity, its ability to predict the physics of specific materials is limited. The second approach is referred to as first-principles, or *ab initio*, condensed matter physics. In this approach, one starts with the full many-body Hamiltonian and makes the fewest possible approximations to simplify the problem until it becomes tractable, a top-down approach. First-principles calculations have the benefit of capturing chemical specificity, or the elemental composition of a particular crystal structure. The primary workhorse of first-principles calculations is density functional theory (DFT), which is described in detail in Chapter 2.

This dissertation focuses on the use of first-principles DFT calculations for the discovery, understanding, and tuning of complex functional energy materials for potential applications in artificial photosynthesis and "Beyond Moore's Law" information technology. Specifically, ternary metal oxide and layered two-dimensional (2D) materials for water splitting and carbon dioxide (CO_2) reduction catalysis and 2D materials for information applications. The electronic structures and ground state properties, such as crystal structures, of these

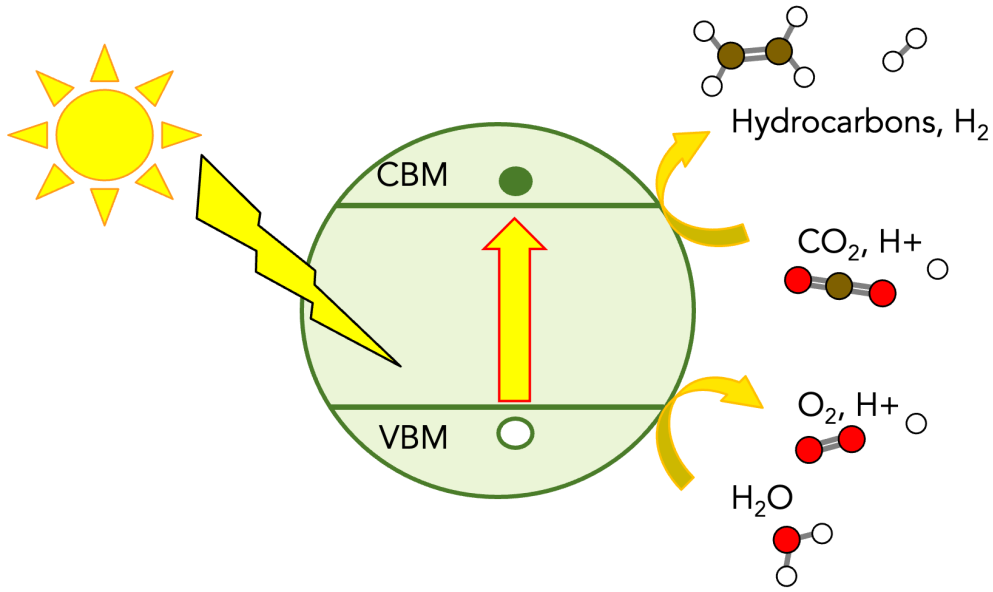


Figure 1.1: Schematic summarizing key processes underlying artificial photosynthesis. Photoexcited holes at a material's surface catalyze oxidation reactions, such as the oxidation of water to O_2 gas, and photoexcited electrons at a material's surface catalyze reduction reactions, such as the reduction of protons to H_2 gas or the reduction of CO_2 to hydrocarbons.

materials are calculated in order to offer insight into their utility and tunability of novel properties required for these applications.

Artificial photosynthesis, or the photocatalytic production of solar fuels such as hydrogen gas and hydrocarbons from water and CO_2, is a promising but nascent green energy technology. By harnessing the underutilized solar energy impinging on the Earth's surface, we seek to produce chemical feedstocks from Earth-abundant water and atmospheric CO_2 in a carbon neutral or carbon negative manner. The general idea behind artificial photosynthesis is that visible light from the sun photoexcites an electron in a semiconducting photocatalyst from the valence band (VB) to the conduction band (CB) and the resulting photoexcited hole and electron go on to catalyze oxidation and reduction reactions respectively (Figure 1.1). In practice, it is difficult to identify single materials that can catalyze both reactions and separate specialized photoanode and photocathode materials are often sought and used. Numerous challenges accompany the search for photocatalyst materials.

In particular, a photocatalyst should have a band gap appropriate for the absorption of visible light (1.2-2.8 eV), appropriate absolute band edge alignment to the relevant redox reactions, good carrier mobility and charge separation (to prevent recombination), and stability under aqueous conditions, among other considerations [1]. To date, known photocatalyst materials generally meet some, but not all, of these criteria, as will be discussed

more specifically below, motivating the continued search for photocatalysts. In this dissertation, we focus primarily on the first two considerations - the relevant characteristics of the electronic structure of candidate photocatalyst materials.

In the context of artificial photosynthesis, photoanodes are materials that catalyze the oxygen evolution reaction (OER) in which water is converted to oxygen gas and protons. Oxide materials have been well-studied for photoanode applications, including Fe_2O_3, WO_3, and $BiVO_4$, because they are earth abundant and often stable in water under operating conditions. These materials suffer from a number of drawbacks. Fe_2O_3 has a band gap of 1.9-2.2 eV which is good for visible light absorption, but it has poor conductivity and rapid charge recombination [2, 3]. WO_3 has a larger band gap of 2.6-2.8 eV, minimizing visible light absorption, suffers from photocorrosion, and has rapid charge recombination as well [2]. $BiVO_4$ has a 2.4 eV band gap and is one of the best performing photoanodes to date, however suffers from low electron mobility [2, 4]. Efforts are underway to better understand and to engineer these materials to perform better, but there is also an impetus towards identifying novel materials for these applications. High-throughput theoretical and experimental efforts have been directed towards this aim. In Chapter 3, we detail the high-throughput experimental discovery of n-type $FeWO_4$ as a high-photovoltage photoanode material by our experimental collaborators. We then detail our studies of the electronic structure of $FeWO_4$ and rationalize the n-type behavior of this traditionally p-type material with a discussion of point defects.

Development of photocathode materials presents certain additional challenges. In particular, product selectivity is dependent on the absolute band edge energies of the photocathode material. There are numerous hydrocarbons that CO_2 can be reduced to. In order to catalyze a particular carbon dioxide reduction reaction (CO_2RR), the CB edge of the catalyst material must be higher in energy than the redox potential required to produce the desired hydrocarbon. The redox potentials for these reactions are clustered close together in a narrow range of energies. Further complicating matters, the hydrogen evolution reaction (HER) which produces hydrogen gas from water competes with the production of hydrocarbons as water is much more abundant under aqueous conditions than CO_2. These factors make fine-tuned control of the absolute band edge energies of photocathode materials exceedingly important.

Layered materials, often referred to as van der Waals (vdW) materials, or 2D materials when exfoliated and isolated, are an emerging class of materials that have received new interest for many applications over the last nearly two decades since the experimental discovery of monolayer graphene in 2004 [5]. These materials consist of monolayers that are one or a few atoms thick with in-plane chemical bonds. Stacks of these monolayers are held together in no small part by vdW dispersion forces in the out-of-plane direction, making it possible to exfoliate them to the monolayer limit [6]. 2D materials can have a variety of electronic structures, from metals like TaS_2, semimetals like graphene, semiconductors like MoS_2, and wide-gap insulators like hBN [7–10]. In this work we focus primarily on semiconducting transition metal dichalcogenides (TMDs) with the MX_2 stoichiometry (M=Mo,W; X = S,Se,Te) and the 2H crystal structure, with a layer of transition metals sandwiched

between two layers of chalcogens in a trigonal bipyramidal coordination (Figure 1.2a,b). Bulk TMDs are indirect gap semiconductors, however, in the monolayer limit they become direct gap semiconductors [9]. In the monolayer limit they exhibit large exciton binding energies due to the reduced dielectric screening above and below a monolayer, with binding energies on the order of 100s of meV [11]. While excitons will not be a primary focus of this work, they are worth noting in any investigation of TMD electronic structure. In particular, in the context of discussing photocatalyst materials, the strong exciton binding energies in monolayer TMDs leads to challenges in producing efficient photoexcited carrier separation, motivating the study of multilayer TMDs and TMD heterostructures.

In Chapter 4 we introduce multilayer alloys of MoS_2 and $MoSe_2$ as electrocatalytic cathode materials for the CO_2RR. The absolute VB and CB edges of $MoSe_2$ are higher in energy than those of MoS_2 by several 100s of meV [12]. By adding controllable quantities of Se into MoS_2 to produce $MoS_{2(1-x)}Se_{2x}$ alloys, our experimental collaborators showed that fine grained control of the band edges of these alloys can be achieved. We perform further first-principles calculations on a variety of candidate crystal structures of $MoS_{2(1-x)}Se_{2x}$ with varying x to understand their experimental measurements. We further explain an unexpected result in the case of lateral heterostructures of MoS_2 and $MoSe_2$.

Another approach to the study of catalytic materials derived from 2D materials that has been widely employed in recent years is the production of vdW heterostructures, or stacks of two or more different types of monolayers. 2D materials lend themselves well to production of vdW heterostructures because, in the absence of out-of-plane chemical bonds, lattice mismatch is not a significant concern [6]. Further, vdW heterostructures often exhibit novel properties not seen in the constituent 2D materials, so that by mixing and matching different combinations of monolayers it could be possible to engineer optimized catalytic materials. In Chapter 5 we discuss vdW heterostructures of the Janus TMD WSSe and monolayer ZnO. Janus TMDs have two different chalcogen ions on either side of the transition metals which results in an out-of-plane dipole moment across the monolayer that has been shown to assist in carrier separation and increase carrier lifetimes by orders of magnitude relative to single-chalcogen TMDs [13–15] (Figure 1.2d). Monolayer ZnO, with a one-atom-thick hexagonal bipartite lattice of Zn and O, also hosts a small dipole moment because of buckling between the Zn and O atoms (Figure 1.2c). The elemental earth abundance and expected enhanced carrier lifetimes of these heterostructures immediately makes them interesting for photocatalytic applications. Further, our calculations reveal that the interplay between the dipole moments gives rise to a high degree of tunability in the absolute band edge energies of these heterostructures in the presence of in-plane biaxial strain and out-of-plane uniaxial strain. This is an emergent phenomenon not seen in either individual monolayer. The results discussed here are expected to be generalizable and open a new pathway towards the development of catalytic materials with tunable band edges.

"Beyond Moore's Law" computing technology, and the field of quantum information science in general, are modern approaches to moving information technology past the traditional use of transistors. The field encompasses both the development of novel methods for storing binary quantities, such as through the spin degree of freedom in spintronics, as well

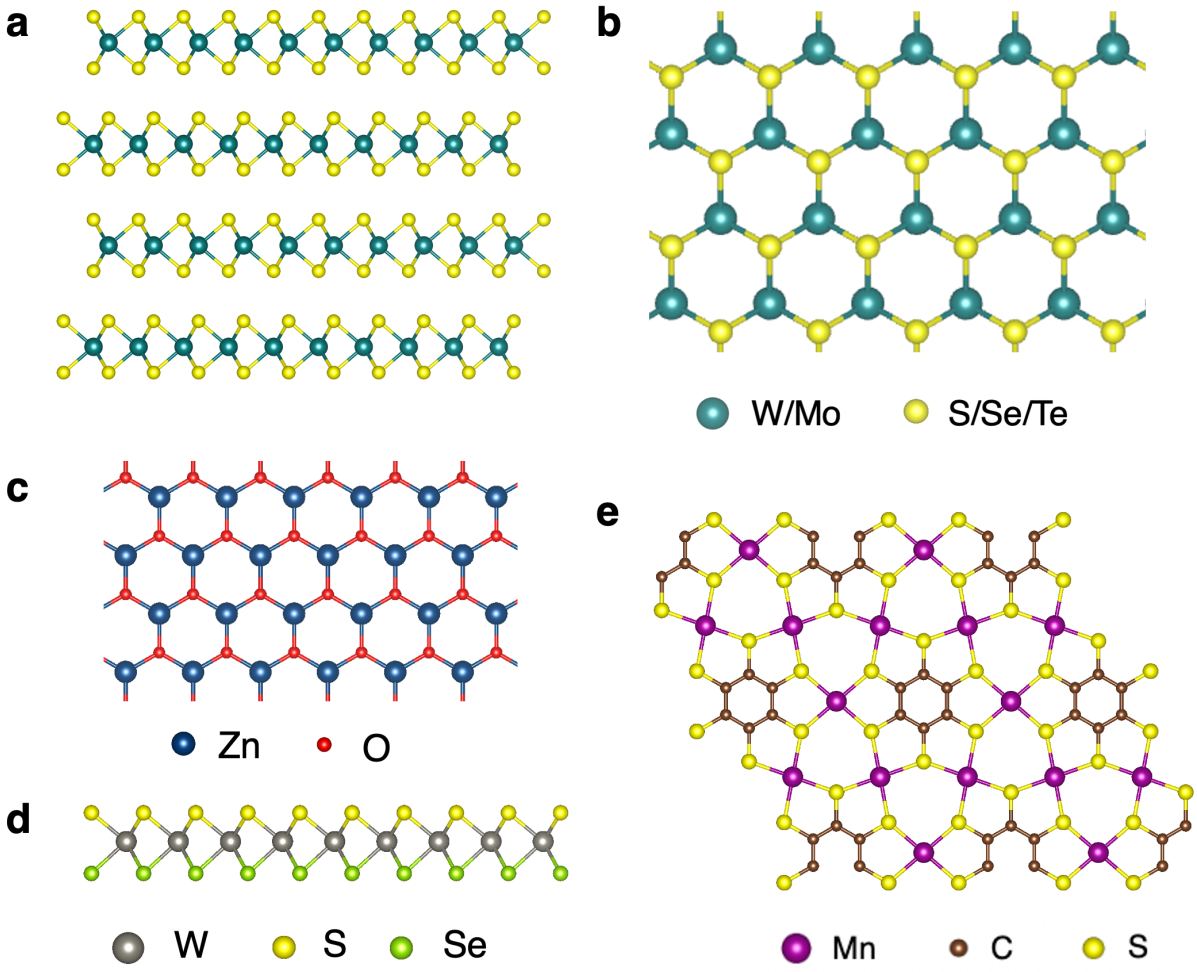


Figure 1.2: Crystal structures of various 2D and layered materials discussed in this dissertation. (a) Side view of a bulk MX_2 TMD, with layers held together by vdW dispersion forces instead of chemical bonds. (b) Top view of a monolayer MX_2 TMD, exhibiting the bipartite hexagonal lattice. (c) Top view of monolayer ZnO, discussed in Chapter 5. (d) Side view of Janus WSSe, discussed in Chapter 5. (e) Top view of $Mn_3(C_6S_6)$, discussed in Chapter 7.

as the development of quantum computing.

Valleytronics, or the harnessing of the valley degree of freedom as a binary quantity, is a field of research in which semiconducting TMDs have received a great amount of attention. Monolayer TMDs exhibit spin-valley locking between the K and K' valleys in the hexagonal Brillouin zone which are energetically degenerate but inequivalent and have opposite spin character, enforced by time-reversal symmetry. Each valley can be selectively excited using left- or right-handed circularly polarized light, respectively [16]. With the application of a magnetic field or proximity to a magnetic substrate, this degeneracy can be broken leading to valley splitting and valley polarization, or breaking of the energetic degeneracy between K and K' to isolate the lowest energy excitation in one of these valleys [17]. In Chapter 6 we discuss the mechanism driving valley splitting by magnetic substrates in monolayer TMDs. In particular, we develop a formalism to understand valley splitting as a result of superexchange, rather than as an effective Zeeman interaction as it is typically described in the literature. We perform a comprehensive study of the effect of proximity and magnetic moment of the magnetic ions in a magnetic substrate to produce general design principles for development of magnetic substrates that can produce maximum valley splitting. We then perform calculations on an idealized magnetic substrate to explore and understand the range of valley splittings that could be achieved by an optimized magnetic substrate.

In Chapter 7 we discuss $Mn_3(C_6S_6)$, a novel 2D metal-organic framework (MOF) that, unexpectedly, exhibits tunable exchange bias. This material is a frustrated antiferromagnet (AFM) with a kagomé lattice of magnetic Mn ions coordinated by organic linker ligands (Figure 1.2e). This 2D MOF is made of earth abundant elements and, as a 2D material, has the advantage of being lightweight and flexible, unlike traditional heterostructures that exhibit exchange bias. At low temperatures it behaves as a spin glass with a highly degenerate ground state and, depending on whether it was field cooled and the directionality of the applied magnetic field during cooling, exhibits exchange bias. Exchange bias has been used historically for magnetic memory applications [18], but has been traditionally unidirectional, making the possibility of selectively controlling the direction of the exchange field an exciting novel phenomenon. Working with experimental collaborators, we have performed calculations that support the existence of a low temperature spin glass state to help rationalize the mechanism driving the observed exchange bias.

In closing, in Chapter 8 we summarize our findings on complex functional energy materials and offer an outlook on this field and future directions.

Chapter 2

Methods

In condensed matter physics, the central problem is finding a solution to the many-body Hamiltonian [19],

$$H = -\frac{1}{2}\sum_i \nabla_i^2 - \frac{1}{2}\sum_A \frac{1}{M_A}\nabla_A^2 + \frac{1}{2}\sum_{i\neq j}\frac{1}{|\mathbf{r}_i - \mathbf{r}_j|} + \frac{1}{2}\sum_{A\neq B}\frac{Z_A Z_B}{|\mathbf{R}_A - \mathbf{R}_B|} - \sum_{i,A}\frac{Z_A}{|\mathbf{r}_i - \mathbf{R}_A|}, \tag{2.1}$$

written here in atomic units, where i,j run over the electronic degrees of freedom, A,B the nuclear degrees of freedom, M_A is the mass of nucleus A, and Z_A is the charge (or atomic number) of nucleus A. The first term represents the kinetic energy of the electrons, the second term the kinetic energy of the nuclei, the third term the electron-electron Coulomb potential, the fourth term the nucleus-nucleus Coulomb potential, and the fifth term the electron-nucleus Coulomb potential. In principle, with knowledge of the energy eigenvalues and the wavefunction $\Psi(\mathbf{r}_1, \mathbf{r}_2, ..., \mathbf{r}_N; \mathbf{R}_1, \mathbf{R}_2, ..., \mathbf{R}_M)$ one may calculate the structural, electronic, and optical properties of any material. In general, a solid consists of N electrons and M nuclei with both N and M on the order of Avogadro's number $\sim 10^{23}$. As such, solving this Hamiltonian with 3N + 3M degrees of freedom is not tractable. Instead, approximation methods are adopted, in addition to using symmetries, such as translational symmetry, to simplify the problem.

2.1 Density Functional Theory

Density functional theory (DFT) is a method widely used to approximately solve the many-body Hamiltonian for condensed matter systems. The first approximation that is made, which is not unique to DFT, is the Born-Oppenheimer approximation [19]. As the nuclei are $> 10^4$ times as massive as the electrons, it is assumed that the nuclei are static and the problem is constrained to the electronic degrees of freedom. More precisely, the electronic states are assumed to evolve adiabatically with respect to any changes in the nuclear coordinates. In this approximation, the kinetic energy of the nuclei is zero and the

nucleus-nucleus Coulomb potential is a constant for a given configuration of nuclei. The nuclei produce a static external potential making the electronic positions the only non-static degrees of freedom in the electron-nucleus Coulomb potential. While this is a vast simplification, the electron-electron Coulomb potential still poses a significant challenge and renders this Hamiltonian not analytically or computationally solvable.

The Hohenberg-Kohn theorems [20] paved the way towards making this problem tractable. The first theorem states that the total energy, E, is a unique functional of the electron density, $\rho(\mathbf{r})$,

$$E[\rho(\mathbf{r})] = \int \rho(\mathbf{r}) v_{ext}(\mathbf{r}) d\mathbf{r} + F[\rho(\mathbf{r})], \tag{2.2}$$

where $v_{ext}(\mathbf{r})$ is the external potential generated by the nuclei and $F[\rho(\mathbf{r})]$ is a universal functional of the electron density that can be broken apart into

$$\hat{F} = \hat{T} + \hat{V_{ee}}, \tag{2.3}$$

where $\hat{T}$ represents the electron kinetic energy and $\hat{V_{ee}}$ is the electron-electron Coulomb interaction.

The second theorem states that the ground state energy can be obtained variationally and that the density that minimizes the total energy is the exact ground state density. The significance of this statement is that the problem of solving for the ground state energy has been reduced from a problem with 3N degrees of freedom to one with 3 degrees of freedom.

However, to solve for the ground state electron density, we need the form of the functional. While Hohenberg and Kohn demonstrated that there exists a unique, universal functional $F[\rho(\mathbf{r})]$, the exact form of this functional is unknown.

Kohn and Sham developed a mean-field approach in which the functional is partitioned into a known non-interacting part and an unknown interacting part [21]. The Kohn-Sham functional can be expressed as

$$F[\rho(\mathbf{r})] = T_e[\rho(\mathbf{r})] + \frac{1}{2} \iint \frac{\rho(\mathbf{r})\rho(\mathbf{r}')}{|\mathbf{r} - \mathbf{r}'|} d\mathbf{r} d\mathbf{r}' + E_{XC}[\rho(\mathbf{r})], \tag{2.4}$$

where $T_e[\rho(\mathbf{r})]$ is the kinetic energy of the N non-interacting electrons, the second term is the electron-electron Hartree interaction, and $E_{XC}[\rho(\mathbf{r})]$ is the exchange-correlation functional, in which all of the unknown interacting effects are stored. The exact form of E_{XC} is not known, however many useful approximations have been developed as will be discussed below.

In the Kohn-Sham framework, we attempt to solve for N fictitious non-interacting single-particle electron wavefunctions $\phi_i(\mathbf{r})$ which constitute the (in principle exact) electron density as $\rho(\mathbf{r}) = \sum_i |\phi_i|^2$. To find the ground state density $\rho_0(\mathbf{r})$ and ground state energy, we enforce the condition that $\frac{\delta E[\rho]}{\delta \rho}|_{\rho_0} = 0$. This leads to a set of Euler-Lagrange equations for the single-particle wavefunctions known as the Kohn-Sham equations, which read

$$\left[-\frac{\nabla^2}{2} + V_{ext}(\mathbf{r}) + \int d\mathbf{r}' \frac{\rho(\mathbf{r}')}{|\mathbf{r}-\mathbf{r}'|} + \frac{\delta E_{XC}[\rho]}{\delta \rho} \right] \phi_i(\mathbf{r}) =$$
$$\left[-\frac{\nabla^2}{2} + V_{ext}(\mathbf{r}) + V_H(\mathbf{r}) + V_{XC}(\mathbf{r}) \right] \phi_i(\mathbf{r}) = \epsilon_i(\mathbf{r})\phi_i(\mathbf{r}). \quad (2.5)$$

A self-consistent variational procedure is used to solve these equations for the ground state electron density. The V_{ext} term is constructed from knowledge of the nuclear positions. Next, an initial guess is made for the electron density and plugged in to calculate the total energy and generate the Hartree term and exchange-correlation term. The Hamiltonian is diagonalized to produce a set of wavefunctions ϕ_i and eigenvalues ϵ_i. These wavefunctions are squared and summed to produce a new electron density. This procedure is repeated iteratively until the total energy converges.

Many ground state properties of a material can be determined by derivatives of this ground state total energy, including forces, force constants, stresses, polarizability, and Born effective charges [19]. Further, ground state crystal structures can be determined by repeating this procedure on a variety of different geometries and identifying the one with the lowest total energy and smallest forces on the nuclei. These "geometry optimization" or "structural relaxation" calculations are often done using a conjugate gradient algorithm, in which new ionic positions are generated iteratively based on the direction of steepest descent of the forces and stresses on the ions.

2.2 Exchange-correlation Functionals

The accuracy of DFT as a method of calculating ground state properties while in the Born-Oppenhaimer approximation is limited by the choice of exchange-correlation functional. While the Hohenberg-Kohn theorems show that a universal exchange-correlation functional exists, its exact form is unknown. As such, approximations must be made.

The most simple approximation is the local density approximation (LDA) [22]. In the LDA, the exchange-correlation energy is the exchange-correlation energy that would correspond to a homogeneous electron gas (HEG) of density $\rho(\mathbf{r})$, namely

$$E_{XC}^{LDA} = \int d\mathbf{r} \rho(\mathbf{r}) \epsilon_{XC}(\rho(\mathbf{r})). \quad (2.6)$$

The generalized gradient approximation (GGA) extends this to include the gradient of the electron density to capture spatial variations in the density, that is

$$E_{XC}^{GGA} = \int d\mathbf{r} \epsilon_{XC}(\rho(\mathbf{r}), \nabla\rho(\mathbf{r})). \quad (2.7)$$

The most commonly used form of GGA is that developed by Perdew, Burke, and Ernzerhof (PBE) [23], which will be used frequently in the following work.

The LDA and GGA work remarkably well in many cases for ground state property calculations despite their relative lack of computational complexity [19]. However there are certain properties and certain types of crystal structures for which they exhibit significant shortcomings.

The band gap of an insulating material, or the energy difference between the highest occupied state and the lowest unoccupied state, is fundamentally an excited state property. As DFT is a ground state theory, and as the eigenvalues that are produced from the Kohn-Sham equations are actually Lagrange multipliers and not true single-particle excitation energies anyway, DFT is not able to accurately calculate band gaps. For GGA, failure to capture the derivative discontinuity in the energy with respect to particle number produces a systematic underestimation of band gaps [24, 25].

2.3 Hubbard U Corrections

The LDA and GGA exchange-correlation functionals are known to perform best in solids where the electrons are delocalized and primarily of s and p character, however, they perform poorly in calculating the charge density for materials with elements that have electrons of d and f character. This is because d and f electrons tend to have more localized wave functions, as can be seen by considering the radial wavefunctions of the hydrogen atom [26]. To remedy this shortcoming, the "Hubbard U" correction scheme can be applied explicitly to the d and f electrons to penalize delocalization. This Hubbard U is not the same as the U value in the Hubbard model [27], but draws inspiration from it as a term that relates to on-site localization. In a simplified and commonly employed DFT+U approach, as implemented by Dudarev [28], a term is added to the total energy as follows:

$$E_{DFT+U} = E_{DFT} + \frac{(U-J)}{2} \sum_{\sigma} \left[\left(\sum_{m_1} n^{\sigma}_{m_1,m_1} \right) - \left(\sum_{m_1,m_2} n^{\sigma}_{m_1,m_2} n^{\sigma}_{m_2,m_1} \right) \right], \tag{2.8}$$

where E_{DFT} is the original DFT total energy, U represents an on-site Coulomb energy, J represents an exchange energy, σ is the spin channel, $n^{\sigma}_{m_i,m_j}$ is an on-site occupancy matrix

$$n^{\sigma}_{m_1,m_2} = \langle \Psi^{\sigma} | m_2 \rangle \langle m_1 | \Psi^{\sigma} \rangle , \tag{2.9}$$

with $|m\rangle$ representing spherical harmonics of a specified angular momentum value. In the Dudarev formulation, U and J aren't meaningful independently; rather they contribute to an effective $U_{eff} = U - J$. In other implementations of Hubbard U corrections they can be treated as separate terms. The DFT+U formalism described by Eq. 2.8 incorporates a subtraction of the energy contributions of the d or f electrons treated in the second term of 2.8, known as the double-counting correction, since the energy contributions of those electrons were already accounted for in the original E_{DFT}. This introduces the possibility of errors as the double-counting corrections will vary depending on the implementation of DFT+U and the selected values of U_{eff}.

The effect of this additional term to the energy is that it increases the total energy when the occupancy matrices are not idempotent (i.e. that their eigenvalues are not 0 or 1 indicating fully unoccupied or fully occupied energy levels). In practice, one selects the specific elements and the angular momenta of the orbitals to which the U_{eff} should be applied, as well as the value of that U_{eff} (which will be simply called U going forward). For example, in Fe_2O_3, one could select a U value of 4.0 eV to be applied to the d orbitals of Fe.

This raises the question of: how does one select an appropriate Hubbard U for a given element in a given material? To date, a foolproof method for selecting the optimal U values has not been fully developed. In practice, there are two commonly employed methods for selecting Us.

The first approach could be termed the "semi-empirical" approach. Calculations are performed with a variety of U values and the U that reproduces an empirical result, such as the band gap,the lattice parameters, or the magnetic moments, is selected. This introduces a degree of empiricism into the calculation that is undesirable in the effort to calculate materials' properties fully from first-principles. The second approach derives from linear response theory [29]. The objective is to reproduce the derivative discontinuity of the excitation energy as a function of particle number that is not accurately captured by the LDA or GGA. Recent efforts to use machine learning to identify appropriate U values are underway and may prove fruitful in the future [30].

Despite the uncertainty in determining the best value of U for a given material, this is still a useful tool for performing calculations on materials with localized orbitals and can be a vast improvement on the uncorrected LDA and GGA methods.

2.4 Hybrid Functionals

Hybrid functionals use a fraction of exact exchange, often with a complementary fraction of semi-local GGA exchange [31]. In the context of solid state systems, it has been observed that hybrid functionals often outperform traditional GGA in calculating band gaps more accurately, a somewhat fortuitous result [32]. This is rationalized by the fact that exact exchange is expected to produce an overestimation of the band gap due to the lack of screening in the bare Coulomb potential which may offset GGA's underestimation of the band gap [24, 25]. Exact exchange takes the following form, in terms of single-particle orbitals:

$$E_X^{exact} = -\frac{1}{2}\sum_{i,j}\iint d\mathbf{r}d\mathbf{r}'\frac{\phi_i^*(\mathbf{r})\phi_j^*(\mathbf{r}')\phi_i(\mathbf{r}')\phi_j(\mathbf{r})}{|\mathbf{r}-\mathbf{r}'|}. \tag{2.10}$$

Range-separated hybrid functionals use different relative fractions of GGA exchange and exact exchange at different length scales, short-range(SR) and long-range(LR). One of the most common versions of this in contemporary solid state physics is HSE06 (commonly just referred to as HSE, although there is another version HSE03) developed by Heyd, Scuseria,

and Ernzerhof [33, 34]. In this formulation, the exact exchange is set to zero at LR, as defined by the range separation parameter γ. This exchange-correlation functional is expressed as

$$E_{XC}^{HSE} = \alpha E_X^{exact,SR}(\gamma) + (1-\alpha)E_X^{PBE,SR}(\gamma) + E_X^{PBE,LR} + E_C^{PBE}, \tag{2.11}$$

where $\alpha = 0.25$ dictates the fraction of exact exchange used and $\gamma = 0.2$ Å^{-1} parametrizes the complementary error function that is used to determine the length scale at which exact exchange makes a significant contribution. Hybrid functionals are generally significantly more computationally expensive than traditional DFT, although recent promising methods have made hybrids more efficient [35].

2.5 van der Waals Dispersion Forces

Another shortcoming of traditional DFT, that is not resolved by the use of hybrid functionals, is the lack of long-range, or non-local, correlation effects. This is most relevant for materials that have significant porosity or significant non-bonding interactions, such as layered materials or porous materials, including metal-organic frameworks [36]. van der Waals (vdW) dispersion forces can be thought of as being caused by the interactions between small, instantaneous dipoles produced by fluctuations in the electron density. In a bulk material these fluctuating dipoles generally have a small effect because of the dielectric screening. In porous materials though, these dipoles can interact across these regions. vdW dispersion interactions play a significant role in determining the ground state crystal structure in these materials. As many properties calculated from DFT are sensitive to the ground state crystal structure lattice parameters and internal coordinates, this can produce significant inaccuracies, such as in calculated values of force constants. The electronic structure can be affected as well since an incorrect crystal structure can erroneously neglect important effects, such as proximity-induced orbital hybridization.

Many methods for incorporating vdW dispersion into DFT calculations have been developed. One of the simplest methods is that derived by Grimme, the DFT-D method [37, 38]. In the Grimme-D method, the total energy and electron density are converged via the normal GGA method, then an energy correction is applied by calculating pairwise corrections between each ion. This method is of the same level of computational expense as GGA itself, since the pairwise corrections are a quick, cheap, post-processing step. The general form of this correction is

$$E_{disp}^{DFT-D} = -\frac{1}{2}\sum_{A\neq B}\sum_{n=6,8,10,\ldots} s_n \frac{C_{AB}}{|\mathbf{R}_A - \mathbf{R}_B|^n} f_{damp}(|\mathbf{R}_A - \mathbf{R}_B|), \tag{2.12}$$

where A,B index ionic sites, C_{AB} is the averaged n^{th} order dispersion coefficient, s_n is a scaling factor and f_{damp} is a damping function. Different implementations of DFT-D use different values for these parameters depending on the GGA functional with which it is to be used, among other considerations. The summation in inverse powers of the internuclear

distances is often truncated after $n = 8$ or $n = 10$. The PBE-D3 method, is one of the most popular of the pairwise vdW dispersion methods.

More advanced vdW functionals (vdW-DF) introduce a more complex form of the correlation functional itself in order to capture non-local correlation effects [36, 39, 40]. Many versions of these functionals exist and they are typically computationally more expensive than standard GGA, although not as much as hybrid functionals. For layered materials, which will be discussed later, the PBE-D3 method actually benchmarks just as well as the best of the vdW-DF functionals with respect to determining crystal structures of layered materials [41].

2.6 Kohn-Sham Electronic Structure

In this dissertation one of the primary focuses is the calculation of band structures and related quantities such as band gaps, band edge energies, and dispersion. These quantities are calculated using Kohn-Sham eigenvalues to reflect the quantities of interest. As stated above, Kohn-Sham eigenvalues are not rigorous observables, merely Lagrange multipliers produced by the variational computation of the ground state charge density. A more accurate treatment of spectroscopic qualities would involve, for example, the use of *ab initio* many-body perturbation theory, such as using the self-energy corrections employed in the GW approximation [19, 42–44] and with electron-hole interactions treated in the Bethe-Salpeter equation (BSE) approach [45].

Neglecting self-energy corrections and working with the Kohn-Sham eigensystem limits the accuracy of the absolute quantities in the calculations performed here. However, much of this work focuses on capturing relevant trends as proof of principle that certain properties can be tuned, rather than accurate calculation of absolute band structure quantities.

For example, while DFT and hybrid functionals do not capture absolute band edge energies accurately, they can capture trends in the band edge energies of related systems, such as nitrides or oxides with variable cation [46, 47]; and we note that in principle DFT can rigorously capture the fundamental band gap center [48]. Further, while DFT does not correctly calculate the band gaps of TMDs, it correctly captures trends in how the magnitude of the band gap varies as a function of strain reported by experiment [49–53].

Future study of these materials and their properties at higher levels of theory would be of interest for a more thorough analysis of optical excitations and linear absorption spectra including excitonic effects.

2.7 Basis Functions

To perform a DFT calculation and diagonalize the Hamiltonians in the Kohn-Sham equations, it is necessary to select a set of basis functions. For crystalline solid state materials, discrete translational symmetry allows calculations to be performed by consideration of only

a single unit cell of a crystal. As a macroscopic solid state system generally has $\sim 10^{23}$ ions, it is reasonable to treat the crystal as though it extends to infinity in all directions with periodic repetition of this unit cell. This should capture the physics of the bulk interior of the crystal.

Because of the periodicity of the lattice, Bloch's theorem [54] allows us to write wavefunctions as

$$\psi_{n\mathbf{k}}(\mathbf{r}) = e^{i\mathbf{k}\cdot\mathbf{r}} u_{n\mathbf{k}}(\mathbf{r}), \tag{2.13}$$

where $\mathbf{k}$ is a crystal momentum, n is a band index as we are generally interested in restricting ourselves to the first Brillouin zone (BZ) (the unit cell in reciprocal space), and $u_{n\mathbf{k}}(\mathbf{r})$ is a cell periodic function that obeys $u_{n\mathbf{k}}(\mathbf{r}) = u_{n\mathbf{k}}(\mathbf{r}+\mathbf{R})$ where $\mathbf{R}$ is a lattice vector of the unit cell.

In the following, we expand the cell periodic part of the wavefunctions in plane wave basis functions, i.e.

$$u_{n\mathbf{k}}(\mathbf{r}) = \sum_{\mathbf{G}} c_{n\mathbf{k}}(\mathbf{G}) e^{i\mathbf{G}\cdot\mathbf{R}}, \tag{2.14}$$

where $\mathbf{G}$ are reciprocal lattice vectors.

As it is not computationally possible to sum over an infinite set of plane waves, a cutoff, E_{cut} is selected that sets an upper bound on the kinetic energy of the included plane waves. Convergence tests are performed on the relevant material properties to determine if sufficiently many plane waves have been included in the basis set, that is

$$\frac{\hbar^2|\mathbf{k}+\mathbf{G}|^2}{2m_e} \leq E_{cut}. \tag{2.15}$$

2.8 Pseudopotentials

Even in the case of a unit cell of a crystal which may have only a few ions, each ion has many electrons associated with it, corresponding to the atomic number Z. In the case of materials with elements beyond the first period or two of the periodic table, treating all of these electrons explicitly becomes computationally expensive, with calculations scaling roughly as N^3. Generally, the electronic properties of a material are dominated by effects associated with the outermost, or valence, electrons [19].

A simplifying assumption can be made that the innermost, or core, electrons do not make significant contributions to the chemistry of a solid state system beyond screening the nuclear charges, as they are tightly bound to the nuclei. In practice, this amounts to treating only the valence electrons explicitly and lumping the core electrons into the nuclei. In constructing a functional form of the external potential, v_{ext}, produced by the ions and experienced by the valence electrons, the core electrons must be incorporated into this v_{ext}.

Pseudopotentials are effective potentials that replace the true Coulomb potential experienced by the valence electrons arising from the nuclei and core electrons with a simpler functional form [19]. The core electrons are thus frozen and eliminated from explicit consideration.

In an all-electron treatment of the electron wavefunctions, the valence electron wavefunctions must be orthogonal to those of the core electrons. As a result, the wavefunctions of the valence electrons in the vicinity of the core adopt a complicated form, exhibiting rapid oscillations. As the assumption is that the relevant physics of the valence electrons occurs further away from the nuclear cores, a well-motivated simplification is to use a pseudo-wavefunction that is smoothed to minimize the number of nodes in the core region but accurately capture the behavior of the true wavefunction outside of a reasonable cut-off radius, r_c. With fewer nodes, fewer reciprocal lattice vectors are necessary to produce the pseudo-wavefunctions than the all-electron wavefunctions, simplifying the calculation immensely.

Pseudopotentials thus make it possible to simplify DFT calculations by (a) neglecting explicit treatment of core electrons and (b) using pseudo-wavefunctions to treat valence electrons that converge more rapidly as a function of E_{cut}.

One commonly used type of pseudopotential is the norm-conserving pseudopotential [55]. These pseudopotentials are constructed such that

$$\int_{r<r_c} d\mathbf{r}\psi^*_{AE}(\mathbf{r})\psi_{AE}(\mathbf{r}) = \int_{r<r_c} d\mathbf{r}\tilde{\psi}^*_{ps}(\mathbf{r})\tilde{\psi}_{ps}(\mathbf{r}), \tag{2.16}$$

where ψ_{AE} is the true all-electron wavefunction and $\tilde{\psi}_{ps}$ is the pseudo-wavefunction. For $r > r_c$, ψ_{AE} and $\tilde{\psi}_{ps}$ should be identical.

Another approach to the construction of pseudopotentials is the projector-augmented wave (PAW) method [56]. In this dissertation this is the primary approach that will be used. In this formalism, the all-electron wavefunctions can be constructed from the pseudo-wavefunctions by a linear transformation $\mathcal{T}$ such that

$$|\psi\rangle = \mathcal{T}\,|\tilde{\psi}\rangle\,, \tag{2.17}$$

where ψ is the all-electron wavefunction, $\tilde{\psi}$ is the pseudo-wavefunction, and we have dropped the $n\mathbf{k}$ subscripts for simplicity. Since $\psi = \tilde{\psi}$ must hold outside the cutoff radius, $\mathcal{T}$ is defined such that

$$\mathcal{T} = 1 + \sum_R \hat{\mathcal{T}}_R, \tag{2.18}$$

where $\hat{\mathcal{T}}_R$ only acts within the cutoff radius, in the so-called augmentation region. The pseudo-wavefunction is expanded into a series of pseudo partial waves $\tilde{\phi}_i$, with i encompassing all the relevant degrees of freedom, such that

$$|\tilde{\psi}\rangle = \sum_i c_i\,|\tilde{\phi}_i\rangle\,. \tag{2.19}$$

The pseudo partial waves must obey

$$|\phi_i\rangle = \mathcal{T}\,|\tilde{\phi}_i\rangle\,. \tag{2.20}$$

and $\phi_i = \tilde{\phi}_i$ outside the cutoff radius. Next, projector functions $|\tilde{p}_i\rangle$ can be defined as:

$$c_i = \langle \tilde{p}_i|\tilde{\psi}\rangle\,, \tag{2.21}$$

where

$$\langle \tilde{p}_i|\tilde{\phi}_j\rangle = \delta_{ij}. \tag{2.22}$$

This allows us to write the linear transformation operator $\mathcal{T}$ as

$$\mathcal{T} = 1 + \sum_i \left(|\phi_i\rangle - |\tilde{\phi}_i\rangle \right) \langle \tilde{p}_i|\,, \tag{2.23}$$

and hence

$$|\psi_{n\mathbf{k}}\rangle = |\tilde{\psi}_{n\mathbf{k}}\rangle + \sum_i \left(|\phi_i\rangle - |\tilde{\phi}_i\rangle \right) \langle \tilde{p}_i|\tilde{\psi}_{n\mathbf{k}}\rangle\,. \tag{2.24}$$

The PAW approach has been shown to reduce the computational expense of plane-wave basis DFT calculations [56] and will be used extensively in the following work.

2.9 Relativistic Effects

Spin-orbit coupling (SOC) is a relativistic fine-structure effect that acts as a perturbation to the energy eigenvalues of a system [26]. In the simplest case, the hydrogen atom, this produces an energy correction of the form

$$\Delta H = -\frac{\mu_B}{\hbar m_e e c^2}\frac{1}{r}\frac{\partial U(r)}{\partial r}\mathbf{L}\cdot\mathbf{S}, \tag{2.25}$$

where μ_B is the Bohr magneton, U is the potential energy of the electron in the central force field produced by the proton, $\mathbf{L}$ is the orbital angular momentum and $\mathbf{S}$ is the spin angular momentum.

A similar form of this equation applies to solid state systems as well. The energy correction associated with SOC scales as Z^4 where Z is the atomic number of the element. In materials that have heavy elements, SOC can become important. In DFT, the energetic perturbation associated with SOC can be added to the total energy of the system as a perturbation or it can be treated self-consistently [57]. The incorporation of spinors as three-component vectors into these calculations is critical as the spin angular momentum is of fundamental importance because SOC serves to couple the spin degrees of freedom to the

crystal lattice. This increases the computational cost of calculations including SOC, however significantly improves upon the accuracy of electronic structure calculations for elements with heavy elements.

2.10 Supercells for Low-Dimensional Materials

Low-dimensional materials have periodic boundary conditions in fewer than three directions. For example, monolayer TMDs, as will be discussed at length in this dissertation, have periodic boundary conditions in the a- and b-directions, but not in the c-direction (Figure 2.1). As DFT codes that use plane-wave bases must employ periodic boundary conditions in all three directions, a supercell approach is commonly used. In this approach, a large region of vacuum is inserted above the monolayer, generally ∼20 Å. This helps reduce spurious interactions between periodic images of the monolayer in the c-direction. In the case of a one-dimensional material (e.g. a carbon nanotube) or a zero-dimensional material (e.g. a quantum dot or a molecule), one would include vacuum insertions in two or all three directions, respectively.

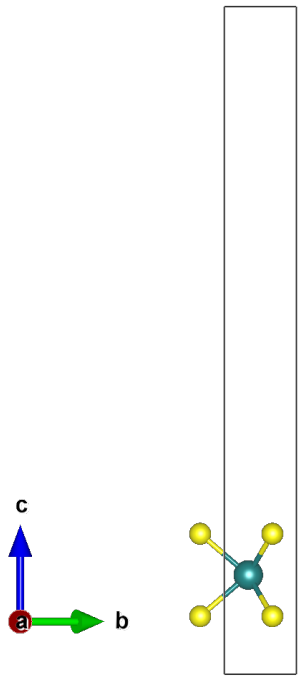


Figure 2.1: A supercell of a monolayer TMD with a large vacuum region above the monolayer to reduce spurious interactions between periodically repeated monolayers in the c-direction.

A subtle point that is not often discussed is the importance of including vdW dispersion corrections during structural relaxations of monolayer 2D materials. Including vdW dispersion corrections for structural relaxations of bulk layered materials is standard operating procedure, although care must be taken in selecting an appropriate vdW correction scheme as different methods are less effective for layered materials and may perform better for, say, molecules or rare-gas solids (e.g. Ar, Xe) [58, 59]. In layered materials, appropriately chosen vdW correction schemes (e.g. PBE+D3 [37, 38], rev-vdW-DF2 [60]) assist in correctly capturing the length of the c-lattice parameter, which is generally overestimated by the commonly used PBE functional in the absence of dispersion corrections [41, 59]. However, this is often neglected for monolayers, which at times, perhaps counterintuitively, results in inaccuracies in geometric optimization of the monolayer crystal structure. While some monolayer materials, such as those that are one-atom-thick (e.g. graphene), do not benefit significantly from the inclusion of vdW dispersion corrections with respect to accurate calculation of the a-lattice parameter, others do [59], which can have consequences for the calculated electronic structure (as demonstrated below). For TMDs in particular, which have three-atom-thick monolayers, the a-lattice parameter can be sensitive to dispersion corrections [59]. In the work performed for this dissertation, it has been observed that vdW dispersion forces significantly out-perform semi-local XC functionals for TMDs in predicting a-lattice parameter values closer to the experimental lattice parameters (as in the example below), with consequences for the electronic structure.

As discussed in Chapter 1, monolayer MoS_2 is a direct gap semiconductor. For illustration, the band structure of monolayer MoS_2 without and with dispersion corrections is calculated and displayed in Figure 2.2. These calculations are performed using density functional theory (DFT) with a plane-wave basis and projector augmented wave (PAW) pseudopotentials [61] as implemented in the Vienna *ab initio* Simulation Package (VASP) [62, 63]. Geometry optimization calculations are performed using the generalized-gradient approximation (GGA) as implemented by Perdew, Burke, and Ernzerhof (PBE) [23] both without and with the addition of van der Waals dispersion corrections using the Grimme-D3 method [37, 38]. An energy cutoff of 600 eV is used with a 12x12x1 Γ-centered k-grid. Structures are relaxed until forces are less than 1 meV/Å. Spin-orbit coupling is not included.

As seen in Figure 2.2, the band structure calculated with the crystal structure obtained from geometric relaxation using PBE is an indirect gap semiconductor, while that calculated with the crystal structure obtained with PBE+D3 is a direct gap semiconductor. The relaxed a-lattice parameter obtained with PBE is 3.18 Å and that obtained with PBE+D3 is 3.16 Å. The experimental a-lattice parameter is 3.15 Å [64]. While the PBE a-lattice parameter appears to be very similar to the experimental value, corresponding to only ∼1% tensile biaxial strain, this is enough to change the relative ordering of the Γ point and the K point in the valence band.

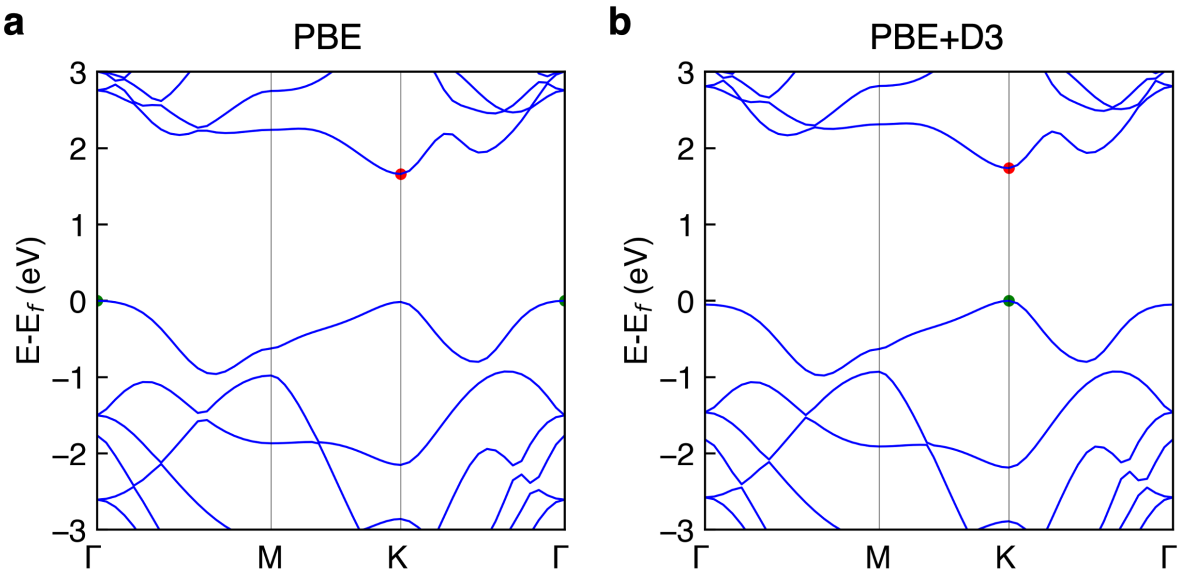


Figure 2.2: The band structure of MoS_2 calculated (a) without and (b) with vdW dispersion corrections. The valence band maximum is marked with a green circle and the conduction band minimum is marked with a red circle. The band structure calculated without dispersion corrections erroneously exhibits an indirect band gap.

2.11 Electrostatic Potential and Absolute Band Edge Calculations

Often, the work function of a material is a quantity of interest. The work function corresponds to the amount of energy required to take an electron in the highest energy occupied state to a point infinitely far away, or at least sufficiently far away that it no longer experiences a significant attractive force from the positively charged nuclei and the rest of the electrons. For photocatalytic applications, it is important to quantify the positions of the band edge energies relative to an absolute reference so as to determine their positions relative to the redox energies of the chemical reactions of interest, as discussed in Chapter 1 and to be discussed further in Chapters 4 and 5. The energy eigenvalues that are obtained from a standard DFT calculation are not physical in and of themselves - they are an artifact of the particular forms of the exchange-correlation functional and the pseudopotentials used and only defined up to an arbitrary constant, given the periodic boundary conditions. As such, an absolute reference that is calculated on the same energy scale as the eigenvalues is necessary in order to compare the energy of the highest occupied state to an absolute reference.

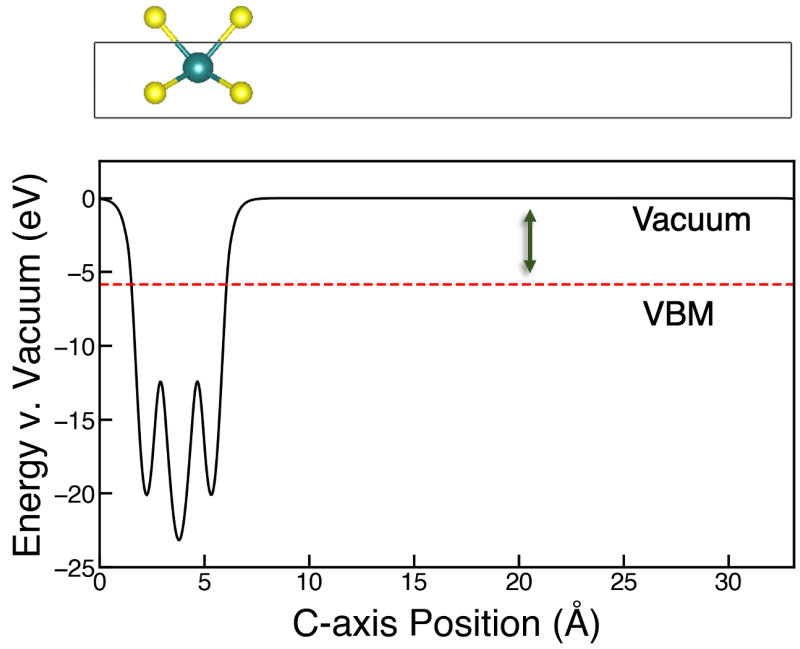


Figure 2.3: The plane-averaged electrostatic potential of a monolayer TMD along the c-axis direction, with the relevant crystal structure for reference. The energy scale has been shifted so that the electrostatic potential is 0 in the vacuum region. The difference between the vacuum region electrostatic potential and the valence band maximum (VBM) is taken to be the absolute position of the VBM.

In practice, this is accomplished by constructing a supercell including a slab of the material of interest and including a vacuum insertion above it [46, 65, 66]. For monolayer and layered materials this is straight-forward as no bonds need to be broken to generate a slab. For three-dimensional (3D) bulk materials, with chemical bonds in all three dimensions, care must be taken to identify the lowest energy surface facet. Then, the plane-averaged self-consistent electrostatic potential is calculated throughout the unit cell, using planes that are parallel to the surface of the slab to obtain values for the electrostatic potential both inside the slab and in the vacuum region. In practice, often only the Hartree potential (V_H) is included, rather than the Hartree potential plus the XC potential (V_{XC}), as the V_H converges more rapidly to the vacuum level in the vacuum region and V_H should be equal to $V_H + V_{XC}$ in the vacuum region where there are no electrons and the charge density is zero [65]. The energy of the valence band maximum (VBM) eigenvalue can be compared to the electrostatic potential in the vacuum region to quantify an absolute VBM position relative to vacuum (Figure 2.3). The length of the vacuum region and the thickness of the slab (if it is a 3D material) should be varied in order to ensure that this quantity is converged. In the case

where the surface is polar, with a non-zero net dipole moment normal to the surface, dipole corrections are employed [67]. This amounts to a fictitious layer of opposing polarization placed somewhere in the vacuum region to counteract the different electrostatic potentials on either side of the slab caused by the finite dipole moment.

In practice, the absolute position of the conduction band minimum (CBM) is obtained by adding the band gap of the material to the absolute VBM energy, using the band gap of the bulk crystal, not the slab, for 3D materials. As band gaps calculated with DFT are inaccurate, these absolute CBM values are expected to be inaccurate. For that matter, the VBM position is not necessarily accurate either, as it varies depending on the XC functional used. For example, HSE tends to predict VBM positions that are significantly lower in energy than those predicted by PBE, often by 100s of meV [46]. For many materials, PBE generally underestimates the experimental work function, or predicts a VBM position that is higher in energy than the experimental value [68], but with an error that is not as large as the discrepancy between PBE and HSE. Given this, the band edge positions obtained from DFT, whether via semi-local functionals like PBE or hybrid functionals like HSE, should be assumed to capture trends, and not absolute values. The effectiveness of these methods for calculating trends is discussed in Ref. [46]. In Chapters 4 and 5 of this dissertation, band edge calculations are performed in an effort to calculate trends in band edge energies as a function of varying chemical composition and varying applied strain.

2.12 Phonon Calculations

Phonons are collective excitations that emerge in crystals that are characterized by vibrations of the ionic lattice. In the harmonic approximation, the interatomic potential energy is truncated at second order, just as in the case of a simple harmonic oscillator. With knowledge of the interatomic force constants, the frequency eigenvalues and eigenvectors of the ionic vibrations, or the phonon modes, can be calculated. Phonon modes, often represented in the form of a phonon band structure analogous to electronic band structures, are parameterized by a crystal momentum q and a branch index λ (equivalent to the band index used in electronic structure) [69]. Two primary methods are used to calculate phonon band structures with DFT.

In the frozen phonon method, one ion is displaced and the forces produced on all the other ions as a result of this displacement are calculated [19]. This approach requires the use of large supercells, as in principle one is attempting to capture the effect of a single ion's displacement on all other ions in the entirety of the infinite crystal. The ions in the immediate vicinity of the displaced ion experience the largest forces, with the induced forces diminishing in magnitude as a function of distance from the displaced ion. In practice, one must converge the size of the supercell so that it is large enough that periodic images of displaced ions do not significantly affect each other.

Alternatively, density functional perturbation theory (DFPT) can be employed [70]. This method involves directly calculating the second order derivatives of the energy and

does not require large supercells.

A unit cell with N atoms will have 3N phonon branches [69]. The 3 lowest energy branches are the acoustic modes, so called because they exhibit linear dispersion near the Brillouin zone center, analogous to the linear dispersion of sound waves. The other 3N-3 branches are referred to as optical modes. In a physical crystal, all phonon modes should have positive frequency. At times, phonon band structures will exhibit optical modes with imaginary phonon frequencies. This indicates that the crystal structure for which the phonon band structure was calculated is dynamically unstable, and the corresponding physical crystal would be expected to undergo a phase transition to a different crystal structure.

2.13 Codes

In this dissertation, first-principles DFT calculations are performed using the Vienna *ab initio* simulations package (VASP) [62, 63] using plane-wave bases and PAW pseudopotentials [56, 61]. Specifically, versions 5.3.5 and 5.4.4 of VASP are employed.

Phonon calculations are performed using the frozen phonon method with DFT calculations of the forces performed using VASP and generation of representative crystal structures with displaced ions produced by the phonopy package [71].

Chapter 3

High photovoltage and oxygen vacancies in n-type $FeWO_4$

This chapter is adapted from [1]. This work was done in collaboration with experimentalists in the Gregoire group at Caltech. In this dissertation, we summarize the experimentalists' findings then outline our theory contributions. We performed first-principles DFT band structure and density of states calculation on various magnetic orderings of the novel photoanode material $FeWO_4$. The calculated band structures indicate that this material has large carrier effective masses and expected low mobility, contrary to the experimental findings of high photovoltage. To rationalize the source of the carrier mobility in the experimentally synthesized samples, we perform a calculation of the phase diagram of Fe-W-O materials under synthesis conditions and use these results to conclude that oxygen must not have diffused completely through the sample during synthesis resulting in oxygen vacancies that drive the formation of electron polarons. We hypothesize these to be the primary carriers in this material.

3.1 Introduction to Oxide Photoanodes

Efforts to identify photoanode materials for solar fuels generation have been hampered by challenges in identifying materials with (i) band gaps that utilize a large fraction of the visible spectrum, (ii) excellent carrier separation (or low recombination rates) (iii) operational stability under aqueous conditions, and (iv) high carrier mobilities, among other considerations [72]. High recombination rates and low carrier mobilities, in particular, limit achievable photocurrents and photovoltages.

Metal oxides are promising candidates for photoanode applications for the oxygen evolution reaction (OER) because they are often able to withstand oxidizing conditions without decomposing. While some success has been made in the development of metal oxide photoanodes, there remains a great deal of space for optimizing metal oxides for this application.For example, alloying and morphology optimization of $BiVO_4$ has improved its initial reported

above-gap external quantum efficiency (EQE) from about 10% [73] to above 90%, [74] and recent optimization of multilayer coatings has improved the stability and lowered the turn-on voltage (lowest potential where photocurrent is observed, which can be no lower than the flat band potential) from 0.4 V vs RHE to 0.2 V vs RHE [75]. However, improving solar spectrum utilization with materials engineering has been relatively unsuccessful, highlighting the importance of discovering photoanode materials with lower band gaps that can be further developed into efficient photoanodes.

Fe_2O_3 and WO_3 are classic photoanode materials, making iron tungstates a promising search space for new photoanodes [2, 3]. Ternary metal tungstates such as $CuWO_4$ and $SnWO_4$ have also been previously reported as emerging photoanode materials [76–78]. $FeWO_4$ is a ternary metal oxide that has traditionally been reported as p-type and has not been reported to be particularly photoactive [79]. In collaboration with the experimental group of John Gregoire at Caltech, we have identified a novel n-type form of $FeWO_4$ that exhibits a 1.95 eV band gap and a $\gtrsim$ 0.8 eV photovoltage, which is the highest photovoltage that has been reported to date in a sub-2 eV band gap material [1].

3.2 Photovoltage

Photovoltage is an experimental metric that describes how effectively photoexcited minority carriers are reaching the surface of a material [80]. In the bulk of a material, the absolute band edges are static and are referred to as the "flat band potentials". Near the surface, however, band bending occurs (Figure 3.1). This is a result of the complexity of surfaces, including, but not limited to, reconstruction, dangling bonds, and trap states. The concentration of the majority carriers is typically different from that in the bulk and can exhibit an accumulation layer, depletion layer, or inversion layer. Typically, the band edges of n-type materials shift up in energy and the band edges of p-type materials shift down in energy at a surface, relative to the bulk flat band potentials.

When the material is illuminated, photoexcited electrons and holes are produced in the bulk. In an n-type material with excess electrons at the surface and bands bent to higher energies, the arrival of photoexcited holes at the surface changes the surface potential and decreases the degree of band bending (Figure 3.1). The degree to which the bands are unbent is referred to as the photovoltage. As oxidation reactions are catalyzed by holes, it is critical that an n-type photoanode material exhibit high photovoltage.

One method of measuring photovoltage is to compare the turn-on potentials of a photoanode under illumination and in the dark. The turn-on potential is the applied potential at which a photocurrent is measured. In the presence of sodium sulfite as a sacrificial hole acceptor, a photoanode material is expected to have a turn-on potential at 1.23 V. Hence in the dark, the turn-on potential should be 1.23 V. Under illumination, if hole minority carriers are able to migrate to the surface, the turn-on potential should be smaller. The difference between the turn-on potential under illumination and 1.23 V in this experimental set-up reflects the photovoltage generated by illumination.

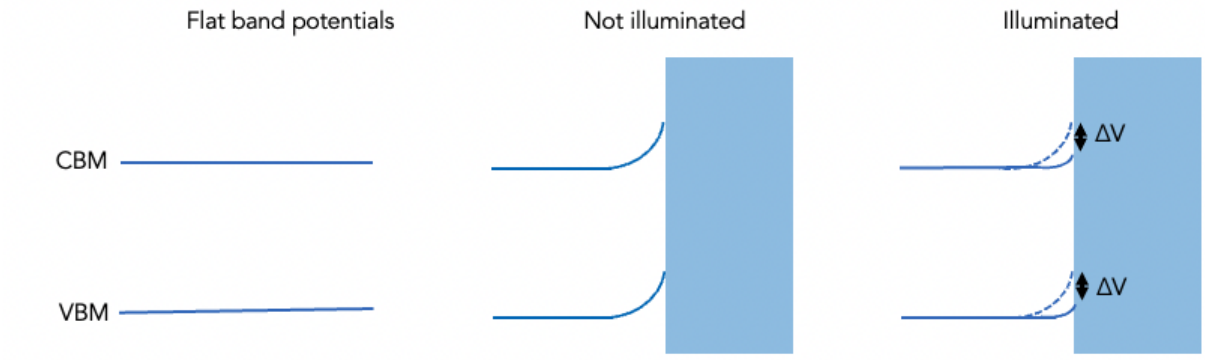


Figure 3.1: Schematic of flat band potentials (left), band bending at the surface of an n-type material (middle), and photoexcited carrier induced band unbending, with the degree of band unbending indicated as the photovoltage ΔV (right).

3.3 Experimental Results

The experimentalists in the Gregoire group at Caltech performed high-throughput experimental analysis of Bi, Fe, and W oxides at a variety of stoichiometries. Exploration of Bi–W–Fe oxides proceeded through synthesis of combinatorial metal oxide libraries using two complementary methods to gauge the effects of materials processing. Both libraries were prepared by sputter deposition of metal targets onto a 100 mm diameter SnO2:F (FTO)-coated glass substrate and subsequently annealed in air at 610 °C for 1 hour. One library was deposited as with oxide precursors using 10% O_2 in the sputter atmosphere, resulting in relatively weak optical absorption, whereas the film deposited with metal precursors using only Ar as a sputter gas exhibited high optical absorption over a broad composition range and became the focus of photoelectrochemical (PEC) characterization. Using a previously reported scanning droplet cell for high-throughput screening [81], characterization of the spectral photoresponse at 1.23 V vs RHE was performed on 215 compositions in aqueous pH 9 borate electrolyte with 0.01 M sodium sulfite as the sacrificial hole acceptor (SLF9) using toggled illumination chronoamperometry (CA). While the photocurrent was measured using four light-emitting diodes (LEDs) spanning 2.07–3.2 eV, the photocurrent at 2.4 eV is particularly important because appreciable photoresponse at this photon energy demonstrates utilization of lower-energy photons than state-of-the-art photoanode $BiVO_4$. Such photocurrent was observed near the Fe–W binary line with Fe concentration between 0.5 and 0.7 and Bi concentration below 0.2, prompting the choice of $Fe_{0.56}W_{0.38}Bi_{0.06}O_z$ for further characterization (Figure 3.2).

X-ray diffraction (XRD) measurements indicated that the dominant phase in the sample

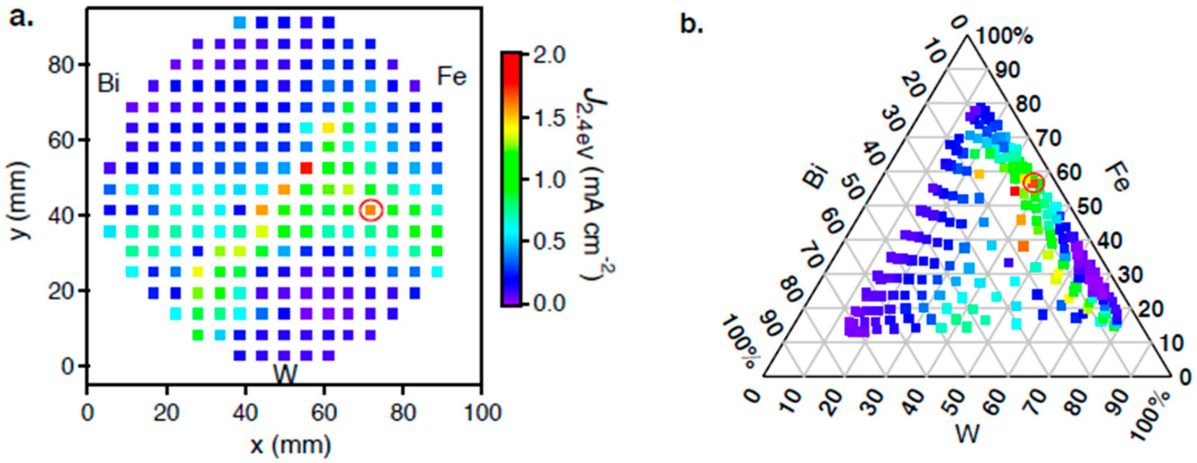


Figure 3.2: Photocurrent measurements of Fe-W-Bi combinatorial library by (a) position space and (b) composition space. Reproduced from [1].

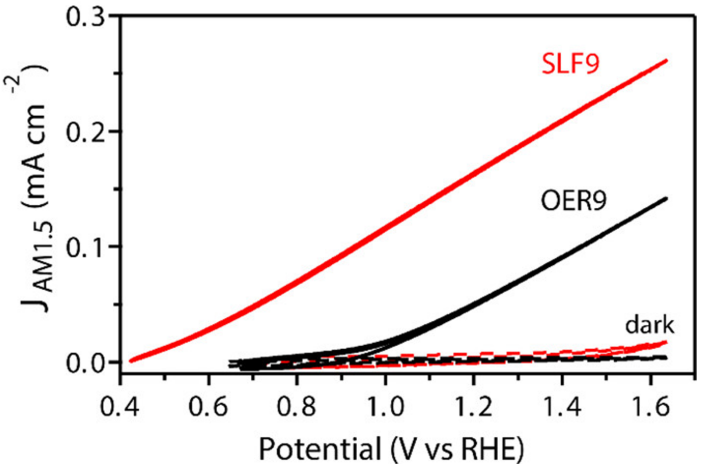


Figure 3.3: Turn-on potential of $Fe_{0.56}W_{0.38}Bi_{0.06}O_z$ sample in the light (solid lines) and in the dark (dashed lines) and with (SLF9) and without (OER9) a sacrificial hole acceptor at pH=9. Reproduced from [1].

is $FeWO_4$ with a minority phase of Bi_2O_3. Tauc analysis revealed that the direct band gap of this sample was $\sim$ 1.95 eV. Cyclic voltammetry (CV) measurements were performed in the pH=9 electrolyte with and without AM 1.5G illumination (light versus dark conditions), both with and without the sacrificial hole acceptor. In the presence of the sacrificial hole acceptor and under illumination, the turn-on potential was measured to be $\sim$ 0.4 V vs. RHE. Hence the measured photovoltage produced under illumination is $\gtrsim$ 0.8 eV (Figure 3.3).

X-ray photoelectron spectroscopy (XPS) measurements revealed that the top layer of the sample was Fe-rich and predominantly Fe^{3+} indicating the presence of a passivation layer of Fe_2O_3 on the surface of the film.

Further analysis of the role of this passivation layer was conducted via synthesis of an additional sample in an exclusively Fe-W library. A majority phase of $FeWO_4$ was detected via XRD measurements at the $Fe_{0.62}W_{0.38}O_z$ stoichiometry and only in a thicker portion of the plate. PEC measurements on this new sample revealed that the photocurrent is lower than in the Bi-containing sample, however a photoresponse exists both for phase mixtures with Fe_2O_3 and WO_3, indicating that $FeWO_4$ is indeed the photoactive phase. Further Mott-Schottky analysis on the $Fe_{0.62}W_{0.38}O_z$ sample indicated that it exhibits n-type conductivity.

3.4 Electronic Structure Calculations

To better understand the experimental results, in particular the origin of the n-type conductivity in a traditionally p-type material, we perform further analysis of the geometry, magnetism, and electronic structure of $FeWO_4$.

First-principles calculations are performed using density functional theory (DFT) with a plane-wave basis and projector augmented wave (PAW) potentials [61] as implemented by the Vienna *ab initio* simulation package (VASP) [62, 63]. All calculations are spin-polarized and performed in the generalized gradient approximation as implemented by Perdew, Burke and Ernzerhof (PBE) [23], with the addition of a Hubbard U term (PBE+U) [28] to account for on-site localization on the Fe and W ions. U values of 5.3 and 6.2 are used for Fe and W respectively, which are chosen to match the values used by the Materials Project database [82]. A plane-wave energy cut-off of 500 eV is used with a 5×4×4 Γ-centered k-point mesh. Structural relaxations are performed in all cases until forces are less than 1 meV/Å. Tables 3.1 lists the optimized lattice parameters for comparision with experimental values. Band structures are generated for both ferromagnetic (FM) and antiferromagnetic (AFM) spin configurations of the Fe atoms (Figure 3.4). Multiple AFM orderings are considered and the most stable one is selected for further analysis.

The band structures of FM and AFM ordered $FeWO_4$ are displayed in Figure 3.5. Notably, in both cases the valence band (VB) and conduction band (CB) are relatively flat, with minimal dispersion. This implies that the electron and hole effective masses are large, meaning that the mobility of the carriers that are producing the high photovoltage is not driven by band-like dispersion.

	a (Å)	b (Å)	c (Å)
DFT, FM	4.787	5.820	5.080
DFT, AFM	4.804	5.790	5.094
ICSD ID 26843	4.730	5.703	4.952

Table 3.1: DFT-GGA+U lattice parameters for $FeWO_4$ for both magnetic configurations studied along with experimental values. The a-lattice parameter for the AFM configuration is taken as half the value of the a-lattice parameter of the 2x1x1 supercell.

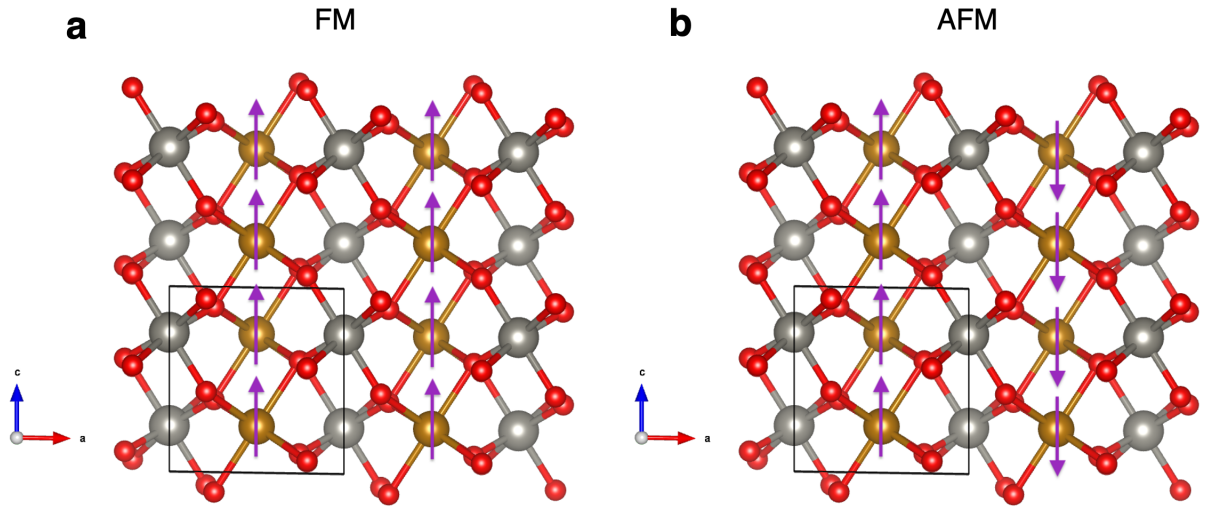


Figure 3.4: The crystal structure of $FeWO_4$ and the two magnetic configurations considered in first-principles calculations (a) FM and (b) AFM. Fe ions are gold, W ions are silver, and O ions are red.

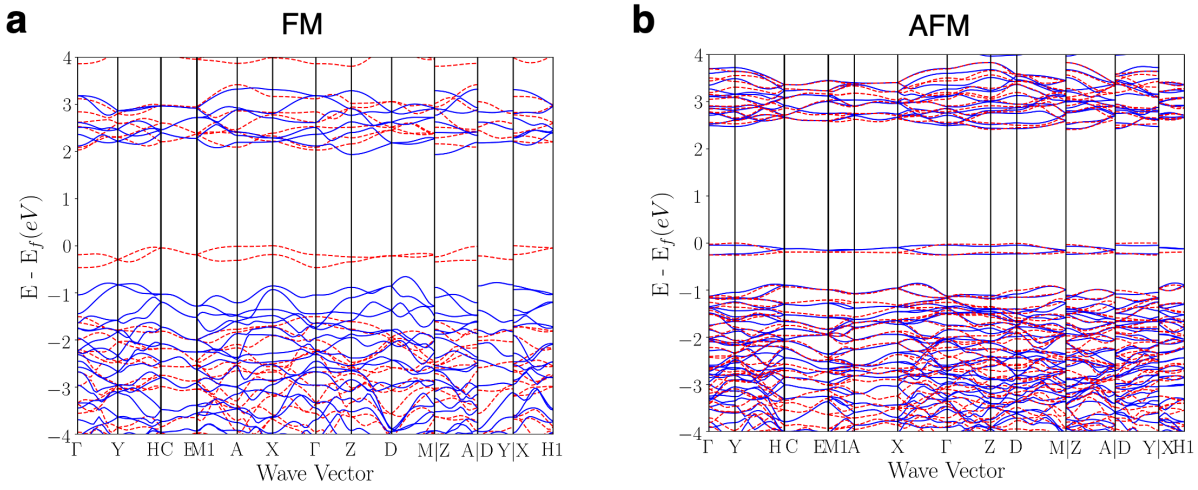


Figure 3.5: The band structures of $FeWO_4$ in the (a) FM and (b) AFM magnetic configurations. In both cases, the bands are relatively flat with minimal dispersion.

The element-projected density of states (Figure 3.6) offers further insight into the electronic structure of $FeWO_4$. The VB is domainted by contributions from highly-localized Fe states and the CB is dominated by contributions from localized W states. This localization suggests that the mobility may be better understood in the context of a hopping mechanism, as will be discussed further.

3.5 Nonequilibrium Synthesis

A deeper understanding of the as-synthesized n-type $FeWO_4$ is obtained by consideration of the synthesis conditions under which it was grown. To start, we consider the phase diagram of Fe-W oxide materials, allowing the chemical potential of O_2 to vary to account for temperature-induced changes.

The phase diagram is generated with the Materials Project [83] using the pymatgen [84] Grand Potential Phase Diagram function with fixed values of the chemical potentials of O_2 corresponding to partial pressures of O_2 ranging from 1.0 atm to 10^{-8} atm at a fixed temperature of 883K (610 °C, the annealing temperature from experiments). Above hull energies are calculated with respect to the most stable species in the entire Fe-W phase space at the selected partial pressure of O_2. In cases where the Materials Project had multiple entries for a given chemical formula, only the most stable entry is displayed. Note that the energies above hull for Fe_2O_3 and WO_3 are the same throughout the displayed regions of the phase diagram. Chemical potential of O_2 is calculated semi-empirically according to formula

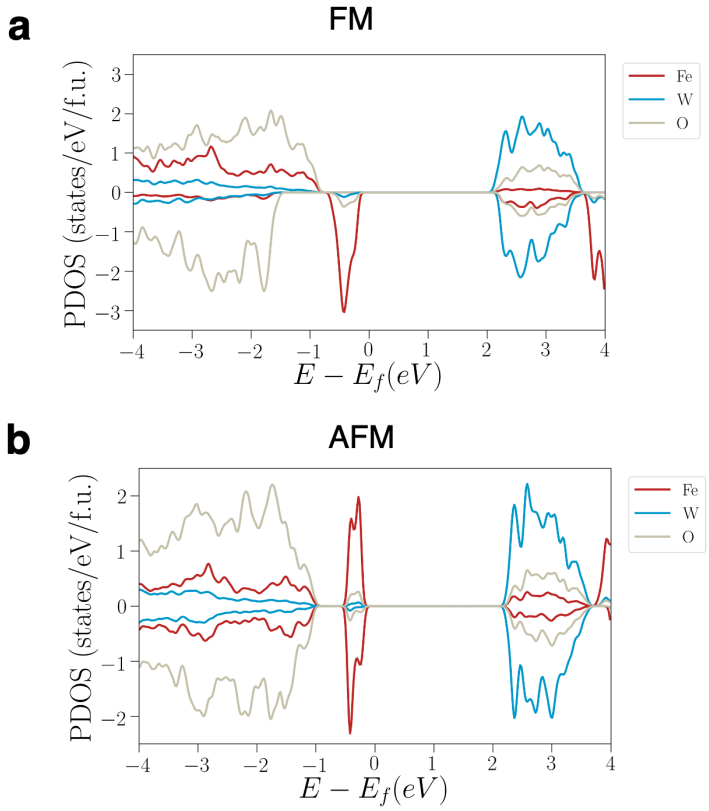


Figure 3.6: The element-projected density of states of $FeWO_4$ in the (a) FM and (b) AFM magnetic configurations. In both cases the VB is characterized by localized Fe states and the CB is characterized by localized W states.

(2) from Ong et al. [85] (Eq. 3.1), modified to use formation energies per atom in agreement with the pymatgen Grand Potential function.

$$\mu_{O_2}(T, p_{O_2}) = E_{O_2} + kT - TS_{O_2}^{T,p_0} + kT\ln\frac{p_{O_2}}{p_0} \tag{3.1}$$

where μ_{O_2} is the chemical potential of O_2 gas, p_{O_2} is the partial pressure of O_2, p_0 is a reference oxygen partial pressure, $S_{O_2}^{T,p_0}$ is the entropy of O_2 at the temperature of interest and at the reference pressure, and E_{O_2} is the DFT energy of oxygen gas. Formation energies of each chemical species are taken from the Materials Project DFT results and the temperature-dependent entropy of O_2 used in the chemical potential calculations are taken from NIST reference values (https://janaf.nist.gov/tables/O029.html) [86].

The grand potential analysis reveals that $FeWO_4$ is the most stable phase only at exceedingly low partial pressures of oxygen, below 10^{-4} atm. Above this partial pressure, Fe_2O_3 and

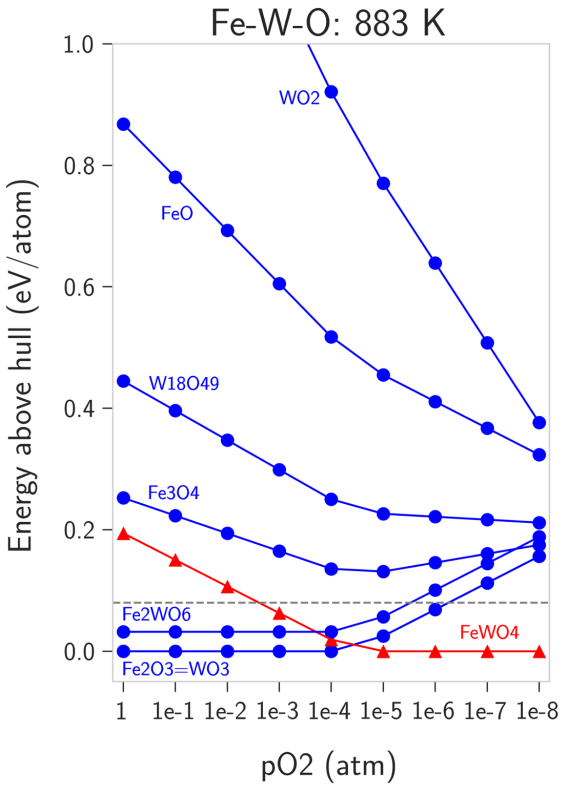


Figure 3.7: The energy above hull of Fe-W oxides at 883 K at varying partial pressures of oxygen gas. At higher partial pressures of oxygen Fe_2O_3 and WO_3 are the most energetically stable whereas at very low partial pressures of oxygen $FeWO_4$ is the most energetically stable.

WO_3 are the favored phases. Under experimental synthesis conditions, the partial pressure of O_2 was substantially higher than 10^{-4} atm, closer to $\sim 2\times10^{-1}$ atm.

In the experimental samples, regions of $FeWO_4$ always exhibited a passivation layer. For the initial $Fe_{0.56}W_{0.38}Bi_{0.06}O_z$ sample, a coating of Fe_2O_3 covered the $FeWO_4$ phase-pure region. This was also observed in the subsequently synthesized $Fe_{0.62}W_{0.38}O_z$ sample, where $FeWO_4$ only appeared in the thickest regions. From this, we draw the conclusion that n-type $FeWO_4$ was being grown through a nonequilibrium synthesis procedure. We hypothesize that oxygen is not diffusing completely through the sample during annealing, resulting in an oxygen-depleted region in which $FeWO_4$ forms. This is corroborated by the fact that high photoactivity was only observed in the sample grown with metal precursors, not the one with metal-oxide prescursors.

This observation offers insight into the n-type conductivity of $FeWO_4$. In order to be n-type, excess electrons must be present in the sample. Oxygen vacancies are a type of point defect that could contribute extra electrons, leading to n-type conductivity.

The formation energies of point defects in $FeWO_4$ have been investigated extensively via first-principles in prior work [87]. In this work, it was found that under typical synthesis conditions, starting with metal oxide precursors, the most energetically favorable point defects are Fe vacancies which lead to the formation of hole polarons. This confirms the previously observed p-type conductivity in $FeWO_4$. Under our nonequilibrium synthesis conditions with suppressed diffusion of oxygen throughout the film however, the formation of oxygen vacancies could become more energetically stable, lending itself to the production of electron polarons. In this prior work, the trapping energy (0.17 eV) and migration barrier (0.12 eV) of electron polarons are calculated to be lower than those of hole polarons. This suggests that electron polarons could account for the n-type conductivity and sufficiently high mobility to produce a high photovoltage.

3.6 Outlook

Using first-principles calculations, we have assisted in explaining the high photovoltage and n-type conductivity observed in n-type $FeWO_4$ synthesized by our expeirmental collaborators. Electronic structure calculations on pristine $FeWO_4$ indicate that the VB and CB are quite flat, consisting of localized Fe and W states respectively, such that band-like dispersion cannot account for the high photovoltage. Analysis of the energy above hull of $FeWO_4$ in the phase space of Fe-W oxides under experimental synthesis conditions reveals that $FeWO_4$ should only appear in a significantly oxygen-depleted environment. This aligns with the observation that a passivation layer of Fe_2O_3 appeared above the as-grown $FeWO_4$ films. We hypothesize that a nonequilibrium synthesis occurred, in which oxygen did not diffuse fully throughout the film. We suspect this resulted in the creation of oxygen vacancies. The n-type conductivity can be understood as arising from conductivity via electron polarons that are formed from excess electrons left behind by the oxygen vacancies.

This result is not without precedent. $CuWO_4$, another known tungstate photoanode material, has been observed experimentally to exhibit much higher photoactivity when it has a high concentration of oxygen vacancies [88]. This indicates that oxygen vacancies may be a valuable point defect to leverage in the development of novel high-performing photoanode materials.

Chapter 4

Band edge tuning of few-layer $MoS_{2(1-x)}Se_{2x}$ alloys for carbon dioxide reduction catalysis

This chapter is adapted in part from [89]. This work was done in collaboration with experimentalists in the Atwater group at Caltech. In this dissertation, we summarize the experimentalists' findings then outline our theory contributions. We perform first-principles calculations of the absolute band edge energies of various candidate crystal structures of $MoS_{2(1-x)}Se_{2x}$ alloys demonstrating their tunability as a function of the S to Se ratio to rationalize the experimental results, as published in [89]. Then, we perform further first-principles calculations to better understand the unexpected results for the band edge energies of small domains of $MoSe_2$ in a MoS_2 matrix, concluding that the dipole moment across the interface between the two TMD regions likely produces the calculated downward shift in the conduction band edge energy.

4.1 Introduction

Transition metal dichalcogenides (TMDs) with the general formula MX_2 (M = Mo,W; X = S,Se,Te) have received increasing attention for photocatalytic and electrocatalytic CO_2 reduction (CO_2RR) in recent years due to the high tunability of their electronic structure [72]. The most well-studied TMD, MoS_2, has been demonstrated to be an effective hydrogen evolution reaction (HER) catalyst with catalytically active sites at sulfur vacancies and edge sites [90, 91], as well as a successful catalyst of the CO_2RR [92]. CO_2RR can produce a wide array of different hydrocarbons, and controlling product selectivity is a challenge in designing effective catalysts for this application.

The absolute band edge positions of a CO_2RR catalyst determine which reduction reactions are accessible. In particular, the position of the conduction band minimum (CBM) must be higher in energy than the redox potential required to reduce CO_2 to the desired

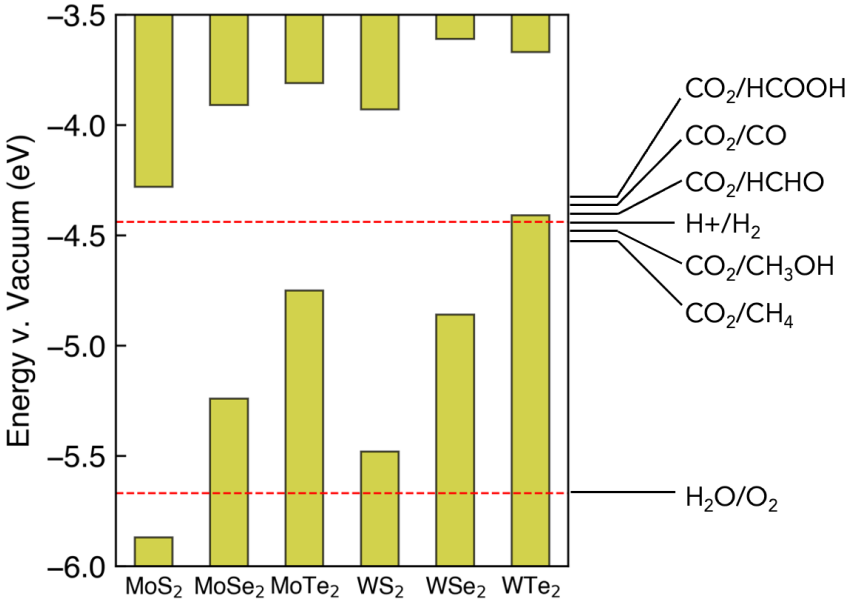


Figure 4.1: Absolute band edge positions of several TMDs relative to vacuum. The pH=0 redox potentials for the oxygen evolution reaction and hydrogen evolution reaction are indicated with red dashed lines. The redox potentials for reduction of CO_2 to various hydrocarbons are indicated as well. Note that under operating conditions these redox potentials will fall at different energies depending on many factors such as pH. This figure and the reported band edge energies are adapted from [12].

hydrocarbon product [66]. The band edges of TMDs increase in energy as the chalcogen is varied from S to Te and as the transition metal is varied from Mo to W [12] (Figure 4.1). As the CO_2RR redox potentials are clustered together in a small energy window, there is motivation to develop the ability to tune the absolute band edges of a catalyst at a very granular level, more granular than what can be achieved by simply varying the chalcogen or transition metal.

Alloys of different TMDs, with mixed concentrations of different chalcogens or different transition metals offer a potential avenue to granular control of absolute band edge positions. Despite much progress, studies of the influence of TMD alloy composition on electronic properties are very limited. Although several studies have used first-principles calculations to understand the electronic structure and optical properties of a variety of 2D vdW heterostructures [12, 93–96] they have mostly focused on the electronic band structure of monolayer TMDs.

Monolayer TMDs have received greater amounts of attention in recent years because of

the novel properties that emerge at the monolayer limit, such as large exciton binding energies and the transition to a direct band gap (as opposed to the indirect band gap observed in multilayer TMDs) [9, 11]. However, for catalytic applications, monolayer TMDs are not necessarily the best candidates. Large exciton binding energies can inhibit production of free, unbound electrons and holes which prevents them from being donated for reduction or oxidation. Further, multilayer TMDs should exhibit better stability under aqueous conditions than monolayers [97].

Most prior theoretical studies have not linked electronic structure calculations with direct experimental measurements of the absolute band edge positions of TMD alloys. In this work, we perform a combined experimental and theoretical investigation of the effect of elemental composition on electronic band structure and absolute band edges of few-layer TMDs.

4.2 Experimental Results

The experimentalists in the Atwater group at Caltech synthesized few-layer MoS_2 using metal-organic chemical vapor deposition (MOCVD) on a silicon wafer. Next, they used a thermal selenization process by placing Se powder in a furnace and flowing H_2/N_2 gas through the chamber (Figure 4.2a,b) to mix Se into the few-layer MoS_2. This was done several times to produce $MoS_{2(1-x)}Se_{2x}$ alloys with varying Se content (x = 0.12, 0.18, 0.23, 0.26, and 1).

The valence band maximum (VBM), work functions, and Se concentrations were measured using X-ray photoemission spectroscopy (XPS). Next, optical absorption measurements were performed to determine the band gap of each alloy. The CBM was taken to be the VBM plus the optical band gap. The measured band edges relative to vacuum are shown in Figure 4.2c. Amongst the alloys, there is a clear upward trend in the VBM and CBM positions with increasing Se concentration. Relative to the pristine MoS_2 and $MoSe_2$ band edges though, the alloys all exhibit a downward shift in VBM position. This was attributed to water molecules adsorbing on the surfaces of the alloys which is suspected to have shifted the band edge energies. The primary take-away from the experimental results is that the band edges can indeed be tuned by varying the Se concentration.

4.3 Crystal Structure Candidates

While the experimentalists were able to determine the fraction of Se in each alloy, they were not able to confirm the exact crystal structure or distribution of Se throughout the MoS_2 matrix. This makes it necessary for first-principles calculations to be performed on a variety of different potential crystal structures.

Three extreme cases are considered. First, lateral heterostructures, with domains of $MoSe_2$ embedded in MoS_2 (Figure 4.3a). Second, vertical heterostructures, with Se only

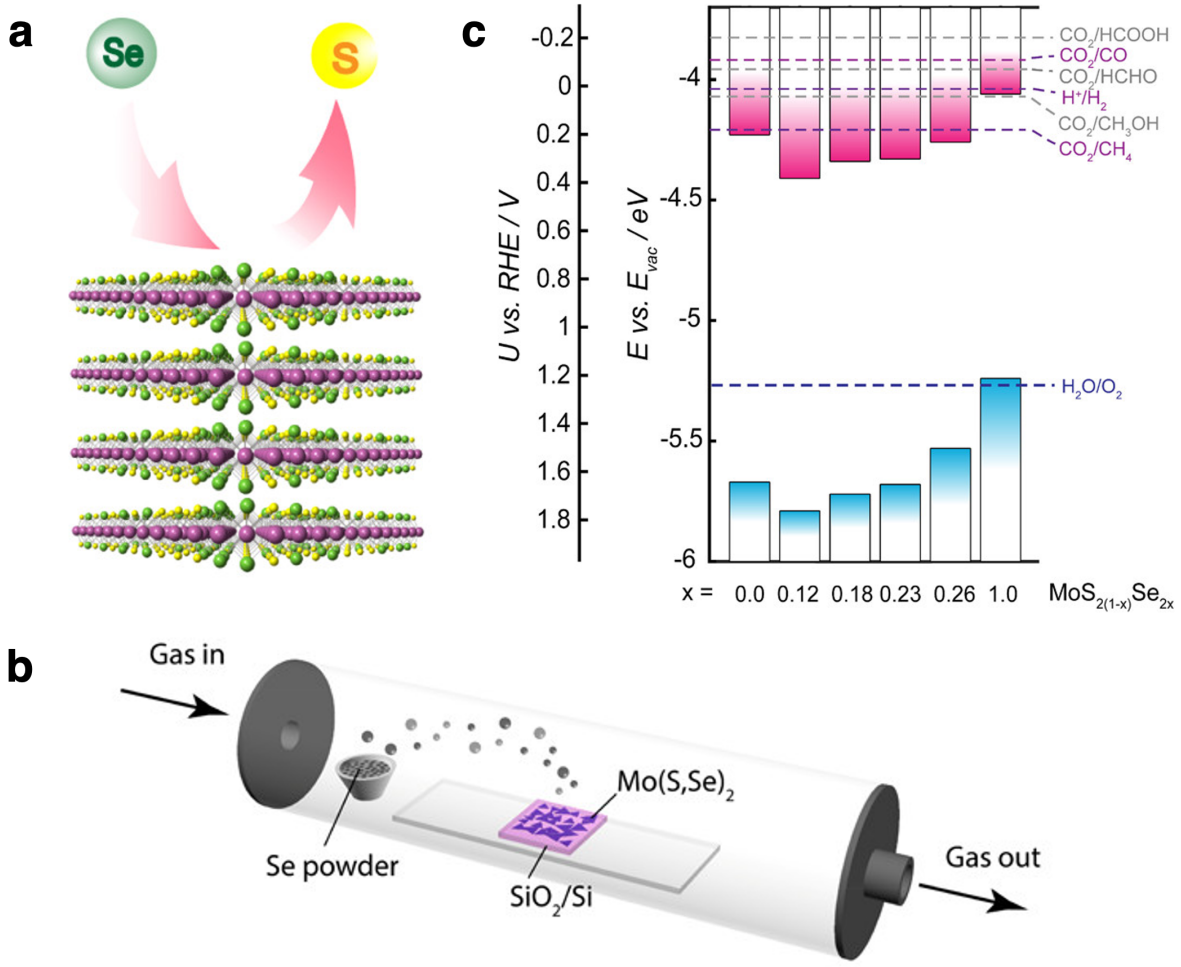


Figure 4.2: Schematic of $MoS_{2(1-x)}Se_{2x}$ alloy synthesis procedure. (a) Few-layer MoS_2 was synthesized and Se was then substitutionally incorporated into S sites. (b) The Se substitution in MoS_2 was performed by using gas to sprinkle Se powder onto the few-layer MoS_2 sample. (c) The experimentally measured band edges. This figure is reproduced from [89].

penetrating the top layers (Figure 4.3b). Third, heterogeneous alloys, with Se uniformly distributed throughout the crystal (Figure 4.3c).

4.4 Electronic Structure and Absolute Band Edges

The electronic structure of each candidate alloy crystal structure is calculated in order to compare to the experimental data and gain insight into the crystal structures that may have been generated in the selenization process.

First-principles ionic and electronic structure calculations are performed using density functional theory (DFT) with a plane-wave basis and projector augmented wave (PAW) potentials [61] as implemented by the Vienna *ab initio* simulation package (VASP) [62, 63]. All calculations are performed in the generalized gradient approximation (GGA) with additional van der Waals corrections using the vdW density functional rev-vdW-DF2 to incorporate dispersion forces [60]. For homogeneous alloys and vertical heterostructures, a plane- wave energy cutoff of 750 eV is used with a 10×10×1 Γ-centered k-point mesh for structural relaxations, band structures, and slab calculations. The most stable homogeneous alloys are determined by considering all symmetrically distinct arrangements of S and Se in a 2×2×1 bulk supercell. A quadrilayer slab with 20 Å of vacuum is used for structural relaxation of the vertical heterostructures. All forces are converged to < 1 meV/Å. Calculations of the electrostatic potential along the c-axis of quadrilayer slabs with 20 Å of vacuum for each system are performed to determine absolute band edges. The absolute position of the VBM relative to the electrostatic energy of the vacuum region is taken as the absolute VBM position. The conduction band minimum (CBM) is determined by adding the bulk band gap to the slab VBM. For small lateral domain calculations, bulk structural relaxations are performed with a plane-wave energy cutoff of 750 eV used with a 2×2×1 Γ-centered k-point mesh on a 10×10×1 supercell of MoS_2 with regions of $MoSe_2$ of varying sizes. All forces are converged to < 0.01 eV/Å. A quadrilayer slab calculation with 15 Å of vacuum is performed using a 600 eV energy cutoff and a 2×2×1 k-point mesh to determine the absolute positions of the VBM and CBM. An empirical correction scheme is further applied to the calculated band edges. The differences between the experimental band edges and DFT band edges for pristine MoS_2 and $MoSe_2$ are calculated then linearly interpolated across the alloys as a function of Se content x in order to generate empirical corrections for the DFT band edges.

The calculated values of the VB and CB edge energies relative to vacuum are shown in Figure 4.3d,e,f. Homogeneous alloys and vertical heterostructures exhibit a clear upward trend of the the band edges from x = 0 to x = 1. This indicates that generally this trend should be expected irrespective of how deeply the Se penetrates into the MoS_2 vertically, so long as it penetrates uniformly in the lateral direction.

In the case of the lateral heterostructures with small domains of $MoSe_2$ embedded in MoS_2, a very different trend emerges. While the VB edge rises consistently with increasing Se concentration, the CB edge shifts to lower energy than the CB edge positions of either pristine TMD and is insensitive to the fraction of Se.

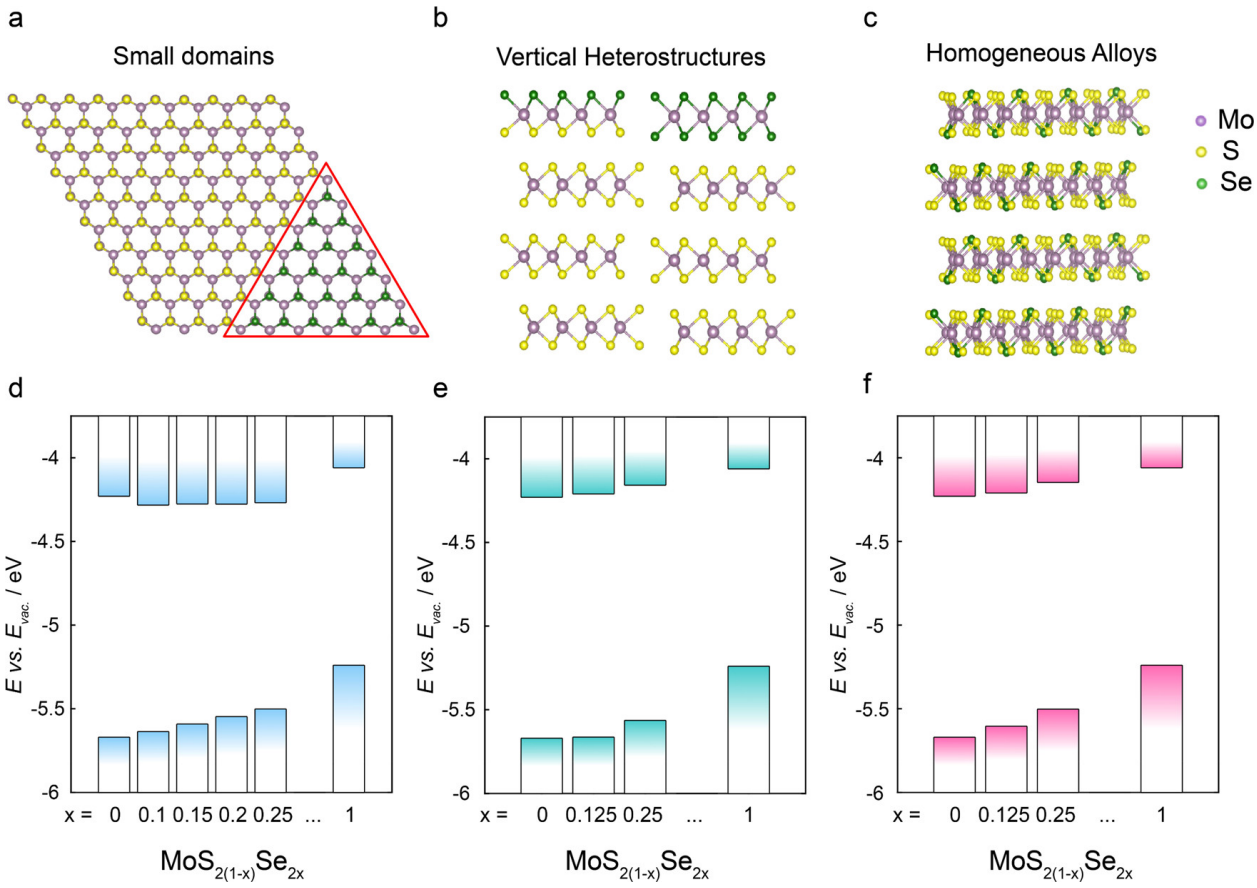


Figure 4.3: Schematics of three different candidate $MoS_{2(1-x)}Se_{2x}$ alloy crystal structures (a) lateral heterostructures with small domains of $MoSe_2$ (b) vertical heterostructures with Se only substituted on the top layers (c) homogeneous alloys with Se homogeneously distributed throughout the crystal. The calculated absolute band edges of each of these three candidate crystal structures are shown in (d), (e), and (f) respectively. This figure is reproduced from [89].

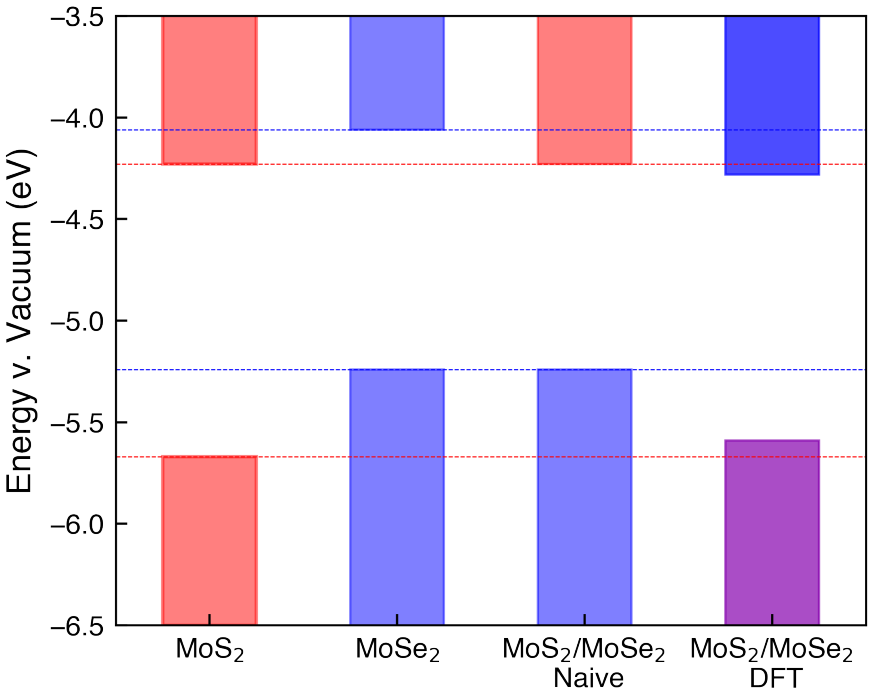


Figure 4.4: The experimental band edges of MoS_2 and $MoSe_2$, the expected naive band edge positions, and the actual calculated band edges of the small lateral domain structure with 15% Se content, with empirical corrections. Red bars represent dominant contributions from MoS_2 at the indicated band edge, blue bars represent dominant contributions from $MoSe_2$, and purple bars represent mixed contributions from both regions. Dashed lines indicate the positions of the experimental band edges for each pristine TMD for visual clarity and to emphasize the discrepancy between the calculated values and the expected band edges.

4.5 Interfacial Dipole Effects in Small Domains

The unexpected behavior of the small lateral domains, whose CBMs exhibit insensitivity to Se concentration and a consistently lower CB edge energy than that of either pristine TMD, warrants further investigation.

Naively one might expect the VBM to have $MoSe_2$ character and fall at the same energy as the pristine $MoSe_2$ VBM. Similarly, one might naively expect the CBM to have MoS_2 character and fall at the same energy as the pristine MoS_2 CBM as depicted in the third column of Figure 4.4. Instead, the CBM has predominantly $MoSe_2$ character and the VBM has a mix of character from both TMDs. The wavefunctions at the VB and CB edges are plotted in Figure 4.5.

Three possible explanations for the unexpected behavior of the CB position are (i) quan-

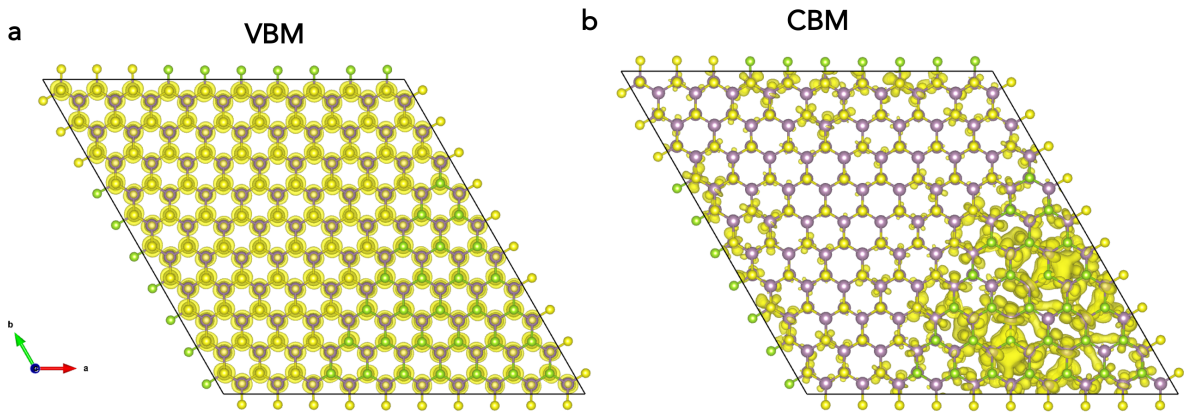


Figure 4.5: The square of the wavefunction at the VBM and CBM of a small lateral domain heterostructure. (a) The VBM is distributed throughout both regions of the heterostructure. (b) The CBM is localized in the $MoSe_2$ region.

tum confinement (ii) strain and (iii) the dipole moment across the interface between MoS_2 and $MoSe_2$.

Quantum confinement in low-dimensional systems is well-known to significantly alter the electronic structure of materials [19]. For example, nanoparticles have very different band gaps than their bulk counterparts. A simple picture to understand this phenomenon is to draw a parallel to the quantum particle in a box.

A particle confined to a box with side lengths L_i by infinite potentials in the surrounding regions has an eigenspectrum [26]

$$E_{\{n_i\}} = \frac{\hbar^2\pi^2}{2m}\sum_i \left(\frac{n_i}{L_i}\right)^2 \tag{4.1}$$

where n_i are the principal quantum numbers and m is the mass of the particle. In the case of a 2D system, the energy difference between the ground state and the first excited state scales as $\sim \frac{1}{Area}$. In a solid state system, this produces an increase in the band gap that scales as the inverse of the area. In the small lateral heterostructure with 10% Se content, the $MoSe_2$ region has a side length of 11 Å. A back of the envelope calculation reveals that this should produce a 1.4 eV increase of the band gap in the 10% Se case. To the contrary, the band gap in the $MoSe_2$ region decreases. Hence, quantum confinement does not explain the CB edge behavior.

Strain is also known to affect the electronic structure of TMDs [49–51]. In the $MoSe_2$ region, the lattice parameters are compressed relative to pristine $MoSe_2$ which is expected

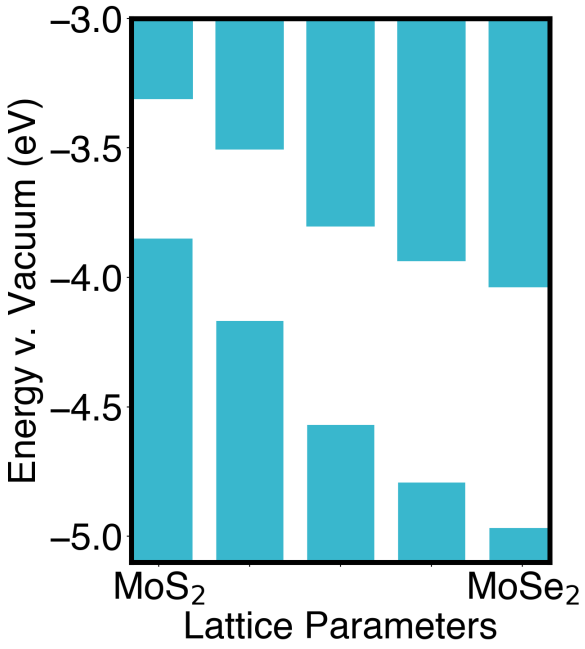


Figure 4.6: The band edges of $MoSe_2$ at varying degrees of in-plane biaxial strain. On the right $MoSe_2$ has its equilibrium lattice parameters. On the left, the lattice parameters have been compressed to those of MoS_2.

to alter the band edges and band gaps. Band edge calculations performed on $MoSe_2$ with systematically decreasing lattice parameters from the pristine $MoSe_2$ lattice parameters to the MoS_2 lattice parameters reveal that in-plane compressive biaxial strain shifts the VB and CB edges to higher energy, rather than producing a decrease in the CB edge position (Figure 4.6). This indicates that strain is also not a sufficient explanation for the CB edge reduction.

Finally, a dipole moment exists perpendicular to the interface between the MoS_2 region and $MoSe_2$ region. To quantify the effect of this dipole moment on the electrostatic potential in each region, the on-site electrostatic potential is calculated for each Mo ion along the diagonal, as depicted in Figure 4.7a. The electrostatic potential on each Mo ion is roughly the same throughout the MoS_2 region, then increases in the $MoSe_2$ region (Figure 4.7b).

The difference between the Mo on-site potentials in the two regions is ∼0.51 eV. The difference between the CB edge energy for pristine $MoSe_2$ and that for the heterostructure with 10% Se content is ∼0.22 eV. These values are the same order of magnitude and are the most promising candidate explanation for the unexpected band edge behavior of the CB in lateral domain heterostructures of MoS_2 and $MoSe_2$.

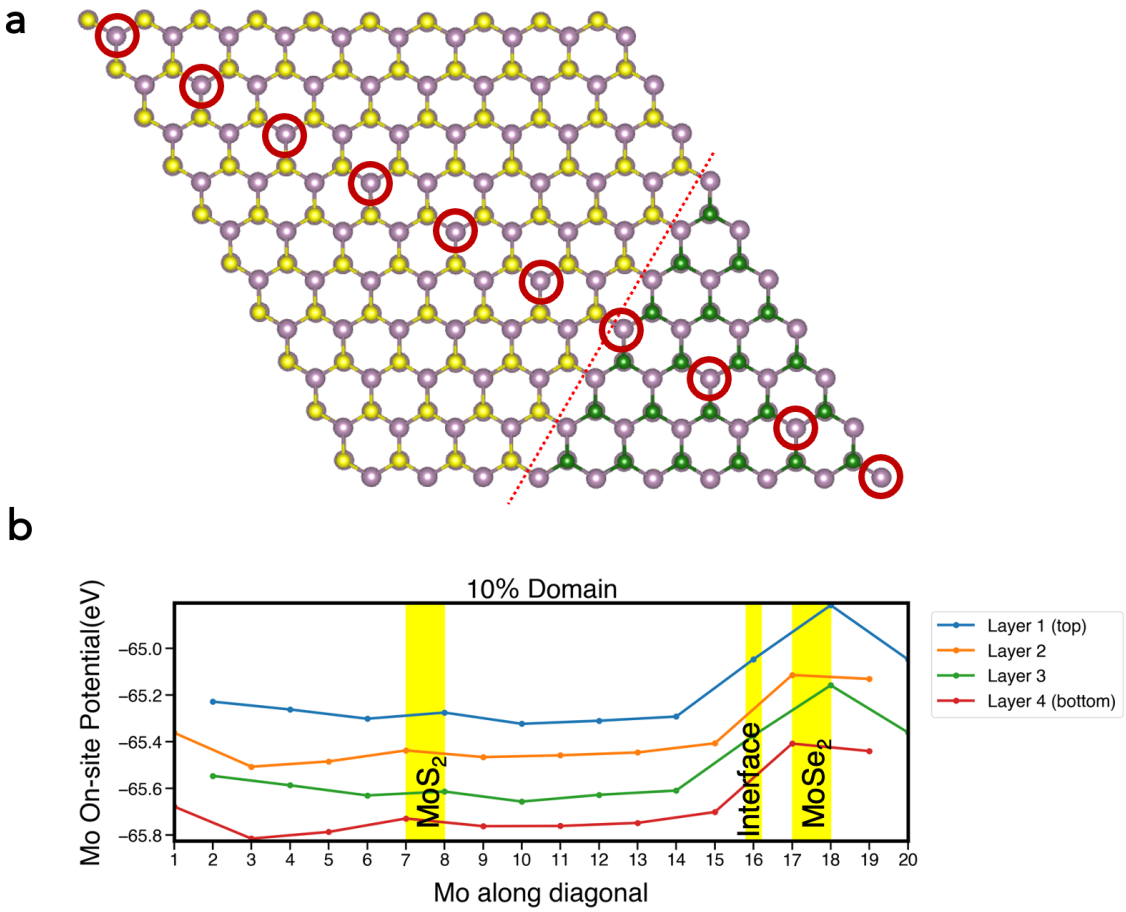


Figure 4.7: Calculation of the dipole moment across the $MoS_2/MoSe_2$ interface. (a) Each Mo site on which the on-site electrostatic potential is calculated. (b) The on-site electrostatic potential for each Mo site along the diagonal for the heterostructure with 10% Se, indicating a change that occurs as the interface is crossed. Representative MoS_2, Interface, and $MoSe_2$ regions are indicated with labelled yellow bars.

4.6 Outlook

In collaboration with experimentalists in the Atwater group at Caltech we have performed density functional theory calculations on the absolute band edge energies of $MoS_{2(1-x)}Se_{2x}$ alloys. These calculations have revealed that homogeneous alloys and lateral heterostructures can produce tunable band edge energies which has applications for developing CO_2RR catalysts with enhanced product selectivity. Further, we studied the unexpected CB edge energetics of small lateral domains of $MoSe_2$ in MoS_2 and determine that the consistent reduction in the CB energy is likely a result of the interfacial dipole across the $MoS_2/MoSe_2$ interface. These results offer insight both into methods for fine grained tuning of absolute band edges for catalysis applications as well as the complexity of lateral heterostructures as an area of future research.

Chapter 5

Band edge tuning of Janus WSSe-ZnO heterostructures

5.1 Introduction

Identification of materials with tunable electronic properties that can be optimized for visible light absorption and appropriate band edge energies relative to chemical reactions of interest is important for the development of photocatalytic production of solar fuels, as discussed in Chapter 4. Pristine bulk and monolayer TMDs have shown some success for photocatalysis, however they exhibit certain known limitations. For example, pristine MoS_2, which has been demonstrated to catalyze the hydrogen evolution reaction (HER) and CO_2RR, exhibits rapid carrier recombination, has band edge energies that do not inherently align well with those of the relevant redox potentials requiring an applied bias, and tends to denature under aqueous operating conditions [89–92]. This motivates the search for novel methods of tuning the electronic and structural properties of TMDs for improved photocatalytic performance.

Efforts to tune the absolute band edge energies of photocatalyst materials is an active area of research motivated by the desire to engineer materials that can catalyze specific desired chemical reactions, for example to improve product selectivity, as discussed in Chapter 4. Methods for tuning band edges often involve changing the elemental composition or geometry of a material. Examples that have been probed experimentally include changing the element used for the second type of cation in ternary metal vanadate photoanodes or producing alloys of TMDs with controllable fractions of mixed chalcogens or transition metals [47, 89]. An alternative method is introducing a polar material in proximity to the photocatalyst whose dipole moment can rigidly shift the band edges of the photocatalyst. Examples of this approach in past work include generating a heterostructure of a monolayer TMD on top of the polar surface of the bulk ferroelectric $BiFeO_3$ or passivating the surface of a bulk semiconductor, like CdSe, with polar surface ligands [98, 99].

vdW heterostructures, constructed by stacking layers of different 2D materials, are a vast and well-motivated search space for designing photocatalysts with tunable band edges

because they have the potential to combine or modulate properties of the individual 2D materials. TMDs in particular are a commonly studied form of 2D material used in vdW heterostructures [6]. The clean interfaces between non-chemically bound monolayers in vdW heterostructures also mitigates the limitations of bulk heterostructures, such as interfacial reconstruction that can change the local electronic structure.

Monolayer Janus TMDs, with chemical formula MXY (M=Mo,W; X,Y = S,Se,Te), have different chalcogen ions on either side of the monolayer. This gives rise to an out-of-plane dipole moment generating a pristine polar surface [14, 100]. While polar surfaces are generally unstable, monolayer Janus TMDs have been successfully synthesized using a modified chemical vapor deposition technique [101, 102]. These materials exhibit novel properties for TMDs including Rashba splitting and piezoelectricity [100, 103, 104]. The intrinsic dipole moment in Janus TMDs assists in spatially separating excited carriers and elongating the carrier recombination time by orders of magnitude relative to traditional MX_2 TMDs [13–15]. Further, it has been shown that TMDs that contain Se or Te exhibit better aqueous stability than those that contain only S [97]. As such, Janus TMDs may have advantages over traditional TMDs for photocatalytic or other light harvesting applications. In fact, recent work has explored the effectiveness of Janus TMD heterostructures for water splitting applications [105].

Another 2D material that has recently begun to receive experimental and theoretical attention is monolayer ZnO, which is polar as well, with a bipartite hexagonal lattice similar to hexagonal-BN but with a small amount of buckling such that the Zn and O are close to being, but are not exactly, coplanar [106–112]. Monolayer ZnO is a wide band gap material, with a reported gap of 4.48 eV [113]. While the band gap is too large for efficient absorption of visible light, the earth abundance of the constituent elements makes it a material of interest for green energy technology, should a method of modifying its electronic structure be accessible. Monolayer ZnO has been synthesized both on metal substrates and in freestanding monolayers [106–109, 113]. Prior first principles studies have investigated the electronic structure of ZnO under strain and with various defects and dopants, reporting that the band gap of ZnO can be effectively tuned by these methods, with tensile strain producing calculated band gap reductions of up to 0.5 eV at 9% tensile strain and Zn and O vacancies producing calculated band gap reductions up to 2 eV [110–112]. To our knowledge the aqueous stability of monolayer ZnO has not been measured experimentally, however, oxides in general often exhibit reasonable stability under aqueous conditions, accounting for their frequent use in photocatalysis [1, 97].

In this work we consider vdW heterostructures of the Janus TMD WSSe and monolayer ZnO and perform density functional theory (DFT) calculations to study the electronic structure of these heterostructures with an eye towards improving upon the limitations of pristine TMDs for potential photocatalytic applications. In particular, WSSe is selected because W-based TMDs tend to have smaller band gaps than Mo-based TMDs and absolute band edge positions shifted to higher energies relative to those of Mo-based TMDs, enhancing their ability to absorb a large fraction of the visible spectrum and to have conduction band edges that are inherently at high enough energies to donate electrons for the HER and

CO_2RR [12]. Further, as mentioned, the intrinsic dipole moment in WSSe assists in charge separation, mitigating the rapid carrier recombination rates that limit the efficiency of MX_2 TMDs [13–15]. The small out of plane buckling in ZnO gives rise to an out-of-plane dipole moment as well. These vdW heterostructures, consisting of two elementally earth-abundant materials that both host dipole moments, has the potential to give rise to novel means of tuning the band edge energies of a photocatalyst.

Prior first-principles work has suggested that Janus WSSe-ZnO vdW heterostructures can assume a Type II band alignment which can further assist with charge separation [114]. This prior work also found that these heterostructures have favorable band edge positions for water splitting. In this work we build upon these prior first-principles calculations of Janus WSSe-monolayer ZnO heterostructures and demonstrate how the electronic structure, including the band gap and band edge alignment, can be tuned by in-plane biaxial strain, out-of-plane uniaxial strain, and applied out-of-plane electric field.

5.2 Electronic Structure Methods

First-principles calculations on Janus WSSe - ZnO heterostructures are performed using density functional theory (DFT) with a plane-wave basis and projector augmented wave (PAW) pseudopotentials [61] as implemented in the Vienna *ab initio* Simulation Package (VASP) [62, 63]. Geometry optimization calculations are performed using the generalized-gradient approximation (GGA) as implemented by Perdew, Burke, and Ernzerhof (PBE) [23] in addition to van der Waals dispersion corrections using the Grimme-D3 method [37]. For crystal structure relaxations, an energy cutoff of 520 eV is used with a 21x21x1 Γ-centered k-grid. Structures are relaxed until forces are less than 1 meV/Å. The relaxed a-lattice parameter is 3.26 Å. The relaxed a-lattice parameter of WSSe is 3.23 Å and that of ZnO is 3.29 Å, meaning that the hetreostructure unit cell corresponds to < 1 % tensile strain applied to WSSe and < 1 % compressive strain applied to ZnO. The calculated lattice parameter for ZnO is in agreement with prior work [115], as is that of WSSe [116]. A vacuum layer of ∼25 Å is included, as are dipole corrections along the c-axis to account for the finite out-of-plane dipole moments of these heterostructures. Binding energies of different stacking orientations are calculated using

$$E_B = E_{WSSe-ZnO} - E_{WSSe} - E_{ZnO}, \tag{5.1}$$

comparing the total energy of the heterostructures to the energies of the isolated monolayers. Geometry optimizations for crystal structures with biaxial strain are performed by modifying and fixing the a-lattice parameter and allowing the internal coordinates of the atoms to relax. Valence band alignment and band structure calculations are performed using the hybrid functional HSE06 [33, 34]. A 9x9x1 k-grid is used to generate the charge density for non-self-consistent HSE06 calculations. The absolute valence band position is determined by calculating the plane-averaged electrostatic potential along the c-axis in order to determine the valence band maximum (VBM) energy relative to the vacuum energy. The conduction

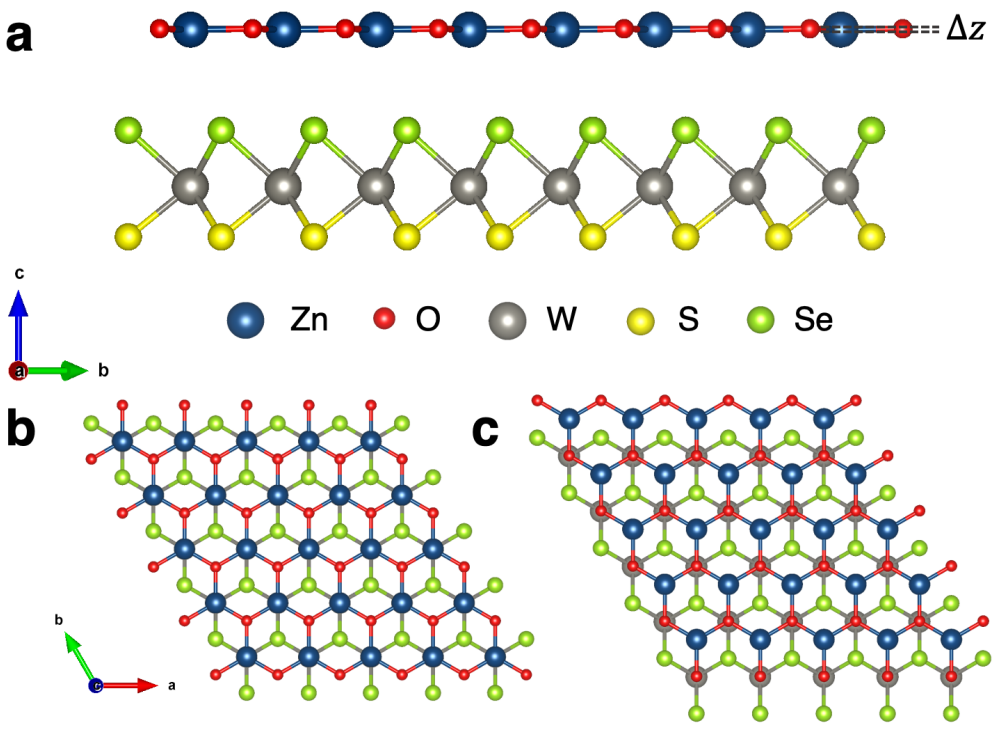


Figure 5.1: Stacking configurations of Janus WSSe-ZnO heterostructures. (a) Side view with Se on the same side as ZnO (AB-I-Se). The buckling Δz in ZnO gives rise to its dipole moment. (b) Top view in Type I registry with AB stacking with W and Zn aligned and Se on the same side as ZnO (AB-I-Se) (c) Top view in Type II registry with AB stacking with W and O aligned and Se on the same side as ZnO (AB-II-Se).

band minimum (CBM) energy is determined by adding the HSE06 band gap to the absolute VBM position. The limitations of this approach when using hybrid functionals are discussed in Chapter 2, however we expect to capture trends effectively. Electric field calculations are performed by applying a uniform out-of-plane sawtooth external potential to the unit cell, generating a constant field perpendicular to the bilayer. Phonon calculations are performed using the frozen phonon method as implemented by the phonopy package [71]. PBE exchange-correlation is used for the frozen phonon calculations with a 5x5x1 supercell and a 5x5x1 k grid.

Stacking Configuration	Binding Energy (eV/unit cell)	a-lattice parameter(Å)
AA-I-Se	-0.217	3.255
AA-I-S	-0.202	3.255
AA-II-Se	-0.262	3.259
AA-II-S	-0.257	3.259
AB-I-Se	-0.276	3.257
AB-I-S	-0.269	3.257
AB-II-Se	-0.277	3.257
AB-II-S	-0.260	3.257

Table 5.1: Binding energies and relaxed in-plane lattice parameters of WSSe-ZnO heterostructures with different stacking orientations. AA and AB refer to the stacking pattern, whether the two hexagonal lattices are aligned on top of one another or shifted. I and II refer to whether the W is aligned below the Zn or the O atom of ZnO. S and Se refer to which chalcogen is facing the ZnO.

5.3 Crystal Structures

The binding energies of eight high symmetry stacking orientations of WSSe with ZnO are calculated in order to determine the lowest energy structures. Type I registry with W and Zn aligned on top of one another along the surface normal is compared to Type II registry with W and O aligned (Figure 5.1b,c), as are AA and AB stacking orientations. Additionally, the two orientations of the Janus monolayer (S facing ZnO or Se facing ZnO) are considered. Due to the buckling in ZnO it could be possible to orient that monolayer two ways as well, with the Zn closer to the WSSe than the O and vice versa. In this study we focus on the case where ZnO is oriented such that Zn is closer to the WSSe, which is the buckling pattern observed when geometry optimization is performed on heterostructures in which the ZnO is initialized with coplanar Zn and O. We expect proximity of the positively charged Zn to the negatively charged chalcogen to be favorable compared to having the negatively charged O in closer proximity to the negatively charged chalcogen. The three most stable structures are AB-I-Se, AB-II-Se and AB-I-S (Table 5.1) where the chalcogen indicated in the stacking name is the chalcogen facing the ZnO.

The phonon band structures of each of these three most stable stacking patterns are calculated to determine whether these structures are dynamically stable (Figure 5.2). The AB-II-Se stacking pattern exhibits imaginary optical modes and is determined to be unstable. The AB-I-S and AB-I-Se stacking patterns do not exhibit any such instabilities so these two structures are selected for further analysis. It should be noted that the binding energy of the AB-II-Se stacking pattern differs from that of AB-I-Se by an extremely minimal amount, $\sim$1 meV per unit cell or $\sim$0.2 meV per atom, making them energetically nearly degenerate within the precision limits of the methods employed in this work. Analysis of the unstable

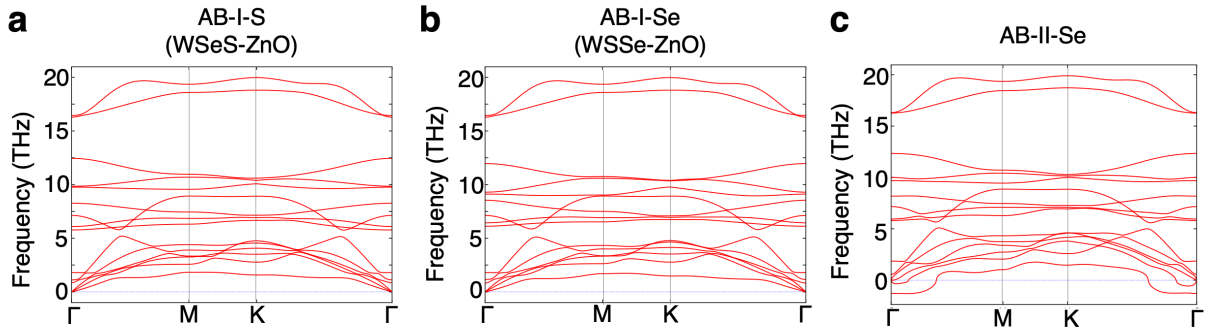


Figure 5.2: The phonon band structures of the three stacking configurations with the largest binding energies (a) AB-I-S (WSeS-ZnO), (b). AB-I-Se (WSSe-ZnO), and (c) AB-II-Se. AB-II-Se exhibits imaginary optical modes indicating that the structure is not stable.

phonon modes near the Brillouin zone center in the phonon band structure of the AB-II-Se structure reveals that they correspond to lateral sliding of the two layers relative to one another. Effectively, the dynamical instability in the AB-II-Se stacking pattern promotes realignment of the layers into a preferred stacking pattern. Further analysis of energetic barriers to sliding and dynamical instabilities driving sliding in these heterostructures would be a valuable topic for future study.

Going forward, we shall refer to the AB-I-S and AB-I-Se heterostructures as WSeS-ZnO and WSSe-ZnO respectively to make it clear which orientation of WSSe with respect to ZnO we are referring to, with the final chalcogen in the Janus TMD label referring to the chalcogen that faces the ZnO monolayer. Discussion of these heterostructures, without reference to any particular configuration, will be indicated with the term Janus TMD-ZnO to reduce ambiguity.

The band structures of the WSeS-ZnO and WSSe-ZnO stacking patterns are calculated using HSE06 (Figure 5.4b,e) using the crystal structures obtained from structural relaxation using PBE+D3. In all cases the valence band (VB) and conduction band (CB) are dominated by WSSe orbital contributions. The only notable mixing that occurs is in the WSSe-ZnO structure with Se facing ZnO – some hybridization between the two layers occurs in the CB at the Γ point. The band gaps for both structures are direct gaps at K and have the same magnitude as the band gap of monolayer WSSe (Table 5.2). These heterostructures exhibit a Type I band edge alignment with the ZnO band edges straddling the WSSe band edges.

Prior work investigating Janus TMD-ZnO heterostructures using HSE found that the band edges were Type I when S faced the ZnO (WSeS-ZnO) but Type II when Se faced the ZnO (WSSe-ZnO) [114], inconsistent with our results. It should be noted that our calculated PBE band structures of both WSeS-ZnO and WSSe-ZnO exhibit Type II alignment, with the

Stacking Configuration	HSE Band Gap (eV)
WSSe	2.14
ZnO	3.73
WSSe-ZnO	2.13
WSeS-ZnO	2.13

Table 5.2: Band gaps of monolayer WSSe, monolayer ZnO, and the two most stable stacking configurations. The band gaps of the heterostructures are very similar to that of monolayer WSSe.

Stacking Configuration	Strain(%)	Interlayer Distance (Å)	Zn-O bond length (Å)	W-Se bond length (Å)	W-S bond length (Å)	HSE Band Gap (eV)
WSSe-ZnO	-5	3.20	1.79	2.52	2.39	2.08
WSSe-ZnO	0	3.08	1.88	2.54	2.42	2.13
WSSe-ZnO	5	2.97	1.97	2.57	2.46	1.14
WSeS-ZnO	-5	3.07	1.79	2.52	2.39	2.09
WSeS-ZnO	0	2.96	1.88	2.54	2.43	2.13
WSeS-ZnO	5	2.87	1.97	2.57	2.47	1.12

Table 5.3: The interlayer distance between the top-most chalcogen and the ZnO layer and the HSE band gaps for 5% compressive strain, no strain, and 5% tensile strain for the WSSe-ZnO and WSeS-ZnO stacking configurations.

VBM dominated by orbitals of ZnO character (see Appendix I: Figure 5.8). Our calculated HSE band gap for WSSe is similar to that of the prior work. Our calculated lattice parameters for ZnO are the same as those in this prior work, however, our converged HSE band gap for ZnO is significantly larger, 3.73 eV versus 3.10 eV, which could explain the discrepancy. The reported experimental band gap of monolayer ZnO is 4.48 eV [113], significantly larger than our calculated value of 3.73 eV, making it reasonable to assume that these heterostructures would indeed exhibit Type I alignment experimentally.

5.4 In-plane Biaxial Strain and Out-of-plane Uniaxial Strain

In-plane biaxial strain has been shown in prior work to be a useful knob that can be turned to tune the electronic structure of TMDs [49–53]. In 2D materials, strain can be applied

in a variety of ways, including by transferring the 2D material to a flexible substrate that can then be bent, to a piezoelectric substrate whose dimensions can be modified with an electric field, or to an array of nanopillars [53]. To investigate the effect of in-plane biaxial strain on the Janus TMD-ZnO heterostructures we perform band edge alignment calculations with varying amounts of tensile and compressive biaxial strain, up to 5%, calculating the absolute VBM position relative to vacuum and the band gap using HSE. Experiments have reported that TMDs can withstand large degrees of strain. For example, one experiment used an atomic force microscopy cantilever, reporting that monolayer MoS_2 did not break until a strain between 6-11% was reached [117]. In all cases the heterostructures are fully optimized at the stretched or compressed lattice parameters, with the internal coordinates allowed to relax. In the relaxed structures, a small amount of buckling occurs in the ZnO layer, with the plane of the O atoms ∼0.03 Å above the plane of the Zn atoms in the unstrained case (Figure 5.3a). The interlayer separation between the topmost chalcogen and the ZnO layer and the bond lengths for the non-strained, largest compressive biaxial strains, and largest tensile biaxial strains are listed in Table 5.3. In general, the interlayer distance is 0.1 Å larger when Se faces the ZnO layer than when S faces the ZnO layer. The Zn-O, W-Se, and W-S bond lengths increase and decrease comparably for both stacking configurations for biaxial tensile and compressive strain respectively.

The degree of buckling in the ZnO, defined as the difference between the z-position of the O ion and that of the Zn ion, is also a function of biaxial strain percent, with compressive biaxial strain producing a large increase in the buckling and tensile biaxial strain producing a smaller decrease in the buckling (Figure 5.3a). At 5% in-plane compressive biaxial strain the buckling in the ZnO layer increases up to more than 0.12 Å while at 5% tensile biaxial strain the ZnO layer buckling decreases to 0.015 Å. We calculate the plane-averaged electrostatic potential energy across the ZnO monolayers alone for different amounts of buckling and find that the potential energy has different values on either side of the ZnO, as it should for a polar material. Further, this potential energy difference scales linearly with the magnitude of the buckling as would be expected from a simplified picture of a dipole moment which scales linearly with separation of the positive and negative charges [26]. This indicates that the biaxial in-plane compressive strain is a direct means of tuning the dipole moment of the ZnO monolayer.

The HSE band structures of the strained structures are displayed in Figure 5.4. In both stacking configurations tensile biaxial strain significantly decreases the band gap and makes the gap just barely indirect, with the Γ point in the VB increasing in energy slightly above the K point. The K-K transition for WSSe decreases as well. While the dominant contributions to the VBM and CBM in a TMD are generally from Mo or W d orbitals, d_{xy} and $d_{x^2-y^2}$ for the VBM at K and d_{z^2} for the CBM at K, this effect can be rationalized in the context of the smaller, but nontrivial, chalcogen p-orbital contributions. These orbital contributions are predominantly in-plane p_x and p_y (see Chapter 6 Figure 6.3). In a simplified bonding-antibonding orbital picture, the lateral separation between the chalcogens can modulate the K-K transition energy, with closer proximity increasing the K-K gap and larger separation decreasing the K-K gap. Compressive biaxial strain has a significant effect on the CB, with

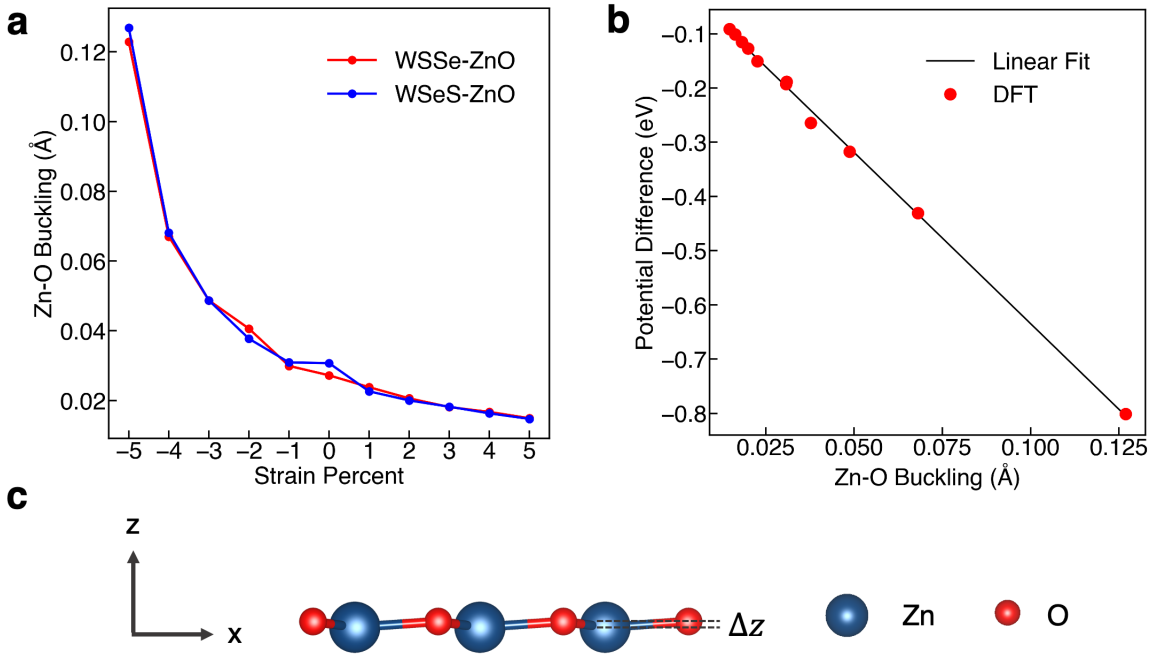


Figure 5.3: The effect of biaxial in-plane strain on the buckling in monolayer ZnO. (a) Magnitude of the buckling (Δz) in ZnO layer as a function of in-plane biaxial strain for the two heterostructures studied, calculated as the difference between the Cartesian z-position of the O ion and that of the Zn ion. (b) Magnitude of the electrostatic potential energy difference across a monolayer of ZnO for each buckling value and a linear fit (black line). (c) Schematic of the difference of the Cartesian z-positions of the O ion and the Zn ion, with Δz corresponding to the Zn-O buckling values.

the gap becoming indirect due to a reordering of the relative energies of the K and Λ valleys, where the Λ valley lies along the high symmetry line between the Γ and K valleys. In this case the K-K transition of WSSe increases in energy, consistent with the chalcogen p-orbital rationalization.

A trend emerges in the effect of biaxial strain on the relative alignment of the WSSe and ZnO band edges. Tensile biaxial strain tends to shift the ZnO bands to lower energy relative to those of WSSe whereas compressive biaxial strain tends to shift the ZnO bands to higher energy. Under compressive strain the WSSe band gap does not change and this shift is attributed to the change in the buckling of the ZnO layer under biaxial compressive strain (Figure 5.3). The out-of-plane dipole moment across the ZnO layer exhibits sensitivity to biaxial compressive strain as can be seen by the difference in the electrostatic potential on

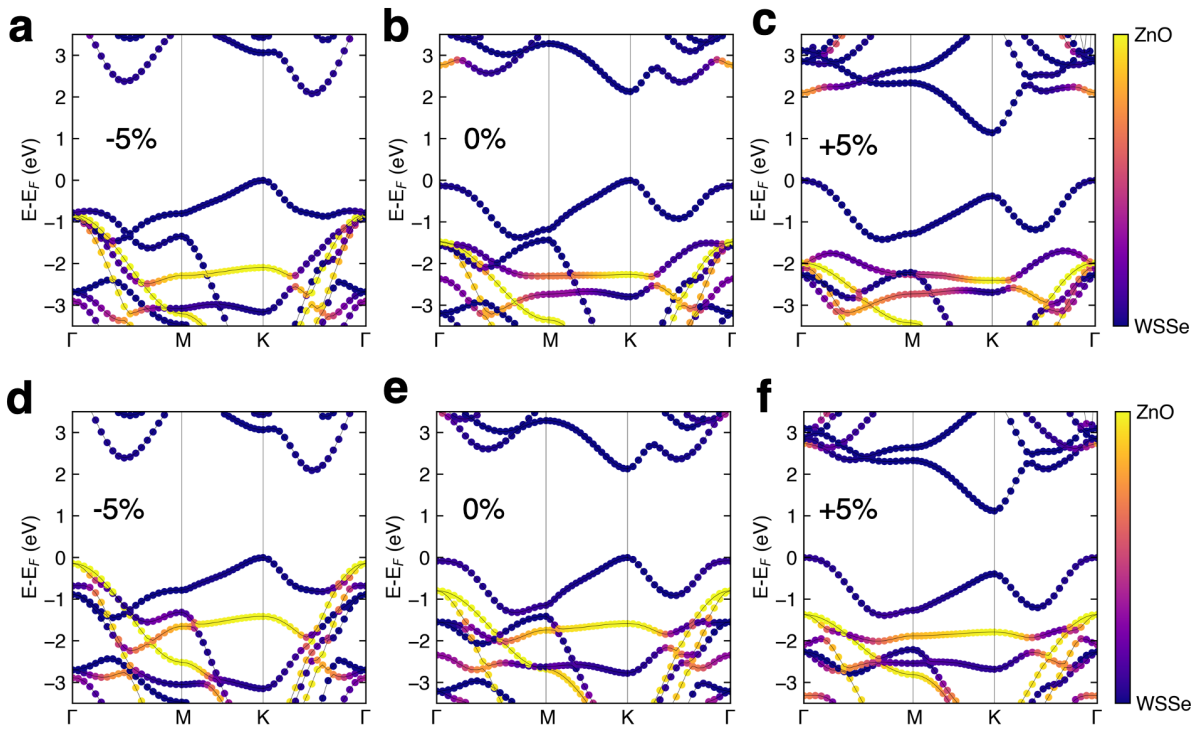


Figure 5.4: Band structures of the Janus TMD-ZnO heterostructures for WSSe-ZnO (a,b,c) and WSeS-ZnO (d,e,f) at 5% compressive strain (a,d), no strain (b,e), and 5% tensile strain (c,f). The orbital projections are color coded so that orbitals with more WSSe character are purple and those with more ZnO character are yellow, as indicated by the color bars.

either side of the ZnO monolayer in Figures 5.3b and 5.6a. Under tensile biaxial strain two concurrent effects occur. First, the buckling in the ZnO and the resulting magnitude of the dipole moment decreases (albeit to a much smaller degree) which is the opposite of the effect seen under compressive biaxial strain. Second, the band gap of WSSe decreases and (as seen in Figure 5.4c,f) the absolute positions of the VBM of WSSe are renormalized to slightly higher energies. Overall this manifests as a downward shift in the ZnO VBM energy relative to that of WSSe.

At 5% compressive biaxial strain the ZnO states at the Γ point shift up in energy sufficiently to make the WSeS-ZnO heterostructure a nearly Type II heterojunction (Figure 5.4d). As our HSE band gap for ZnO is known to be a significant underestimation and it is not known if the error is primarily in the VBM or CBM position (or both), we cannot conclude that 5% compressive biaxial strain is sufficient to drive a transition to a Type II

heterojunction. However, we can conclude that under some sufficient, but unknown, amount of compressive biaxial strain, a Type II heterojunction could be realized, assuming that the strain were not so large as to destabilize the heterostructure.

The calculated band edges for each structure are reported in Figure 5.5, in addition to the calculated band edges for monolayer WSSe for comparison. Due to the out-of-plane dipole moment of WSSe the band edge energies are different on opposing sides of the monolayer WSSe and the heterostructures, with the Se side having a smaller work function than the S side. The work functions on either side of the heterostructures are reported separately. Both sides of monolayer WSSe behave similarly under application of biaxial strain (Figure 5.5a,b). The VBM increases in energy slightly and the CBM decreases in energy significantly with the application of tensile biaxial strain due to the reduction of the band gap, as has been observed in TMDs under tensile biaxial strain experimentally [50]. In the picture described above, in which bonding-antibonding behavior of the chalcogen p-orbitals plays a role in modulating the K-K transition as a function of separation between p-orbitals, it is reasonable that the CBM at K is more strongly affected by tensile strain because the p-orbitals are the only in-plane orbitals (the W orbitals are out-of-plane d_{z^2} orbitals). In the VBM at K however the in-plane character of the W orbitals, which are midway between the chalcogen orbitals, helps mitigate the magnitude of this effect by providing a means by which in-plane orbital hybridization may still occur. This behavior is reproduced in the Janus TMD-ZnO heterostructures on the WSSe sides of the heterostructures (Figure 5.5e,h). However, on the ZnO side of the heterostructures the VBM is strongly affected by compressive biaxial strain and decreases dramatically. As the band gap does not change significantly, the CBM decreases in energy correspondingly (Fig 5.5d,g). This behavior differs substantially from that of monolayer WSSe and warrants further investigation, as compressive biaxial strain is the only case in which the presence of the ZnO appears to modify the band edge energies of WSSe in the Janus TMD-ZnO heterostructures.

As mentioned, Janus TMDs exhibit an out-of-plane dipole moment due to the differing chalcogen ions on either side. This produces a potential energy difference of 0.71 eV across the monolayer WSSe in our calculations. In the absence of ZnO, the potential energy difference across the WSSe exhibits minimal variation with compressive and tensile biaxial strain (Figure 5.6a). Due to the small amount of buckling, monolayer ZnO also experiences a smaller out-of-plane potential energy difference, 0.19 eV in the unstrained structure. Unlike monolayer WSSe, the magnitude of the potential energy difference of monolayer ZnO is sensitive to compressive biaxial strain and increases dramatically with increasing compressive biaxial strain, up to 0.8 eV at 5% compressive biaxial strain (Figures 5.3b and 5.6a) .

In all of the heterostructures studied, the buckling in the ZnO layer has the same directionality, with O shifted slightly higher and further away from the TMD than Zn, irrespective of biaxial strain percent. However, the directionality of the potential energy difference in the WSSe layer is reversed depending on which chalcogen faces the ZnO layer. The electrostatic potential of the S side of WSSe is always at lower (more negative) energy than the Se side. The direction of the electrostatic potential energy difference, meaning whether the top or bottom is at higher potential energy, is the same for ZnO and WSSe in the WSeS-ZnO

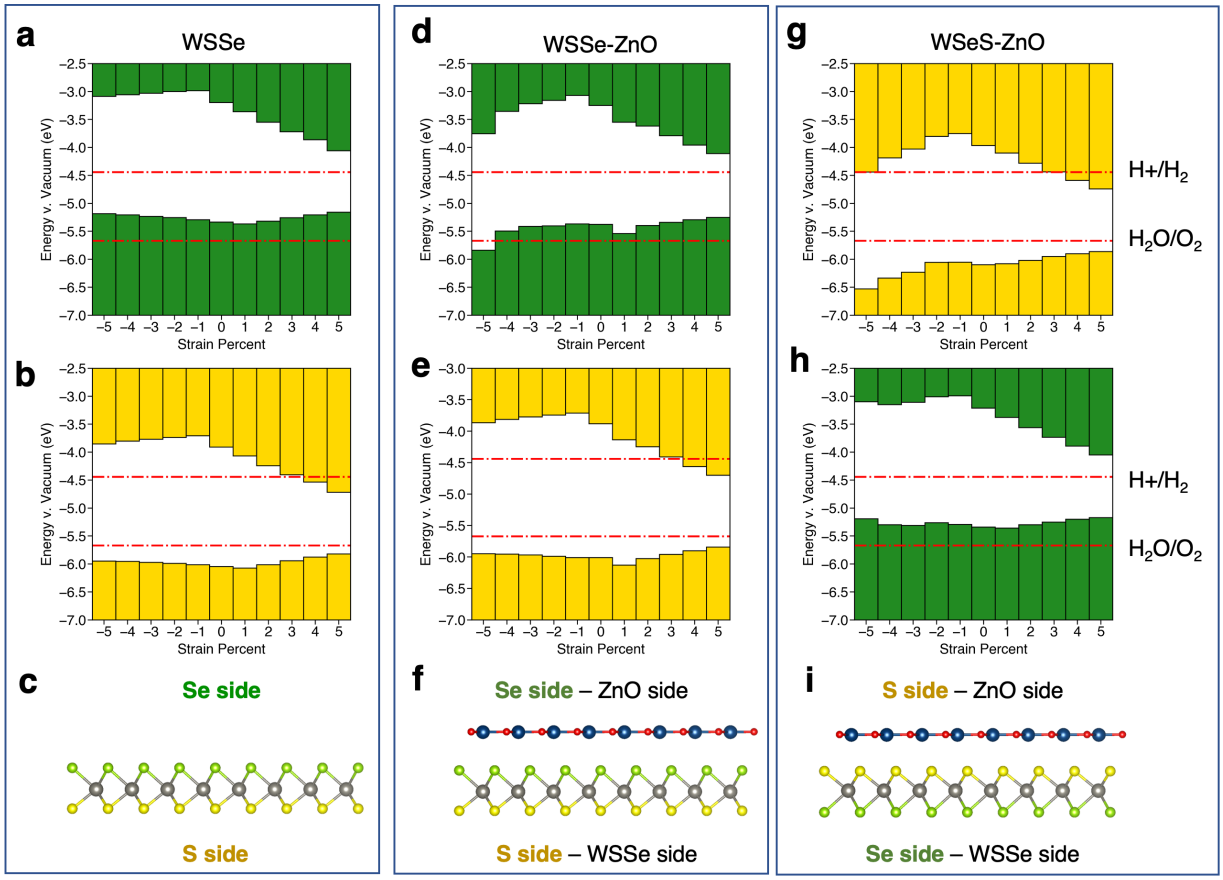


Figure 5.5: Schematics of band edge alignments under in-plane biaxial strain. Band edge alignment of monolayer WSSe on the (a) Se side and (b) the S side. Band edge alignment of WSSe-ZnO on the (d) Se/ZnO side and (e) S/WSSe side. Band edge alignment of WSeS-ZnO on the (g) S/ZnO side and (h) Se/WSSe side. Schematics of (c) monolayer WSSe, (f) WSSe-ZnO and (i) WSeS-ZnO with labels indicating what Se side, S side, ZnO side and WSSe side refer to. Green or yellow bars indicate that the band edges are calculated from the electrostatic potential relative to the vacuum level on the Se side or S side of WSSe respectively. The redox potentials for the hydrogen evolution reaction and the oxygen evolution reaction at pH=0 are indicated in red lines. The potentials for pH=7 and pH=14 are shown in Appendix III Figure 5.12.

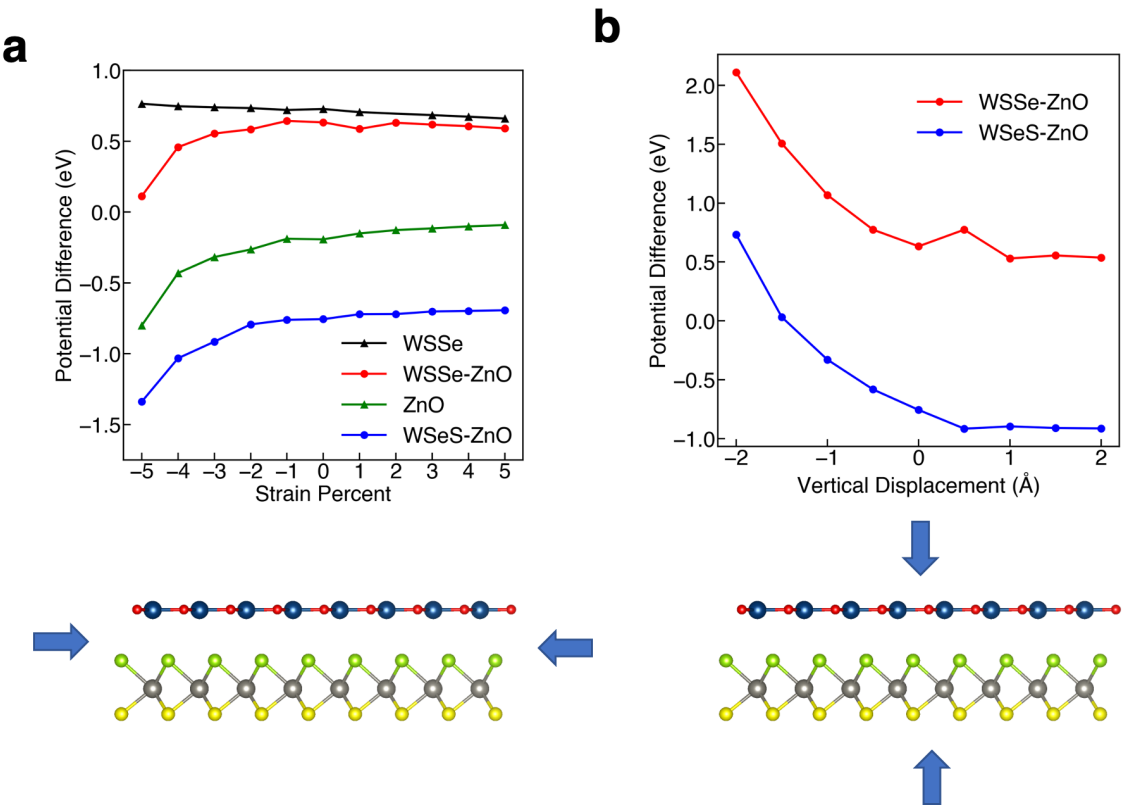


Figure 5.6: Electrostatic potential differences across WSSe, ZnO, and the heterostructures under study. (a) The electrostatic potential difference between the ZnO (or top) side and WSSe (or bottom) side of monolayer WSSe, monolayer ZnO, and the two most stable stacking configurations WSSe-ZnO and WSeS-ZnO. Compressive strain tends to make the electrostatic potential difference more negative. (b) The electrostatic potential difference between the ZnO side and WSSe side of the two most stable stacking configurations as a function of displacement of the ZnO from the equilibrium separation. Vertical compression tends to make the electrostatic potential difference more positive.

configuration, but is opposite in the WSSe-ZnO configuration. In this discussion top and bottom are referenced to the directionality displayed in Figure 5.1a where ZnO is on top of the Janus TMD. As compressive biaxial strain is applied, the electrostatic potential difference between the ZnO side and WSSe side of both WSSe-ZnO and WSeS-ZnO becomes more negative, mimicking the trend for the electrostatic potential difference of the ZnO (Figure 5.6a). If the ZnO monolayer were inverted, with O in closer proximity to the WSSe and the dipole moment of the ZnO reversed, we expect that the opposite effect would occur, with the potential difference across the ZnO becoming more positive and the bands of the heterostructures shifting to higher energies under compressive in-plane biaxial strain.

Further insight can be gained by considering the effects of vertical proximity via out-of-plane uniaxial strain. From Table 5.3, compressive biaxial strain moves the ZnO layer further away from the WSSe and tensile biaxial strain moves the ZnO layer closer. To investigate the effects of out-of-plane uniaxial strain, band edge calculations are performed on the unstrained structures with the ZnO layer moved closer and farther away from the WSSe. The effect of vertical displacement on the band edge positions, defined as the deviation of the interlayer spacing from the equilibrium distance of each structure, is displayed in Figure 5.7. The electrostatic potential energy of the WSSe side is not affected by the changing vertical proximity. However, the electrostatic potential on the ZnO side of the heterostructure is strongly affected by decreasing interlayer separation. The electrostatic potential energy difference between the ZnO side and the WSSe side of each heterostructure becomes more positive with decreasing interlayer separation (Figure 5.6b). Further, as the vertical separation decreases, the VB edges of the Janus TMD-ZnO heterostructures on the ZnO side of the heterostructure shift to higher energies, the opposite of the effect exhibited under in-plane biaxial compression.

A significant energetic barrier exists for large amounts of vertical compression (Appendix II: Fig 5.11c), however even with small amounts of vertical compression a substantial change in the band edge energies can be observed. For example, in the WSeS-ZnO heterostructure a decrease in the vertical separation of 0.5 Å can generate a 177 meV shift in the valence band edge with an energy cost of 23 meV/atom, on the order of kT, the amount of thermal energy expected at room temperature.

This work demonstrates that the band edge energies of the Janus TMD-ZnO heterostructure can be tuned, shifted to lower energies with compressive in-plane biaxial strain or shifted to higher energies with compressive out-of-plane uniaxial strain. What is particularly interesting about this effect is that the ZnO plays a large role in determining the band edge energies of these heterostructures despite the fact that, in our calculations, its band edges straddle those of WSSe and do not make large orbital contribution to the heterostructures' VB and CB edges. The interplay between the dipole moment of ZnO and that of WSSe is critical in producing this phenomenon as it does not occur in monolayer WSSe alone, as demonstrated by the lack of change in the electrostatic potential energy difference across WSSe (Figure 5.6a) and the lack of a downward shift in the VBM position under compressive in-plane biaxial strain (Figure 5.5a,b) for isolated monolayer WSSe. A similar effect has been observed in multilayer MoSSe, with the dipole moments of successive layers inducing

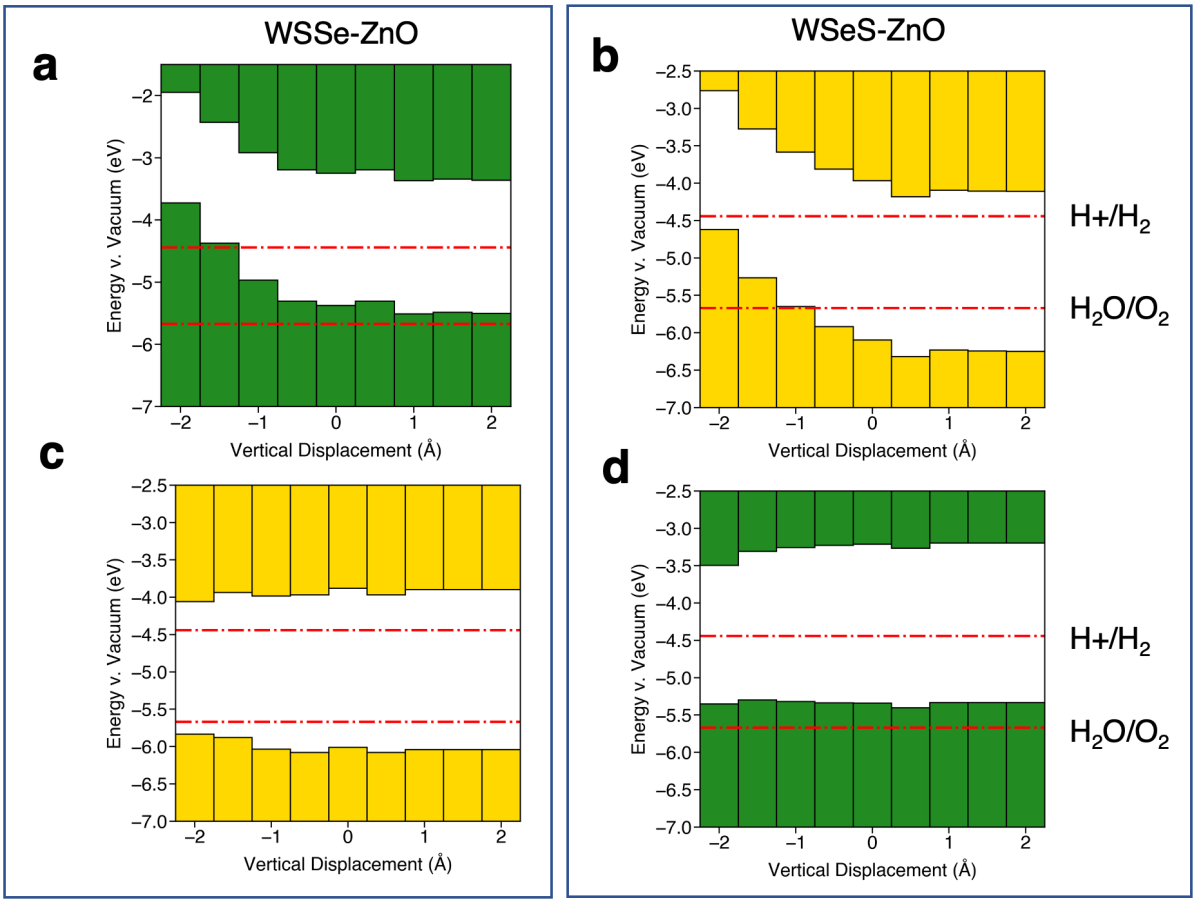


Figure 5.7: Summaries of band edge alignments under out-of-plane uniaxial strain. Band edge alignment of the most stable stacking configurations on the ZnO side of the heterostructure (a,b) and the WSSe side of the heterostructure (c,d) for (a,c) WSSe-ZnO and (b,d) WSeS-ZnO as a function of the vertical displacement of the ZnO relative to the equilibrium separation of ZnO and WSSe in each heterostructure. ZnO side and WSSe side are defined as in Figure 5.5f,i. Green or yellow bars indicate that the band edges are calculated from the electrostatic potential relative to the vacuum level on the Se side or S side of WSSe respectively. The redox potentials for the hydrogen evolution reaction and the oxygen evolution reaction at pH=0 are indicated in red lines. The potentials for pH=7 and pH=14 are shown in Appendix III Figure 5.13.

shifts in the band edges on either side of the multilayer structure [14], indicating that band edge tuning of vdW heterostructures with dipole moments in each layer is a broader field of study that is ripe for exploration.

For completeness, we calculate the phonon band structures of the Janus TMD-ZnO heterostructures under compressive in-plane biaxial and compressive out-of-plane uniaxial strain. Under compressive in-plane biaxial strain the heterostructures begin to exhibit imaginary frequency phonon modes indicating dynamical instability (Appendix II: Figure 5.9). The imaginary phonon modes are confined to the ZnO layer indicating that ZnO may undergo a phase transition upon application of compressive in-plane biaxial strain. While prior first-principles work studying ZnO under biaxial strain has been performed and the tunability of the electronic structure under these conditions has been reported [110, 111], it appears that the dynamical and phase stability of this material under biaxial strain have not yet been studied in detail. The phonon modes at imaginary frequencies are localized in the ZnO layer and the eigenvectors correspond to alternating out-of-plane displacements, suggesting that a phase transition would likely occur to a buckled structure with periodic oscillations of the directionality of the buckling and dipole moments. This would likely diminish the magnitude of the band edge tuning effect. Encouragingly though, small amounts of compressive out-of-plane uniaxial strain, such as the likely energetically-achievable decrease in vertical separation of 0.5 Å, do not produce imaginary phonon frequencies, although large amounts of compression do (Appendix II: Figure 5.10). Despite the dynamical instability of ZnO under compressive in-plane biaxial strain, we continue the discussion of the properties of these heterostructures under varying degrees and types of strain as our results should be generalizable to heterostructures of Janus TMDs and other 2D materials that have small out-of-plane dipole moments and hence still of value in a broader discussion of engineering novel vdW heterostructures for photocatalytic applications.

5.5 Electric Field

Application of an out-of-plane electric field, for example via an underlying gate or in a sandwich geometry via electrodes, is another method for tuning electronic structure. In prior first-principles work it has been shown that an out-of-plane electric field does not substantially affect the band gap of monolayer Janus TMDs [100]. Past work on the effect of out-of-plane electric fields on TMD homobilayers however suggests that application of an electric field can substantially change the band gap, producing a transition to a metallic state near 0.5-1.0 eV/Å [118]. As the heterostructures under study in this work are heterobilayers, we perform band structure calculations to determine whether an out-of-plane electric field will affect the Janus TMD-ZnO heterostructures as though they were Janus TMD monolayers or as though they were TMD homobilayers.

We calculate the HSE band structures of our two stacking configurations under the application of out-of-plane electric fields of varying strengths. We find that application of an out-of-plane electric field does not change the band gap of these heterostructures by

more than 0.01 eV, both at moderate and very large electric force field strengths up to 1 eV/Å (Appendix IV: Table 5.4). This is reasonable given that the valence and conduction band edges are dominated by WSSe states, with the ZnO valence and conduction band edges straddling those of WSSe. Effectively, the band edges of the Janus TMD-ZnO heterostructure behave as though the system were a Janus TMD monolayer in the presence of an out-of-plane electric field. The relative alignment of the WSSe and ZnO bands reorders somewhat, but not to a sufficient degree to produce a Type II heterojunction.

With respect to the absolute band edge energies of the Janus TMD-ZnO heterostructures, calculation of the absolute VBM position via the electrostatic potential is challenged by the fact that the electrostatic potential in the vacuum region is not constant in the presence of an electric field and there is no well-defined vacuum energy. However, in prior work it has been shown that monolayer TMDs stacked on ferroelectric materials experience shifts in their work function as a result of proximity to an out-of-plane electric polarization [119]. For example, monolayer MoS_2 stacked on $BiFeO_3$ with an out-of-plane polarization experiences rigid shifts in its band edges, which can be patterned to produce p-n junctions between regions of ferroelectric domains with opposite polarization [99]. This indicates that it may be possible to tune the band edges of the Janus TMD-ZnO heterostructures rigidly with an out-of-plane electric field, or a substrate with a finite out-of-plane electric polarization.

5.6 Photocatalytic Applications

For photocatalytic applications the absolute positions of the band edges relative to the redox potentials of the water splitting reaction or CO_2RR are critical. In much of the past experimental work considering TMD photocatalysts attention has been paid primarily to using TMDs as cathodes for the relevant reduction reactions (HER and CO_2RR) [90–92] rather than acting as a catalyst for the entire water splitting reaction, donating both holes and electrons for OER and HER. Leveraging control over the CB energies has been studied as a means of attempting to tune product selectivity amongst the various competing CO_2RR products and HER [89]. Nonetheless, it is still informative to consider the band edges of the Janus TMD-ZnO heterostructures relative to both the OER and HER (knowing that the CO_2RR potentials are in the neighborhood of the HER potential as discussed in Chapter 4).

The redox potentials for the hydrogen evolution reaction (HER) and oxygen evolution reaction (OER) at pH=0 are plotted on the band edge plots in Figure 5.5 and Figure 5.7. It is important to note that under operating conditions in aqueous environment the relative positions of the HER and OER redox potentials to the band edges of the heterostructures will differ from the relative positions of the pH=0 redox potentials to those of the vacuum band edges of the heterostructures. First, the dipole moments of the water molecules on the surface of the heterostructure will alter the relative alignment. Second, the HER and OER redox potentials are functions of pH and shift according to the Nernst equation (Eq. 5.2) [120] as pH is increased to more realistic operating conditions, that is

$$E(pH) = E(pH = 0) + 0.0591 * pH. \tag{5.2}$$

The calculated vacuum band edge positions correspond to the point of zero charge (PZC), the pH value at which the surface of the catalyst has equal concentrations of positive and negative ions under aqueous conditions [66]. The PZC is generally determined empirically and, as it is unknown for these heterostructures, it is difficult to interpret which pH the calculated vacuum band edges of these heterostructures correspond to. However, higher band edge positions are likely to be necessary under realistic photocatalytic conditions as pH=0 is unlikely to be the PZC. With these caveats, we compare the calculated band edges to those of the HER and OER at various pH values. Consideration of the effect of surface dipoles from water molecules is beyond the scope of this work.

Another consideration is Pourbaix stability, or the stability of a material under aqueous conditions and applied bias. Using the Materials Project Pourbaix Diagram software [83, 121–123], the most energetically stable species (including both solids and ions) for a given elemental composition at a particular pH and applied potential can be determined, as well as the energy above hull for unstable species. Neither WSSe nor monolayer ZnO are the most stable species at any pH or applied potential. For example, at pH = 7 and no bias voltage relative to the reversible hydrogen electrode (RHE), the potential corresponding to HER, WSSe is 0.10 eV/atom above the Pourbaix hull and monolayer ZnO is 0.39 eV/atom above the Pourbaix hull. At a bias voltage of -0.5 V vs. RHE, a representative value considered in prior work to correspond to reducing conditions for CO_2RR [97], the energies above hull are 0.29 eV/atom and 0.39 eV/atom respectively. Past work comparing the calculated energy above the Pourbaix hull for a number of known oxide photoanode materials, however, found that many of them exhibited a nonzero energy above hull, up to 0.5 eV/atom [122]. The experimentally observed stability of these materials was attributed to kinetic barriers to undergoing a phase transition to the more stable phase. While this does not guarantee that the Janus TMD-ZnO heterostructures studied here will also exhibit this meta-stability, it indicates that it is possible that they could exhibit reasonable operational stability. Alternatively, addition of an encapsulating protective coating of a Pourbaix stable 2D material or thin film could be employed to protect the heterostructures.

The relative alignment of the band edges of the heterostructures to the HER and OER potentials at pH=0, 7, and 14 are plotted in Appendix III in Figures 5.12 and 5.13. In general, due to the electrostatic potential energy difference between the Se and S sides of WSSe, the band edges on the side of the heterostructure that the Se faces will always be at higher energy. The VBM is generally $\sim$0.7 eV higher in energy on the Se side (Figure 5.5d,h and Figure 5.6a,d). The HER and OER redox potentials increase in energy by $\sim$0.4 eV at pH=7 according to the Nernst equation, in which case the Se sides of the heterostructures are more likely to straddle the band edges. Thus, the large dipole moment across the Janus TMD-ZnO heterostructures allows for the band edges to straddle the HER and OER potential at the redox potentials corresponding to a variety of pHs by varying which side of the heterostructure is used as the catalytic surface (i.e. the side of the heterostructure

from which photoexcited carriers would be donated to catalyze chemical reactions) and the amount of strain applied.

Relative to the redox potentials under extreme acidic conditions (pH=0) the WSSe side of the WSSe-ZnO heterostructure is terminated by S ions making that side optimal for a catalytic surface (Figure 5.5e) Alternatively, using the ZnO as the catalytic surface, the S side of WSeS-ZnO under no strain (Figure 5.5g) or the Se side of WSSe-ZnO with the application of compressive biaxial strain (Figure 5.5d) would be appropriate. Relative to the redox potentials under neutral conditions (pH=7), both the S terminated side of WSSe-ZnO (Figure 5.5e) and the Se terminated side of WSeS-ZnO (Figure 5.5h) could have appropriate band edge positions. Relative to the redox potentials under extreme basic conditions (pH=14) the WSSe side of the WSeS-ZnO heterostructure is terminated by Se ions making the band edges of that side of this stacking configuration likely the best candidate for a photocatalytic surface (Figure 5.5h). Using ZnO as the catalytically active surface, the Se side of WSSe-ZnO under no strain (Figure 5.5d) or the ZnO sides of WSeS-ZnO and WSSe-ZnO under the application of compressive out-of-plane uniaxial strain (Figure 5.7a,b) could be suitable. As we expect the PZC of these heterostructures to be at pHs higher than pH=0, it is encouraging that the dynamically unstable heterostructures under compressive biaxial strain are perhaps not the most relevant for photocatalytic applications. The heterostructures that best straddle the pH=7 and pH=14 redox potentials exhibit dynamical stability, with no imaginary phonon modes.

In the cases in which the ZnO side of the heterostructure is used as the catalytic surface, carriers would need to tunnel through to the ZnO layer since the VBM and CBM are dominated by WSSe orbitals (Figure 5.4) and excited carriers would be expected to reside in the WSSe layer. In WSSe-ZnO under zero or tensile biaxial strain our HSE band structure calculations indicate that the CB is characterized by hybridization of WSSe and ZnO states at the Γ point that are nearly degenerate with the CBM at the K point enhancing the probability for electron tunneling to the ZnO layer. Similarly, for the WSeS-ZnO heterostructure, under biaxial compressive strain our HSE band structure calculations indicate that the VB is characterized by ZnO states at the Γ point that are nearly degenerate with the VBM at K making it favorable for holes to tunnel to the ZnO layer. Preventing charge recombination is critical to efficient photocatalysis so if this tunneling or hopping could be achieved the photocatalytic efficiency of these heterostructures would be significantly enhanced.

5.7 Outlook

DFT calculations on Janus WSSe-ZnO heterostructures are performed to study the effects of in-plane biaxial strain, out-of-plane uniaxial strain, and electric field on the electronic structure of these heterostructures, with the aim of exploring the tunability of their electronic properties for photocatalytic applications. The unstrained heterostructures exhibit a Type I band alignment with the ZnO VBM and CBM straddling the WSSe VBM and CBM.

The absolute band edges of the heterostructures are at higher energy on whichever side

of the heterostructure the Se side of WSSe faces due to the finite dipole moment across the WSSe. In general, if the PZC of these heterostructures corresponded to acidic conditions, the S side of these heterostructures would be preferable for straddling the HER and OER potentials. With a neutral PZC either side has band edge energies that are appropriate. For a basic PZC, the Se side of these heterostructures is generally preferable. Tensile in-plane biaxial strain tends to decrease the band gap of the heterostructures, shifting the CBM down to unfavorably low values for HER catalysis.

Compressive in-plane biaxial strain does not significantly change the band gaps of the heterostructures and does not change the band edge energy on the WSSe side of the heterostructure. However, compressive in-plane biaxial strain generates an interfacial dipole effect by amplifying the magnitude of the dipole moment in ZnO that strongly affects the band edges on the ZnO side of the heterostructures. This results in a reduction of the VBM position on the ZnO side. Conversely, reducing the interlayer distance via out-of-plane uniaxial compressive strain generates an interfacial dipole effect that shifts the band edges on the ZnO side of the heterostructure to higher energies, more favorable for catalysis relative to the non-acidic redox potentials for HER and OER. These results demonstrate the significance of the ZnO in these heterostructures as a means of tuning the absolute band edges of the heterostructures either up or down via out-of-plane uniaxial compressive strain or in-plane biaxial compressive strain, respectively.

The effect of an out-of-plane electric field is investigated to determine if this could modify the band structure by potentially modifying the interfacial dipole effects. Our calculations show that out-of-plane electric fields do not significantly affect the band gaps of Janus WSSe-ZnO heterostructures, indicating that the band edges could potentially be rigidly shifted up and down in the presence of an applied electric field or substrate with a finite out-of-plane electric polarization, as has been observed for TMDs in prior experiments.

Our investigation of Janus WSSe-ZnO heterostructures demonstrates that the band gaps and absolute band edge energies of vdW heterostructures of 2D materials with finite dipole moments can be tuned by the application of strain when the magnitude of the dipole moment of one of the layers is correspondingly tuned by strain. The significance of this result is that a single heterostructure, with a clean vdW interface, could be synthesized and mechanically manipulated to tune its band edges. This differs from prior studies of band edge tuning via changing the elemental composition or constructing interfaces with or passivating surfaces of bulk materials, that suffer from less controllable effects like surface or interfacial reconstruction. This effect should be generalizable to other vdW heterostructures and could potentially be harnessed for the development of novel photocatalysts with tunable band edge energies.

5.8 Appendix I: Comparison of band structures at PBE and HSE levels of theory

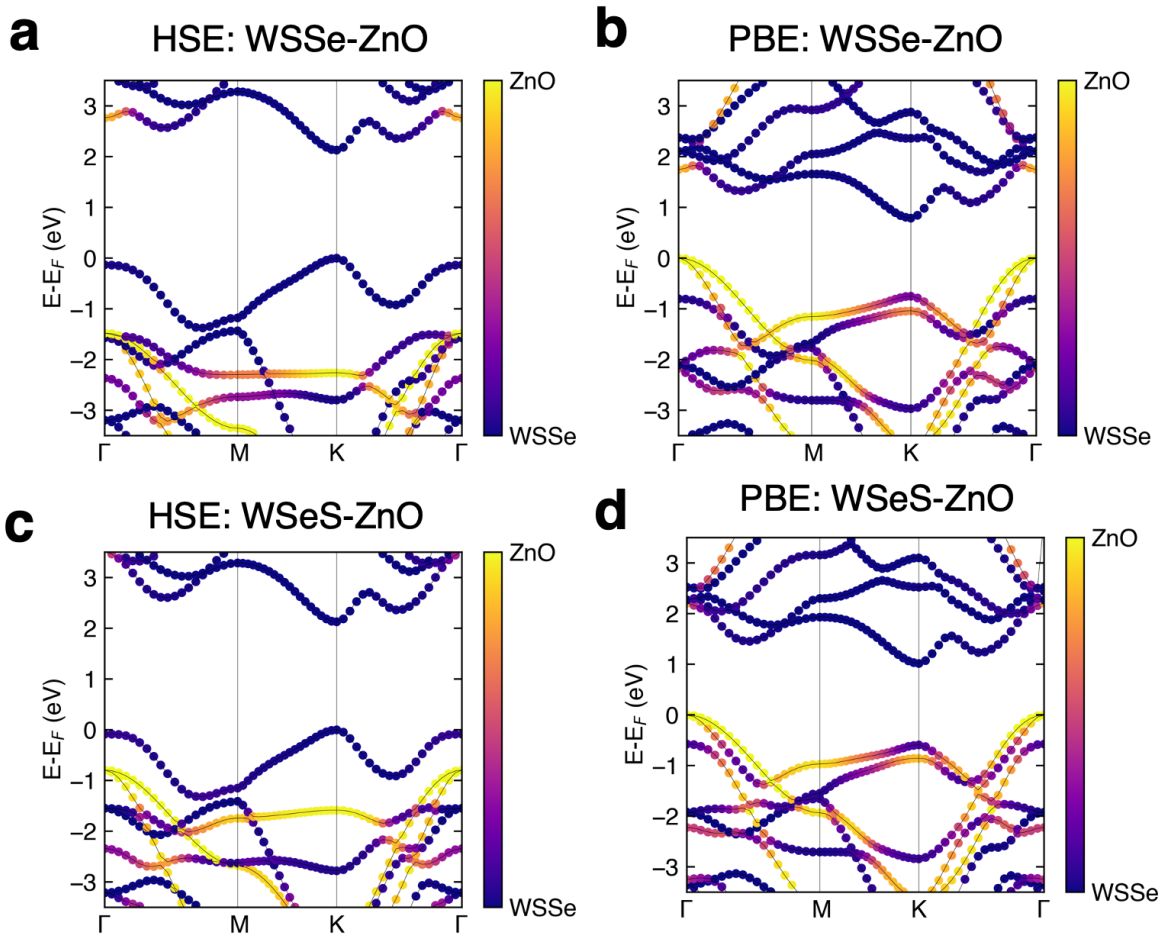


Figure 5.8: Band structures with orbital projections of WSSe and ZnO for WSSe-ZnO calculated via (a) HSE and (b) PBE. Similarly, band structures of WSeS-ZnO calculated via (c) HSE and (d) PBE. In both cases, the HSE band structures exhibit Type I band alignment and the PBE band structures exhibit Type II band alignment.

5.9 Appendix II: Phonon band structures and energetics of strained heterostructures

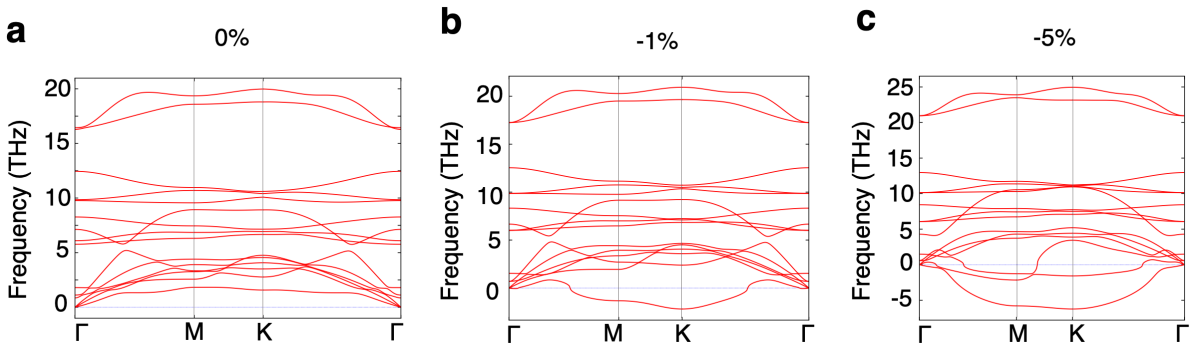


Figure 5.9: Phonon band structures of the WSeS-ZnO heterostructure under (a) 0% (b) 1% and (c) 5% in-plane biaxial compressive strain. The structures under biaxial compressive strain exhibit phonon modes with imaginary frequencies indicating a lack of dynamical stability. The imaginary modes are primarily confined to the ZnO layer, indicating that while WSSe is stable under biaxial compressive strain, ZnO is not stable under biaxial compressive strain.

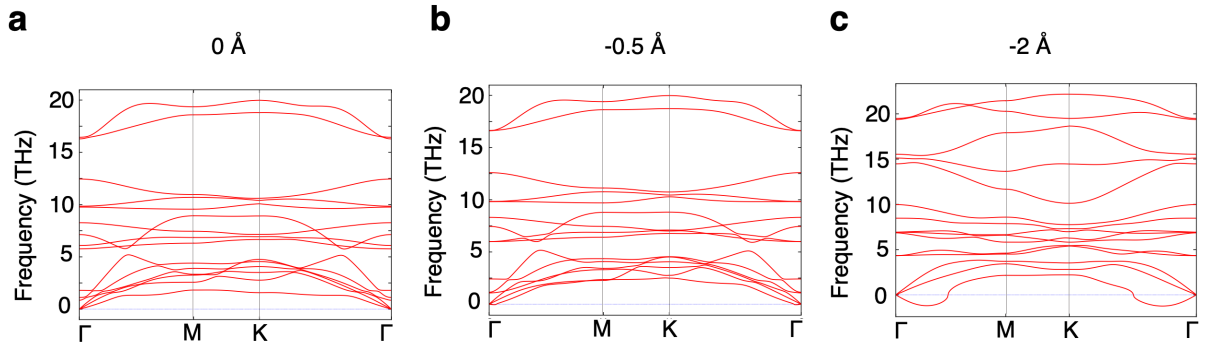


Figure 5.10: The phonon band structures of the WSeS-ZnO heterostructure under out-of-plane uniaxial compressive strain at (a) the equilibrium vertical separation (b) 0.5 Å of vertical compression and (c) 2 Å of vertical compression. For small amounts of vertical compression the heterostructure exhibits dynamical stability, however at larger amounts of vertical compression the heterostructure becomes structurally unstable.

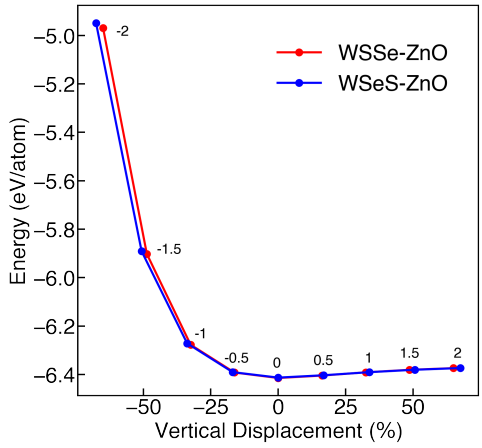


Figure 5.11: The energy per atom of Janus TMD-ZnO heterostructures as a function of vertical displacement, represented as a percent on the x axis with inset numerals indicating the number of Å by which the vertical separation differs from the equilibrium separation. There is a large energy barrier to vertical compression beyond 30% decrease in the vertical separation.

5.10 Appendix III: Band edge alignment to HER and OER redox potentials for varying pH

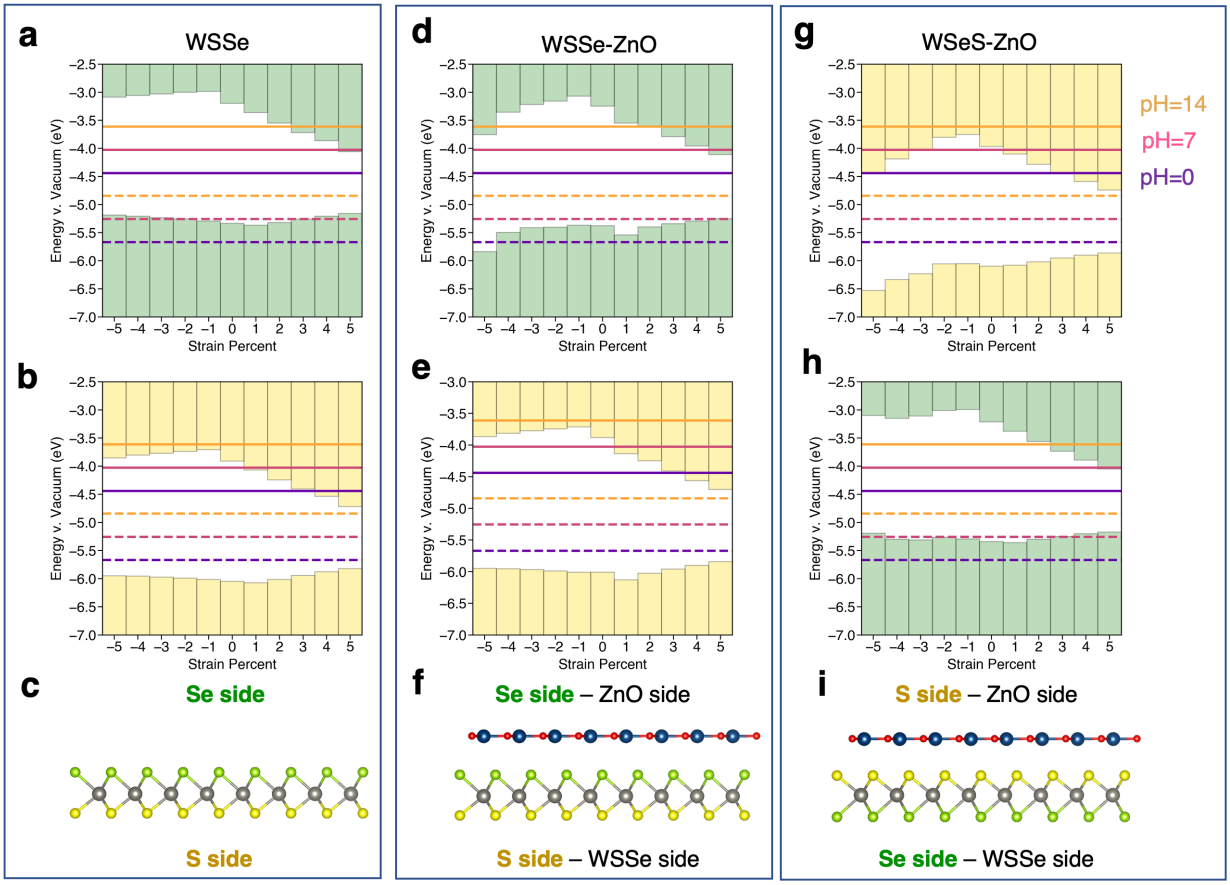


Figure 5.12: Reproduction of Figure 5.5. The redox potentials for the hydrogen evolution reaction and the oxygen evolution reaction at pH=0, 7, and 14 are indicated in purple, pink, and orange respectively with the hydrogen evolution potentials indicated by solid lines and the oxygen evolution potentials indicated by dashed lines.

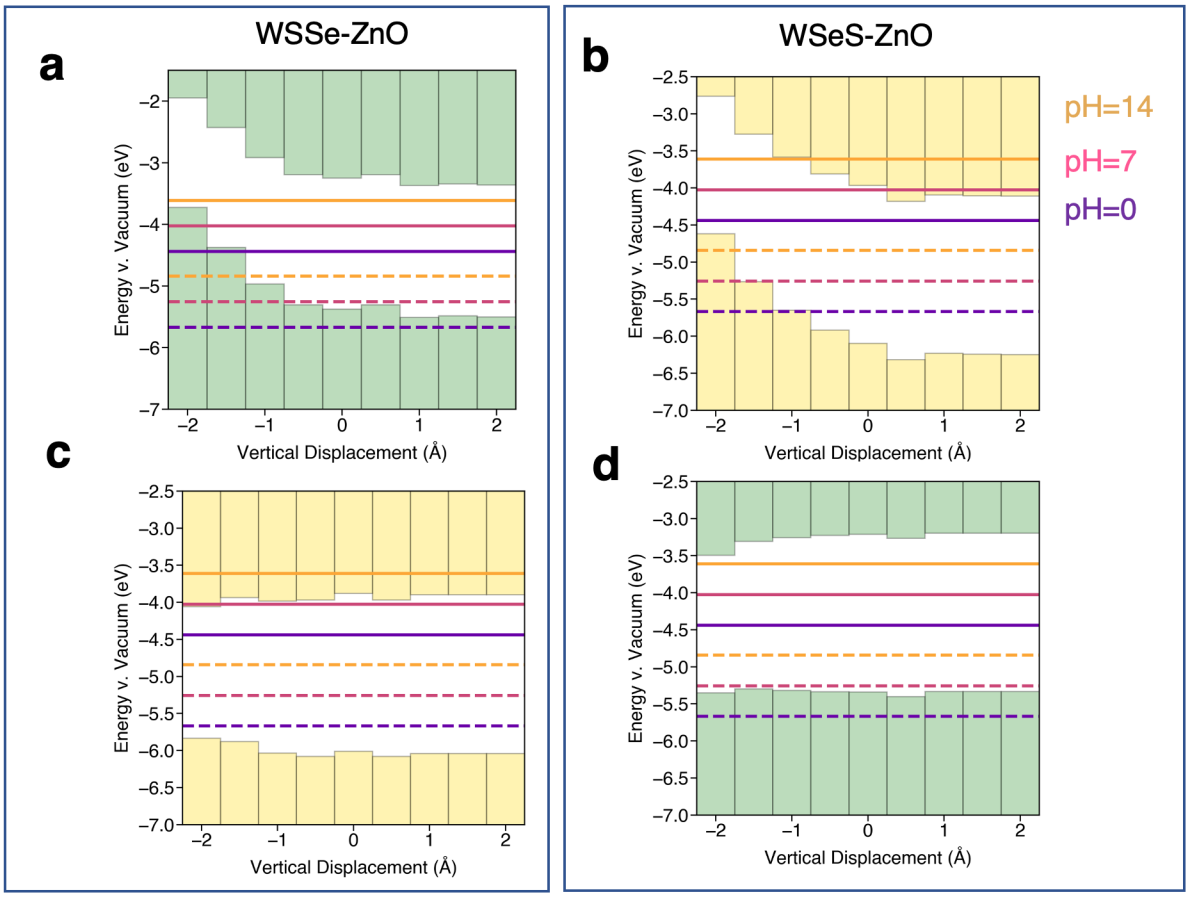


Figure 5.13: Reproduction of Figure 5.7. The redox potentials for the hydrogen evolution reaction and the oxygen evolution reaction at pH=0, 7, and 14 are indicated in purple, pink, and orange respectively with the hydrogen evolution potentials indicated by solid lines and the oxygen evolution potentials indicated by dashed lines.

5.11 Appendix IV: Band gaps of Janus TMD-ZnO heterostructures with an applied out-of-plane electric field

Stacking Configuration	Electric Field (eV/Å)	HSE Band Gap (eV)
WSSe-ZnO	-1.0	2.13
WSSe-ZnO	-0.2	2.13
WSSe-ZnO	0.0	2.13
WSSe-ZnO	0.2	2.14
WSSe-ZnO	1.0	2.12
WSeS-ZnO	-1.0	2.13
WSeS-ZnO	-0.2	2.13
WSeS-ZnO	0.0	2.13
WSeS-ZnO	0.2	2.13
WSeS-ZnO	1.0	2.11

Table 5.4: The HSE band gaps for the WSSe-ZnO and WSeS-ZnO stacking configurations under application of an out-of-plane electric field. The band gaps do not change considerably.

Chapter 6

Superexchange-induced valley splitting in two-dimensional transition metal dichalcogenides

This chapter is primarily adapted from [124].

6.1 Introduction to Valley Splitting

Monolayer transition metal dichalcogenides (TMDs) with the 2H-MX_2 structure (M = Mo/W, X = S/Se/Te) (Figure 6.1a) have attracted attention for valleytronics applications in recent years due to their semiconducting behavior and the existence of spin-valley coupling in these systems [16]. Monolayer TMDs exhibit a direct band gap [9] located at K and K' in the 2D hexagonal Brillouin zone (Figure 6.1b,c) where the valence band maximum (VBM) and conduction band minimum (CBM) states are energetically degenerate but inequivalent. Loss of inversion symmetry and strong spin-orbit coupling (SOC), which leads to splitting of the valence and conduction bands at K and K', give rise to degenerate but inequivalent valleys, which are linked by time reversal symmetry (Figure 6.1c). The symmetry and strong SOC lead to substantial spin-valley coupling, and the bands at K and K' exhibit opposite spin character and can be selectively excited with left-handed or right-handed circularly polarized light, for K and K' respectively [16].

The energetic degeneracy of the K and K' valleys can be lifted by breaking time reversal symmetry, causing valley polarization, with the band gap isolated in one valley (Figure 6.1c); the valley splitting is defined as the difference between the dipole-allowed band gaps at K and K'. Valley splitting has been demonstrated experimentally for monolayer TMDs in the presence of external magnetic fields or when supported by magnetic substrates, where photoluminescence, optical absorption, and reflectance measurements with circularly polarized light confirm that the band gaps in each valley differ when time reversal symmetry is broken [17, 125–130]. Whereas static magnetic fields have been shown to produce relatively

modest valley splittings 0.1-0.22 meV/T [17, 125–127], magnetic substrates such as EuO, EuS, CrI_3, and ferromagnetic metals Ni/Co lead to valley splittings of 1-16 meV, at least an order of magnitude larger [128–131]. Despite a growing number of experimental reports, a detailed quantitative picture of the origin of the valley splitting associated with magnetic substrates is still lacking. Prior studies have modelled the effect of magnetic substrates using an effective Zeeman field, adding other perturbations to account for inconsistencies between a purely Zeeman-like effect and first-principles calculations [130–133]. Other studies have described the TMD-magnetic atom interaction as magnetic exchange coupling or referred to it as a proximity exchange effect without providing an orbital- or spin-based mechanistic understanding of its nature or magnitude [129, 132, 134, 135]. Ref. [136] qualitatively assesses the impact of Cr-W alignment in a WSe_2+CrI_3 heterostructure but does not offer a theoretical framework within which to interpret their results. A detailed framework for understanding and quantifying the magnetic exchange coupling generated by orbital hybridization effects and the magnetic moment of the magnetic atom in the substrate, and for suggesting alternative magnetic substrates that might enhance the valley splitting would clearly be of value for interpreting future studies and for applications.

In this work we perform a systematic study of valley splitting induced in TMDs by monolayers of suspended magnetic atoms using density functional theory (DFT) calculations. By varying the coverage, alignment, proximity, and magnetic moment of Fe, Co, and Zn atoms on WSe_2 and MoS_2 TMD monolayers, we quantify the importance of these factors to the magnitude of valley splitting, specifically tracking the effect on the top-most valence band eigenvalue splitting at K and K'. We use the results of our DFT calculations to validate a minimal model of valley splitting, fitting our DFT results to a second-order expression from a model Hamiltonian with spin-dependent exchange coupling. From our calculations and analysis, we provide general design principles toward optimal magnetic substrates for large valley splittings and future valleytronics interfaces. Finally, we calculate the valley splitting generated in WSe_2 by an idealized magnetic oxide substrate in order to set an upper bound on achievable valley splitting.

6.2 Electronic Structure Methods

First-principles calculations are performed using density functional theory (DFT) with a plane-wave basis and projector augmented wave (PAW) pseudopotentials [61] as implemented in the Vienna *ab initio* Simulation Package (VASP) [62, 63] . The electrons treated explicitly as valence electrons are $5s^25p^66s^25d^4$ for W, $4s^24p^4$ for Se, $4s^24p^65s^24d^4$ for Mo, $3s^23p^4$ for S, $3s^23p^64s^23d^6$ for Fe, $3s^23p^64s^23d^4$ for Cr, and $3s^23p^64s^23d^{10}$ for Zn. Monolayer WSe_2 and MoS_2 are relaxed using the generalized-gradient approximation (GGA) as implemented by Perdew, Burke, and Ernzerhof (PBE) [23]; van der Waals dispersion corrections are approximately included using the Grimme-D3 method [37]. The relaxed lattice parameters are 3.29 Å and 3.16 Å respectively, in excellent agreement with experimental values of 3.282 Å [137] and 3.15 Å [64]. For relaxations of monolayer TMDs, an energy cutoff of 1000 eV

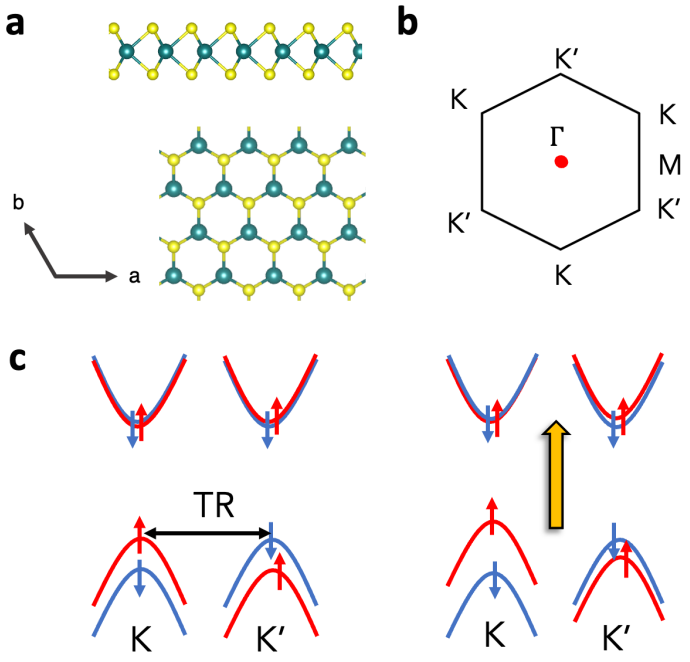


Figure 6.1: (a) Side and top view of a monolayer TMD crystal structure with the transition metal in turquoise and the chalcogen in yellow (b) Diagram of hexagonal 2D Brillouin zone (c) Spin-valley coupled valence and conduction bands at K and K' without (left) and with (right) time-reversal symmetry breaking because of a magnetic field (yellow arrow) or magnetic substrate.

is used with a 25x25x1 Γ-centered k-grid. Structures are relaxed until forces are less than 1 meV/Å.

TMD+Fe: Calculations for 100% coverage of Fe atoms are conducted using a 1000 eV energy cutoff and a 25x25x1 Γ-centered k-grid. Calculations for 33% coverage of Fe atoms are conducted using a 750 eV energy cutoff and a 15x15x1 Γ-centered k-grid. Non-collinear calculations with spin orbit coupling (SOC) are implemented self-consistently for structural relaxations and charge density generation for band structures. The magnetic moments of the magnetic atoms (Fe, Cr, Zn) are oriented in the positive z direction, unless specified otherwise. A vacuum layer $\geq$ 20 Å in the c-direction is used to prevent interactions between neighboring monolayers. To ensure that the valence band eigenvalues are not affected by spurious shifts in the Fermi energy, the electrostatic potential is calculated along the c-direction for each TMD+Fe system and the valence band eigenvalues are aligned to vacuum so they are all reported relative to the same absolute energy scale. Testing of the effect of an effective Hubbard U for Fe d states is performed using the PBE+U method of Dudarev [28].

WSe_2+(111)-$BiFeO_3$: The crystal structure of $BiFeO_3$ is relaxed in the bulk with an energy cut-off of 750 eV and a 5x5x2 Γ-centered k-grid until forces are < 1 meV/Å. A Hubbard U value of 4.0 eV is applied to the Fe ions to account for the expected localization of the 3d states. This yields an a-lattice parameter in the (111) planes of 5.62 Å, in good agreement with the experimental value of 5.58 Å [138]. A stoichiometric 4-layer slab of $BiFeO_3$ is constructed with a $\sqrt{3} \times \sqrt{3}$ supercell of WSe_2 placed on top and a vacuum layer above the TMD of ≥ 20 Å. A small amount of tensile strain is applied to the $BiFeO_3$ in order to make its in-plane lattice parameter match that of WSe_2. Dipole corrections are included in the calculations to account for the finite out-of-plane dipole moment of (111)-$BiFeO_3$. The magnetic moments of the $BiFeO_3$ Fe ions are oriented out-of-plane, with FM ordering in-plane and AFM ordering between alternating planes (unless otherwise specified). The band structures of this heterostructure at varying separations are calculated using a 750 eV energy cut-off with non-collinear magnetism and SOC included.

6.3 Model TMD+Fe Monolayer System Band Structure and Eigenvalues

We perform DFT calculations for monolayers of Fe atoms at a fixed height z above the surface of WSe_2 and MoS_2 (Figure 6.2d,e). While Fe atoms could be deposited on monolayer TMDs, we are unaware of any such experiments and we treat this as a model material system for purposes of understanding. We systematically compute the valley splitting as we vary the vertical height (or separation) and lateral alignment of the Fe atoms relative to the TMD substrate; we also consider two different Fe atom coverages. As we use periodic boundary conditions, the Fe atoms constitute a uniform monolayer for a fixed coverage in our calculations. The Fe monolayers are initially laterally aligned such that each of the Fe atoms lies directly above a metal site, either W or Mo in this case. Two coverages are considered: one Fe for 33% of the W or Mo atoms and one for 100%, respectively. Unless specified otherwise, the magnetic moment of the Fe atoms is aligned along the z direction in our calculations, normal to the TMD substrate.

Our calculations show Fe atom coverage-dependent valley splitting which is visible in the computed band structure of the TMD+Fe system (Figure 6.2b,c). Minimally-dispersive bands with Fe character appear in the band structure between the TMD valence and conduction bands in this model system, with limited hybridization with W orbitals and reduced dispersion with decreasing Fe coverage.

We identify and track the TMD valence and conduction bands via element-specific orbital projections in a manner we elaborate on below. As height z between the Fe monolayer and the TMD is reduced, the valley splitting systematically increases until at very close distances (small z), significant orbital hybridization dramatically alters the orbital character of the valleys at K and K', eliminating their desirable symmetry properties (valley degree of freedom and selection rules). We track the shift in the valence band (VB) energies of

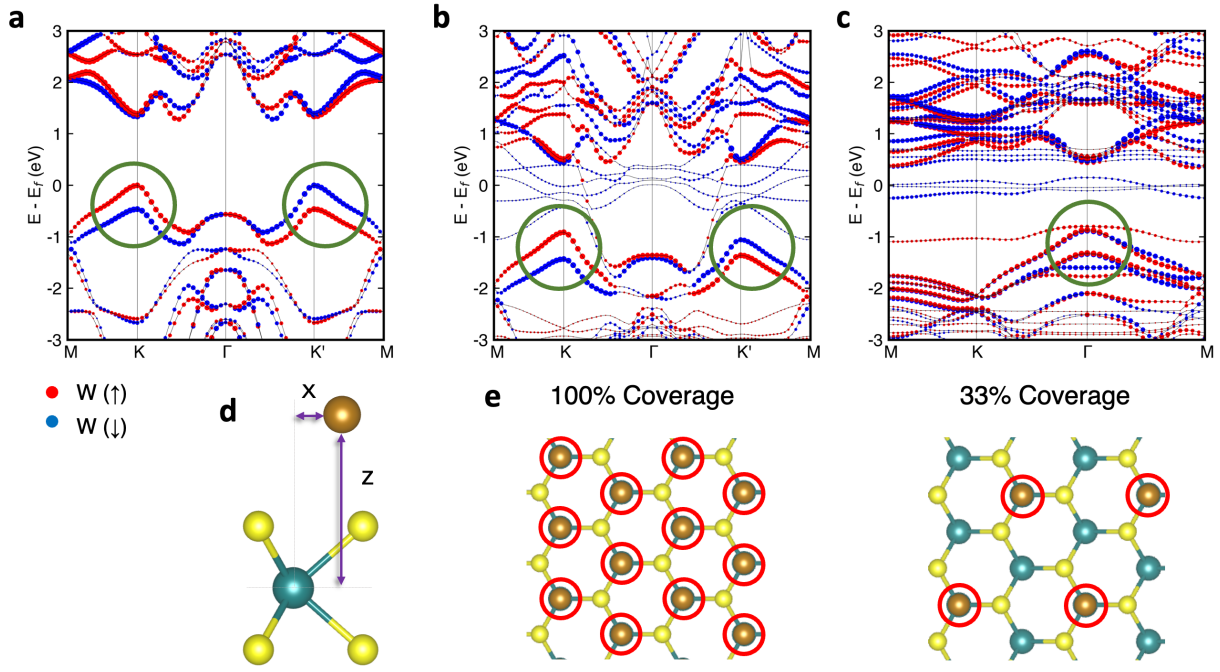


Figure 6.2: (a) The band structure of pristine WSe_2 with the spin character of W in each state indicated in red and blue for positive and negative respectively (b) The band structure of WSe_2 with 100% coverage of Fe atoms that are 4.4 Å above the W atom, with valley splitting clearly visible. (c) The band structure of WSe_2 with 33% coverage of Fe atoms that are 4.4 Å above the W atom, with K and K' folded into Γ (d) Schematic of Fe atoms above TMD monolayer indicating x and z displacements (e) Schematic of Fe atoms above TMD monolayer at 100% coverage (left) and 33% coverage (right).

the TMD, reporting our calculated values in Figure 6.5 for both 100% coverage (1 Fe per TMD primitive cell) and 33% coverage (1 Fe per $\sqrt{3} \times \sqrt{3}$ TMD supercell, see Figure 6.2e). Notably, the (111) planes of many perovskite-based oxides have similar lattice parameters to $\sqrt{3} \times \sqrt{3}$ supercells of S and Se TMDs. For example, the hexagonal (111)-plane of $BiFeO_3$ contains a single Fe atom with an in-plane lattice parameter of 5.58 Å [138], only 2% different from 5.70 Å, the in-plane lattice parameter of a $\sqrt{3} \times \sqrt{3}$ supercell of WSe_2 [137]. Thus 33% coverage is a good approximation to the coverage expected for a TMD + (111) magnetic oxide heterostructure, a promising avenue of future investigation for valleytronics heterostructures.

We define valley splitting, ΔE_g, as the difference between the dipole-allowed single-particle band gaps at K and K', $E_g(K)$ and $E_g(K')$, respectively, which are the energies associated with the vertical transitions between the top-most valence band (VB) and the

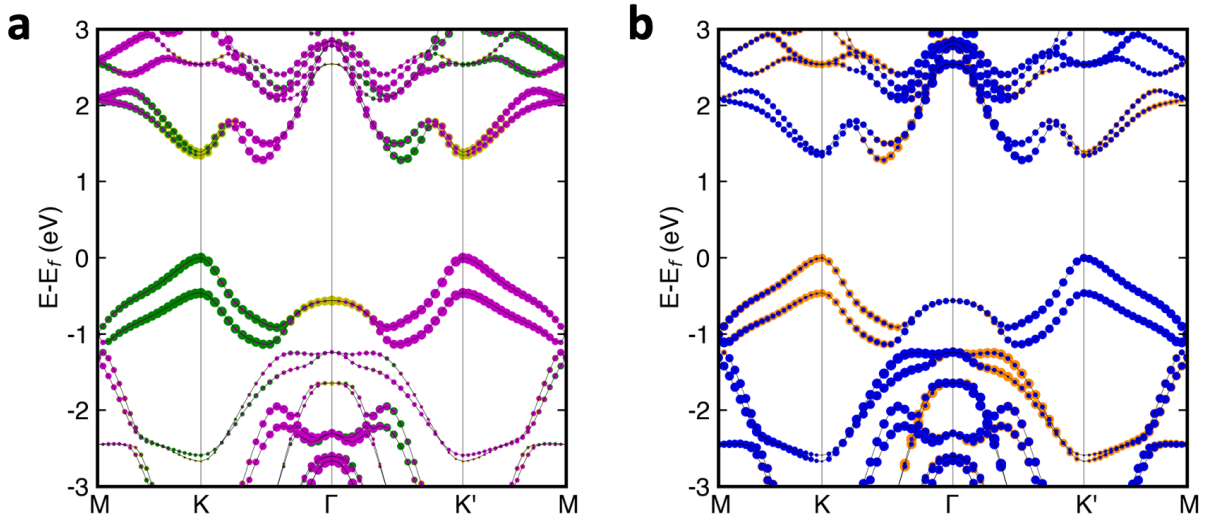


Figure 6.3: Spherical harmonics projections on the band structure of WSe_2. (a) Spherical harmonics projections $|\langle Y_l^m | n\mathbf{k}\sigma\rangle|^2$ centered on W sites, Y_2^{+2} in green, Y_2^{-2} in magenta and Y_2^0 in yellow. (b) Spherical harmonics projections for Se orbitals. Y_1^{+1} in orange and Y_1^{-1} in blue. Some mixing occurs in the conduction band at K', however the dominant contribution comes from Y_1^{+1}

lowest conduction band (CB) eigenvalues of the same spin (the lowest conduction band eigenvalue for MoS_2 and the second lowest conduction band eigenvalue for WSe_2). That is, we define

$$\Delta E_g = E_g(K') - E_g(K), \tag{6.1}$$

where

$$E_g(K) = E^{CB}_{K\uparrow} - E^{VB}_{K\uparrow} \tag{6.2}$$

and

$$E_g(K') = E^{CB}_{K'\downarrow} - E^{VB}_{K'\downarrow}, \tag{6.3}$$

with the spin index on $E^{VB/CB}_{K/K'}$ denoting the spin of the removed electron.

In a $\sqrt{3} \times \sqrt{3}$ supercell of a monolayer TMD, K and K' fold onto the Γ point of the corresponding BZ. The contributions from K and K' can be disentangled by projecting out the spin and spherical harmonic character of each band, which together create a unique signature. The VBMs of WSe_2 at K and K' are dominated by a combination of d_{xy} and $d_{x^2-y^2}$ orbital character [132, 136, 139–141] where the x and y Cartesian directions are taken to be in-plane, from which the Mo/W states can be uniquely decomposed into Y_2^{+2} and Y_2^{-2}

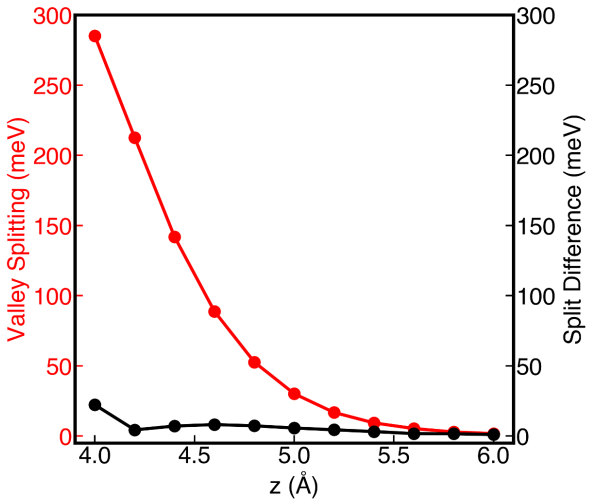


Figure 6.4: DFT-PBE Valley splitting (Eq. 6.1) for WSe_2 + Fe at 100% coverage (red) and difference between valley splitting (band gap split) and valence band splitting (Eq. 6.4) (black). The difference between the valley splitting and the valence band splitting is generally less than 5 meV and for the closest separations (< 4.5 Å) the difference is less than 10%.

character at K and K' respectively (Figure 6.3a). Here Y_l^m refers to the spherical harmonic function with orbital angular momentum quantum number l and orbital angular momentum magnetic quantum number m. The CBMs consist predominantly of d_{z^2} W/Mo orbitals which cannot be distinguished between K and K' because $m = 0$ for these orbitals; however, there are additional contributions from Se/S p_x and p_y orbitals which lend unique Y_1^{-1} and Y_1^{+1} character to the CBM at K and K' respectively (Figure 6.3b).

In what follows, we define the valence band (VB) splitting, ΔE_{VB}, as the difference between the topmost valence band at K and the topmost valence band at K' (see Fig. 6.5a), i.e.,

$$\Delta E_{VB} = E^{VB}_{K\uparrow} - E^{VB}_{K'\downarrow}. \tag{6.4}$$

This difference dominates the valley splitting for the monolayer TMDs considered here, generally deviating from the valley splitting itself by just a minimal amount for these systems (Figure 6.4), and thus will be used as a proxy for the valley-splitting, ΔE_g, in the discussion that follows.

6.4 Calculated Valence Band Splitting

The calculated VB splitting decays exponentially with increasing height (z) (Figure 6.5b) and varies sinusoidally with horizontal displacement (x) (Figure 6.5c). The nature of the

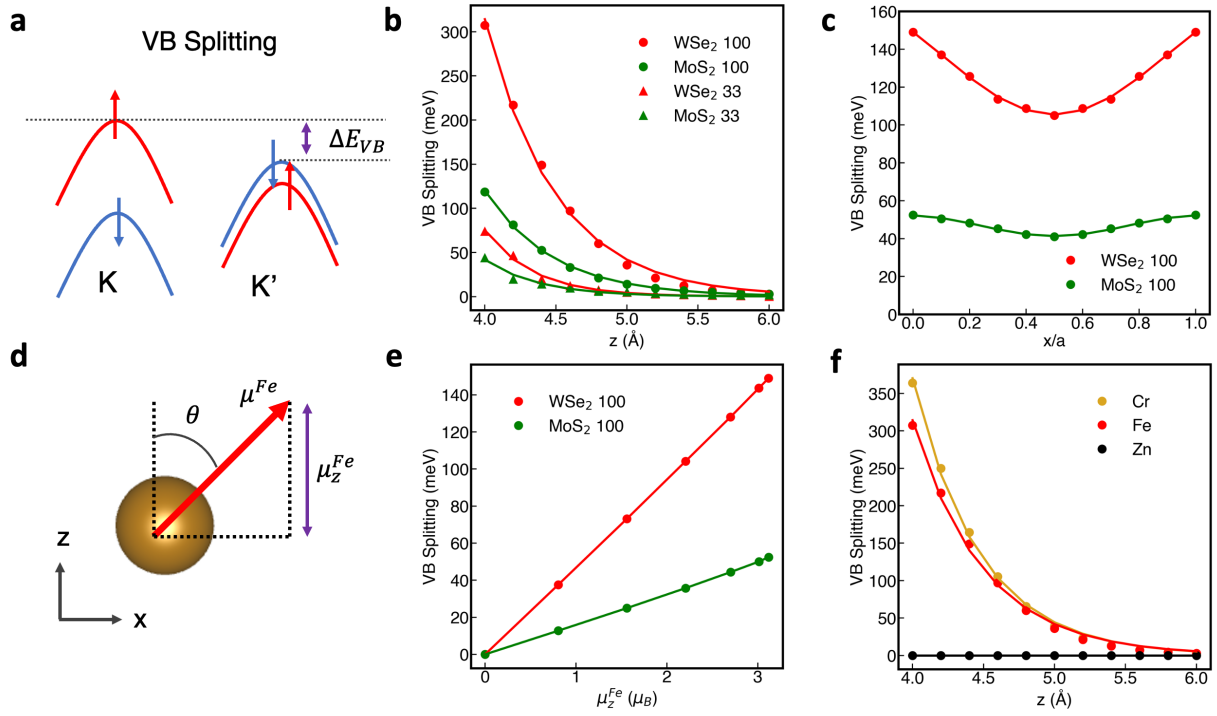


Figure 6.5: (a) Schematic illustrating definition of the valence band (VB) splitting (b) Valence band splitting of WSe_2 and MoS_2 with Fe atom at 100% and 33% coverage at variable Fe-W separations z. Circles and triangles are data points, solid lines are exponential fits. (c) Valence band splitting of WSe_2 and MoS_2 with Fe atom at 100% coverage with variable lateral position x and with z fixed at 4.4 Å. Lateral position is represented here as a fractional position along the a-axis (x/a) following the direction of the a-axis displayed in (Figure 6.1a). Circles are data points, solid lines are fits to cosines. (d) Schematic of canted Fe atom spin and definition of z component of magnetic moment. (e) Valence band splitting of WSe_2 and MoS_2 at 100% coverage with the magnetic moment of the Fe atom at variable angles with respect to the c axis, causing the z component of the magnetic moment to take different values. Circles are data points, solid lines are linear fits. (f) Valence band splitting of WSe_2 in the presence of different magnetic atoms, Fe, Cr and Zn. Circles are data points, solid lines are exponential fits.

variation of the splitting with height and lateral displacement reflects the important role of orbital overlap and hybridization between Fe and TMD states near the VBM on valley splitting, as has also been reported elsewhere for WSe_2+CrI_3 heterostructures [136]. At small separations, ∼4 Å, for 100% coverage of Fe atoms directly aligned over WSe_2, the calculated VB splitting is more than 300 meV, much larger than prior experimental reports of 1-16 meV [128–131], indicating that under more optimal conditions giant valley splittings are possible.

The maximum valley splitting values we report here for our model TMD+Fe system are, depending on the Fe atom height, between one and two orders of magnitude larger than those reported in prior experiments on TMDs supported by magnetic substrates [17, 125–131], and greater than any value yet reported experimentally or theoretically. In one prior first-principles study, the equilibrium W-Eu separation of WSe_2+EuS with a Eu-terminated surface was computed to be ∼4.4 Å with ∼1:3 coverage of Eu:W, leading to a predicted valley splitting of 8 meV [130]. Notably, at 100% Fe coverage and at a height of 4.4 Å we compute VB splittings of 148 meV and 52 meV for WSe_2 and MoS_2 respectively, with lateral W/Mo-Fe misalignment resulting in a maximum reduction of 29% and 21%, respectively, in the VB splitting. Should that be achievable experimentally, these VB splittings would be larger than any values yet observed. From the trends in valley splitting we compute here, we can rationalize lower values reported in prior theoretical and experimental work as resulting from imperfect lateral alignment and differing heights and orbital localization, depending on the magnetic atom and substrate. For example, although the magnetic Eu atoms in EuS have more localized f orbitals and a different ionic radius, for comparison at this W/Mo-Fe separation of 4.4 Å and coverage of 33%, we compute VB splittings of 20 meV and 14 meV, comparable numbers given the differences between Fe d and Eu f states and that the Eu-W alignment is not optimal [130]. To further illustrate the sensitivity of VB splitting to orbital overlap, we introduce a Hubbard U [28] for the Fe 3d states to compute the VB splitting, and find that it decreases from 148 meV for U = 0 to 60 meV for U = 7 eV (Appendix I: Figure 6.10) for WSe_2 with 100% coverage of Fe atoms at a separation of 4.4 Å.

We note that the VB splitting is also sensitive to the magnitude and orientation of the Fe magnetic moment. Systematically rotating the Fe moment clockwise off the z axis towards the x axis (Figure 6.5d), the VB splitting for WSe_2 and MoS_2 at 100% coverage at a fixed height of 4.4 Å is computed to decrease linearly with the z component of the magnetic moment of the Fe atom (Figure 6.5e). Replacing Fe with Cr in the 100% coverage case on WSe_2, we also observe a similar exponential decay with increasing z and similar dependence on magnetic moment (Figure 6.5f). Our DFT-PBE magnetic moment of Cr (3.7 μ_B) is larger than the magnetic moment of Fe (3.1 μ_B). The ratios of the VB splitting to the magnetic moment of Cr and Fe differ by only 2%, further validating the linear relationship between out-of-plane magnetic moment and VB splitting. The trend for Cr can be directly related to experimental results for the WSe_2+CrI_3 heterostructure. In our work the VB splitting predicted for WSe_2+Cr at the maximum W-Cr separation considered (6 Å) is 2.4 meV. Estimating the coverage of Cr atoms to W atoms to be 50% based on their respective lattice parameters we would expect the VB splitting to be ∼1 meV. Prior first-principles

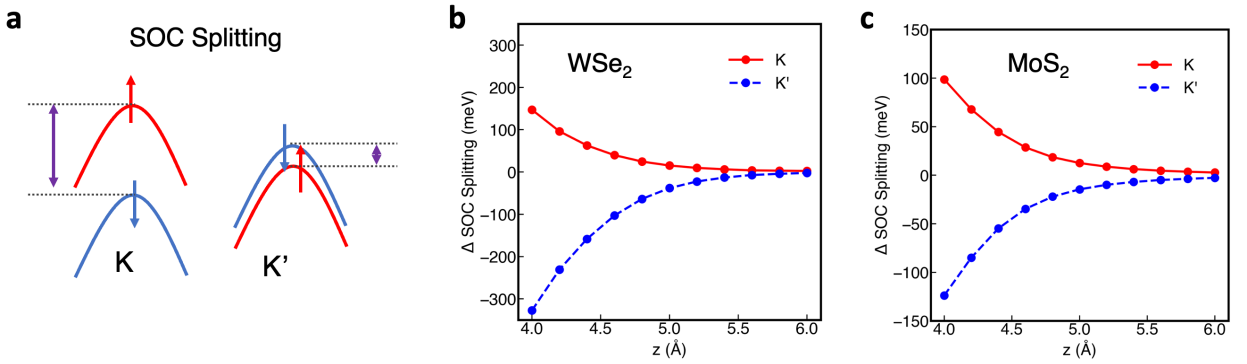


Figure 6.6: (a) Schematic of spin-orbit coupling (SOC) splitting at K and K' of TMD valence bands in the presence of Fe atom (b) Change in SOC splitting at K and K' relative to no Fe system for WSe_2+Fe atom system at 100% coverage and Fe directly above W with interpolation between data points. The absolute value of the SOC splitting in the absence of Fe is 459 meV. (c) Change in SOC splitting at K and K' relative to no Fe system for MoS_2+Fe atom system at 100% coverage and Fe directly above Mo. The absolute value of the SOC splitting in the absence of Fe is 146 meV.

calculations have predicted a W-Cr distance of 6.8 Å in this heterostructure [136], larger than our maximum value, but similar. Experimental studies have measured a valley splitting of 1-2 meV [129], very close to what our calculations would predict. Finally, as a sanity check, we confirm closed shell Zn, which has no magnetic moment, does not produce any VB splitting.

An asymmetry arises in the SOC splitting (Figure 6.6a) at K and K' with the presence of the Fe atoms; the Fe spin inducing valence band splitting does not affect K and K' equally and oppositely. The change in the SOC splitting at K induced by Fe can be expressed as

$$\Delta E_{VB}^{SOC} = (E_{K\uparrow}^{VB} - E_{K\downarrow}^{VB})_{TMD+Fe} - (E_{K\uparrow}^{VB} - E_{K\downarrow}^{VB})_{TMD}, \tag{6.5}$$

with an analogous expression for the change in the SOC splitting at K'. Going forward we drop the VB subscript used in Eq. 6.4 since all eigenvalues considered will be VB eigenvalues. For both WSe_2 and MoS_2 the change in the SOC splitting with Fe is significantly greater at K' than at K (Figure 6.6b,c), by a factor of two for WSe_2 for Fe magnetic moments oriented away from the TMD.

6.5 Superexchange Model Hamiltonian

To better understand our DFT calculations, we consider perturbative corrections to the TMD eigenvalues associated with TMD W/Mo-Fe d orbital overlap. For this analysis, we

use a model interacting Hamiltonian, H, with an off-diagonal coupling, H_{TMD+Fe}, written as

$$H = \sum_{\mathbf{k}\sigma} \epsilon_{n\mathbf{k}\sigma} c^{+}_{n\mathbf{k}\sigma} c_{n\mathbf{k}\sigma} + \sum_{\sigma} \epsilon_{Fe,\sigma} c^{+}_{Fe,\sigma} c_{Fe,\sigma} + H_{TMD+Fe} \tag{6.6}$$

where $\epsilon_{n\mathbf{k}\sigma}$ are the TMD eigenvalues at a given band n, k-point $\mathbf{k}$, and spin state σ; $\epsilon_{Fe,\sigma}$ are the Fe eigenvalues; and c^{+} and c are one-electron creation and annihilation operators for the TMD Bloch states (parametrized by band index n, k-point $\mathbf{k}$ and spin state σ) and localized Fe states with spin state σ [142, 143].

In what follows, we take the dilute monolayer limit and treat the Fe atom and its orbitals and spin state as localized, neglecting any coupling between Fe atoms. We focus on a term representing the interaction between an approximately half-filled Fe atom and a single spin on a Bloch state, i.e.,

$$H_{TMD+Fe} = \sum_{\mathbf{k}\mathbf{k}'\sigma\sigma'} J_{\mathbf{k}\mathbf{k}'} c^{+}_{n\mathbf{k}\sigma} c_{n\mathbf{k}'\sigma'} c^{+}_{Fe,\sigma'} c_{Fe,\sigma}, \tag{6.7}$$

where $J_{\mathbf{k}\mathbf{k}'}$ is a set of matrix elements involving overlaps between Fe orbitals and TMD Bloch states and spin indices on $J_{\mathbf{k}\mathbf{k}'}$ have been omitted for simplicity (see Appendix III for details 6.11). These $J_{\mathbf{k}\mathbf{k}'}$ will be treated as parameters in what follows, and set the energy scale for the effective exchange interaction. It should be noted that this coupling term is not the only possible coupling that may arise between the TMD and Fe atom (see Appendix II 6.10). We expect additional terms, such as a Hartree term, to arise as well. However, the H_{TMD+Fe} used in this work is the largest expected coupling contribution that affects K and K' differently, as will be seen in the following analysis. Since our objective is ultimately to model the difference between the eigenvalues at K and K', we neglect discussion of other coupling terms.

Our first-principles calculations show proximity to spin-up Fe electrons decreases the energy of the spin-down TMD eigenstate at K' and increases the energy of the spin-up TMD eigenstate at K. For this to be consistent with the above interaction Hamiltonian, the matrix elements $J_{\mathbf{k}\mathbf{k}'}$ must promote an antiferromagnetic interaction leading us to conclude the $J_{\mathbf{k}\mathbf{k}'}$ which appear above are not related to direct exchange, which would have the wrong sign for $J_{\mathbf{k}\mathbf{k}'}$, but rather a superexchange mechanism. Our focus on this term has analogies with Anderson's analysis of half-filled d orbitals interacting with one another where the dominant second-order term in the kinetic and ionic potential energy represents double-hopping, or superexchange [142].The difference here is that one of the spins, associated with the Fe atom, is localized in real space; the other, associated with a TMD Bloch function at K or K', is localized in reciprocal space. We write the eigenstates of the uncoupled TMD+Fe system as tensor products of TMD Bloch states and localized Fe spin states $|n\mathbf{k}\sigma\rangle \otimes |Fe,\sigma\rangle = |n\mathbf{k}\sigma;\sigma_{Fe}\rangle$. We simplify this further by treating the Fe atom spins as a single unit with total spin S and total spin magnetic quantum number M_s^{Fe} so that our states can be labeled as $|n\mathbf{k}\sigma;M_s^{Fe}\rangle$.

Treating H_{TMD+Fe} in Eq. 6.6 as a perturbation to the TMD VB eigenvalues at K and K', the corrected eigenvalues to second order become:

$$E_{K\uparrow} = E^0_{K\uparrow} + M_s^{Fe} J_{KK} + \sum_{\mathbf{k}'} |J_{K\mathbf{k}'}|^2 \left[\frac{(M_s^{Fe})^2}{E_{K\uparrow} - E_{\mathbf{k}'\uparrow}} + \frac{S(S+1) - M_s^{Fe}(M_s^{Fe}+1)}{E_{K\uparrow} - E_{\mathbf{k}'\downarrow}} \right] \quad (6.8)$$

and

$$E_{K'\downarrow} = E^0_{K'\downarrow} - M_s^{Fe} J_{K'K'} + \sum_{\mathbf{k}'} |J_{K'\mathbf{k}'}|^2 \left[\frac{(M_s^{Fe})^2}{E_{K'\downarrow} - E_{\mathbf{k}'\downarrow}} + \frac{S(S+1) - M_s^{Fe}(M_s^{Fe}-1)}{E_{K'\downarrow} - E_{\mathbf{k}'\uparrow}} \right] \quad (6.9)$$

where M_s^{Fe} and S are taken to be $\frac{3}{2}$, based on the calculated DFT-PBE value of the magnetic moment of the Fe atom (3.1 μ_B) and assuming a gyromagnetic ratio of $\gamma \approx 2$. It should again be noted that there should be further corrections arising from other coupling interactions, but that those interactions are expected to produce identical corrections to the eigenvalues at K and K'.

In principle, the $\mathbf{k}$-dependence of $J_{\mathbf{k}\mathbf{k}'}$ will be related to details of the overlap between the itinerant Bloch TMD states and localized Fe states. Since the TMD VB eigenfunctions at K and K' differ only by a phase, consisting of contributions from 5d/4d orbitals with spherical harmonics Y_2^{+2} and Y_2^{-2} respectively (Figure 6.3a), we expect $J_{KK} = J_{K'K'} = J$. To further simplify as much as possible, we assume minimal $\mathbf{k}$-dependence of $J_{\mathbf{k}\mathbf{k}'}$ near K and K', and approximate that $J_{K\mathbf{k}'} \approx J_{KK}$ and $J_{K'\mathbf{k}'} \approx J_{K'K'}$, with contributions from neighboring k points weighted by how similar their wave functions are to those of the VBM at K and K', equivalently $J_{K\mathbf{k}'} = Jw(\mathbf{k}')$ and $J_{K'\mathbf{k}'} = Jw(\mathbf{k}')$. This is a reasonable assumption because the orbital character in the neighboring Bloch states in the top and bottom TMD VBs consist predominantly of 5d/4d orbitals with Y_2^{+2} and Y_2^{-2} spherical harmonics. With these approximations, we can pull J out of the summations, and define the constants

$$\alpha = \sum_{\mathbf{k}'} \frac{w(\mathbf{k}')}{E_{K\uparrow} - E_{\mathbf{k}'\uparrow}} = \sum_{\mathbf{k}'} \frac{w(\mathbf{k}')}{E_{K'\downarrow} - E_{\mathbf{k}'\downarrow}} \quad (6.10)$$

and

$$\beta = \sum_{\mathbf{k}'} \frac{w(\mathbf{k}')}{E_{K\uparrow} - E_{\mathbf{k}'\downarrow}} = \sum_{\mathbf{k}'} \frac{w(\mathbf{k}')}{E_{K'\downarrow} - E_{\mathbf{k}'\uparrow}} \quad (6.11)$$

for the same-spin and spin-flip summations over the top VB and bottom VB respectively.

It follows from these approximations that an asymmetry in the magnitude of the valence band eigenvalue shifts at K and K' arises at second order. Capturing this asymmetry is necessary to rationalize the manner in which the VB SOC splitting (top VB minus bottom VB, Figure 6.6a) changes with z (Figure 6.6b). To first order in J, equal and opposite changes in the SOC splitting would be expected. However, the first order term alone cannot lead to the valence band splitting seen in our DFT calculations. From our model, the second-order

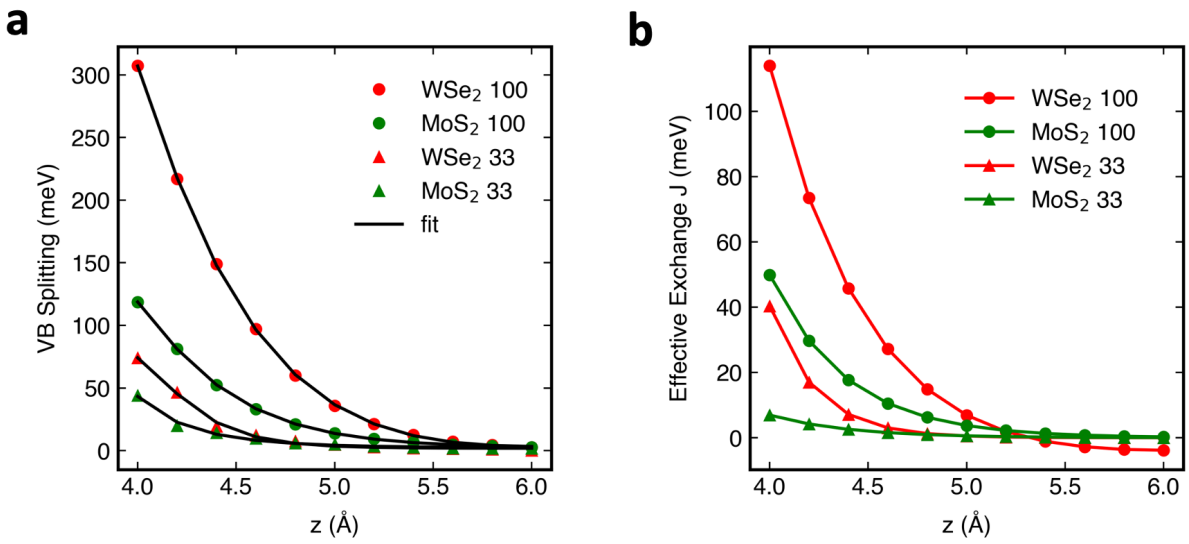


Figure 6.7: (a) Valence band splitting for WSe_2 and MoS_2 for 100% coverage and 33% coverage (with the Fe atoms positioned directly on top of the W and Mo atoms), same as Fig. 6.5b, and fits to the valence band splitting model (b) Fitted values of effective exchange J arising from the superexchange interaction for WSe_2 and MoS_2 for 100% and 33% coverage.

terms in J lead to the asymmetry in this splitting, and hence the valley splitting at lowest order (see Appendix III 6.11 for further details).

To understand the trends in the VB splitting predicted by this model, we take the difference between the two perturbed eigenvalues, ΔE_{VB}, which reduces to

$$\Delta E_{VB} = E_{K\uparrow} - E_{K'\downarrow} = 2M_s^{Fe}(J - J^2\beta). \tag{6.12}$$

When the Fe atom spin is canted by an angle θ away from the z axis and clockwise towards the x axis (Figure 6.5d), $|\mathbf{k}\sigma; M_s^{Fe}\rangle \rightarrow e^{-iS_y\theta}\,|\mathbf{k}\sigma; M_s^{Fe}\rangle$ and the corresponding expression for the VB splitting is modified to (see Appendix IV 6.12)

$$\Delta E_{VB} = E_{K\uparrow} - E_{K'\downarrow} = 2M_s^{Fe}\cos\theta(J - J^2\beta). \tag{6.13}$$

Here $2M_s^{Fe}\cos\theta$ corresponds to the z component of the Fe magnetic moment μ_z^{Fe}.

From our DFT calculations, we know J to be sensitive to both the height z and the lateral alignment. As J involves matrix elements between Fe and TMD states – with dominant Fe and Mo/W d atomic orbital character – we assume J to have the form

$$J(z) = ae^{-bz}f(z) \tag{6.14}$$

where $f(z)$ is a polynomial, a generic form consistent with the relevant states being hydrogenic 3d and 5d/4d atomic orbitals, respectively.

We fit Eqs. 6.13 and 6.14 to the DFT-PBE VB eigenvalue splitting (Fig. 6.5b, 6.7a) as a function of vertical displacement z for WSe_2 and MoS_2 at 100% and 33% coverage.

From Figure 6.7b we see that WSe_2 exhibits a larger J than MoS_2 at a given separation, consistent with 5d orbitals having a greater spatial extent than 4d orbitals. The J calculated here contains an implicit dependence on the coverage of the magnetic atoms. For both WSe_2 and MoS_2, J for the 100% coverage case is 6 times larger than J for the 33% coverage case at a relevant height z of 4.4 Å, larger than the expected factor of 3 assuming a linear dependence on coverage. This may be because for the 100% coverage case, each Mo and W could potentially interact with neighboring Fe atoms, beyond the one that is aligned directly above the transition metal. It could also be associated with dispersion and k-dependence of the Fe states, which is neglected in our model. Nevertheless, this second-order superexchange model captures the trends exceedingly well, allowing us to use this for intuition in the future design of valleytronics interfaces.

6.6 General Design Principles for Valleytronics Interfaces

Based on these results and our model, we can summarize general principles that can guide development of optimal magnetic substrates for large valley splitting and valleytronics applications. First, the vertical proximity (z) between the W/Mo ion and the magnetic atom in the substrate must be reduced as much as possible while keeping the valley degree of freedom in the TMD intact. Reducing the distance between the TMD transition metal (W/Mo) and the magnetic atom in the magnetic substrate could be achieved, for example, by using magnetic substrates that are terminated by the magnetic atom. Because of the exponential nature of this effect, 1 Å of additional distance between a magnetic atom and the TMD transition metal atom due to the addition of, for example, oxygen on the surface can reduce the valley splitting by an order of magnitude.

Second, lateral alignment (x) of the TMD transition metal (W/Mo) with the magnetic atom must be optimized. This can be achieved by identifying magnetic substrates with good lattice parameter matching to the selected TMD. Although important, lateral alignment is not as sensitive as the vertical proximity as it only leads to a sinusoidal variation in valley splitting, decreasing it by ∼20% at maximal misalignment. In prior experimental studies of TMDs with substrates like EuS and CrI_3, the small valley splitting, ∼1-16 meV, can be understood by considering the low coverage and significant lattice parameter mismatch, leading to poor alignment of the W/Mo atoms with the magnetic Eu and Cr atoms. As previously discussed, perovskite-related magnetic oxides may offer better lattice alignment and coverage, and therefore are an avenue worth further study.

Third, we find that the out-of-plane magnetic moment of the magnetic atom must be

	a_{exp}(Å)	a_{DFT}(Å)
$\sqrt{3} \times \sqrt{3}$ WSe_2	5.70	5.71
(111)-$BiFeO_3$	5.58	5.62

Table 6.1: Experimental and DFT-PBE+U a-lattice parameter for a $\sqrt{3} \times \sqrt{3}$ supercell of WSe_2 and (111)-$BiFeO_3$.

maximized. This can be achieved by tuning the chemical identity, oxidation state, or local environment of the magnetic atom so that it has a larger magnetic moment and out-of-plane easy axis. It should be noted that this requirement is not as critical as the proximity requirements; valley splitting only decreases linearly with decreasing out-of-plane magnetic moment, not exponentially. This indicates that even substrates with canted magnetic moments could still produce valley splitting, so long as the proximity and alignment of the magnetic atoms to the W/Mo atoms is optimized.

Fourth, maximizing the radial extent of the TMD transition metal and the magnetic atoms will amplify the effective exchange J which increases with increasing orbital overlap, or equivalently, with increasing radial extent of both the TMD Bloch state (dominated by the transition metal W/Mo) and the magnetic atom. Since the valence band splitting increases with increasing J, this implies that valley splitting can be maximized by using larger transition metals in the TMD (W) and by using magnetic substrates with magnetic atoms that have larger radial extent.

6.7 Model System: WSe_2+(111)-$BiFeO_3$

In order to validate the trends observed in the TMD+Fe systems, we perform further calculations on WSe_2 with an actual magnetic substrate. As mentioned in Section 6.3, the in-plane lattice parameters of the (111) surface of $BiFeO_3$ match well with those of a $\sqrt{3} \times \sqrt{3}$ supercell of WSe_2 (Table 6.1). In such a heterostructure, the Fe ions correspond to 33% coverage of Fe ions to W ions.

The (111) surface of $BiFeO_3$ itself is not suitable for producing large valley splitting. The primary problem is that while alternating layers of Fe ions in the (111) planes are ferromagnetically ordered (with AFM ordering between alternating planes), the magnetic moments are oriented in-plane [144] (Figure 6.8a). Further, oxides are generally oxygen-terminated, which introduces an extra ∼1 Å of separation between the WSe_2 and the Fe ions even in the case where the surface is terminated by Fe octahedra.

Rather than study physical (111)-$BiFeO_3$, we use the crystal structure of $BiFeO_3$ as a scaffold upon which to perform calculations on an idealized structure, in an effort to set an upper bound on the achievable valley splitting that could be produced by a magnetic oxide substrate. We construct a supercell of a WSe_2 + (111)-$BiFeO_3$ heterostructure in which

the in-plane FM orderings are directed entirely out-of-plane and the surface of $BiFeO_3$ is Fe-terminated (Figure 6.8b).

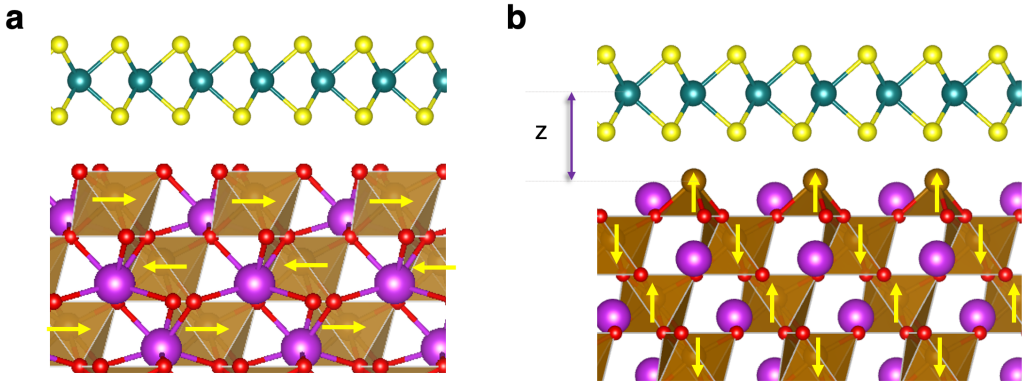


Figure 6.8: The crystal structure of a WSe_2+(111)-$BiFeO_3$ with (a) the experimentally observed magnetic ordering and O termination and (b) the fictitious version of (111)-$BiFeO_3$ with out-of-plane magnetic ordering and Fe termination. The definition of z, the separation between W and Fe ions is indicated in (b). W ions are turquoise, Se ions are yellow, Fe ions are brown, Bi ions are purple, and O ions are red.

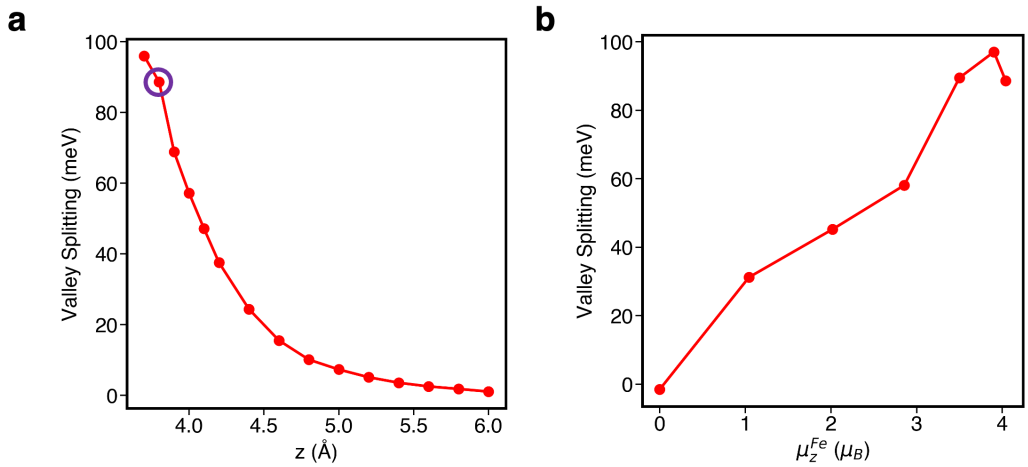


Figure 6.9: The calculated valley splitting in the fictitious WSe_2+(111)-$BiFeO_3$ heterostructure as a function of (a) vertical proximity and (b) out-of-plane magnetic moment. The valley splitting at the equilibrium separation is indicated with the purple circle in (a).

We performed calculations to study the valley splitting (Eq.6.1) as a function of Fe-W spacing (z) by varying the height of the WSe_2 above the surface of the fictitious (111)-$BiFeO_3$ surface with the W ions aligned directly above Fe ions. The calculated valley splitting as a function of vertical proximity exhibits the same exponential trend as observed in the TMD+Fe systems (Figure 6.5). At the equilibrium spacing (z) the calculated valley splitting is 85 meV (Figure 6.9a). We perform further calculations to determine the dependence of the valley splitting on the out-of-plane moments of the Fe ions and find a similar linear-like trend (Figure 6.9b). The deviations from linearity are attributed to the difficulty in converging these calculations and we expect that future work will reveal a smoother linear trend.

The conclusion that we draw is that magnetic oxides with optimized lattice parameters, magnetic ordering, and surface termination could be excellent candidates for producing large valley splittings. In our idealized system we observed a valley splitting of 85 meV, larger than any value observed experimentally to date.

6.8 Outlook

Motivated by recent experiments, and using first-principles density functional theory calculations, we have studied in detail trends in valley splitting of monolayer TMDs with the proximity, alignment, and coverage of overlayers of magnetic atoms. We find large valley splittings for optimal geometries – in which magnetic atoms are well aligned sitting atop each TMD TM atom – that are one to two orders of magnitude larger than previously reported. Our analysis indicates that an orbital overlap-driven superexchange interaction drives valley splitting in TMDs supported by magnetic substrates. By systematically varying the placement and coverage of magnetic atoms at two different coverages, we have pinpointed and explored the differing shifts in the valence band eigenvalues at K and K' giving rise to valley splitting. Through analysis of expressions originating with second-order perturbation theory in a model coupling Hamiltonian between the magnetic atoms and the TMD, we have elucidated the dependence of the valley splitting on the superexchange interaction. Further, by considering an idealized magnetic substrate based on the crystal structure of (111)-$BiFeO_3$ we calculate that an 85 meV valley splitting could be produced in WSe_2, larger than any as-yet observed experimental value, motivating magnetic oxides as a search-space for future valleytronics heterostructures.

6.9 Appendix I: Effects of Hubbard U on Valley Splitting Calculations

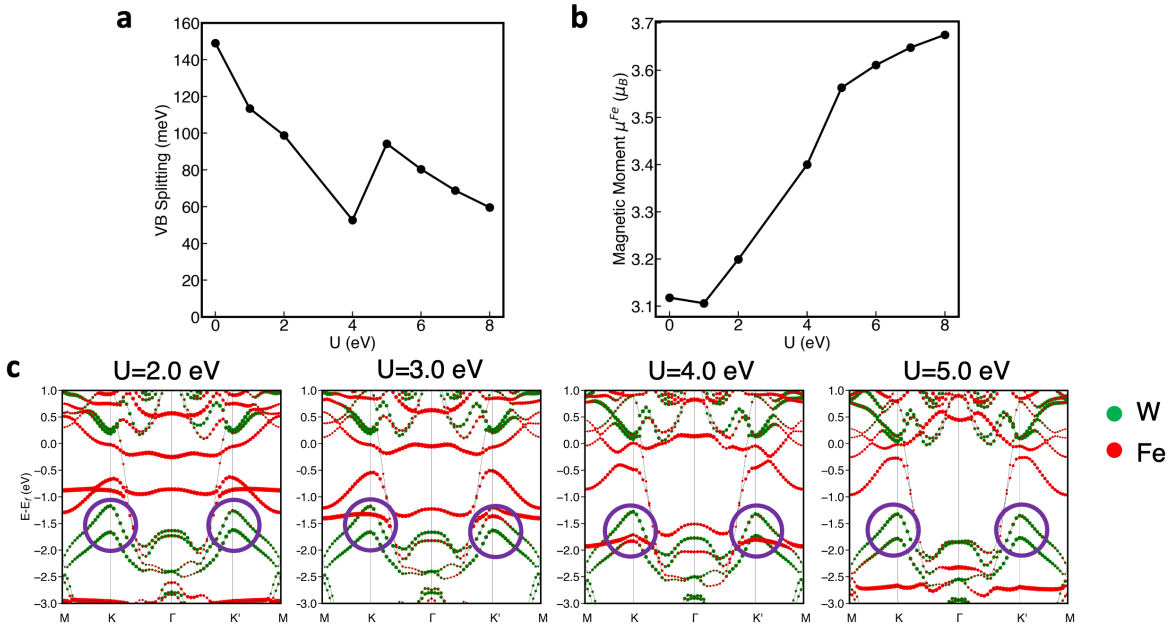


Figure 6.10: (a) Valence band splitting of WSe_2 with 100% coverage of Fe atoms at fixed 4.4 Å Fe-W separation as a function of effective Hubbard U. (b) Corresponding magnetic moment of Fe atom as a function of effective Hubbard U. (c) Element-specific orbital projected band structures of WSe_2+Fe with various Hubbard U values applied to the d states of Fe.

Applying a Hubbard U to the Fe atom in the TMD+Fe system is expected to decrease valley splitting as it causes the Fe orbitals to become more localized. We investigated the effect of applying Hubbard U to the Fe atom in the 100% coverage case with a Fe-W separation of 4.4 Å. The valence band splitting decreases from U = 0-4 eV, then increases at U = 5 eV and decreases again for larger values of U (Figure 6.10a). The magnetic moment of the Fe atom systematically increases as the Hubbard U value is increased (Figure 6.10b). The element-specific orbital projected band structures of WSe_2+Fe are plotted in Figure 6.10c. The Fe orbital projections are in red and the W orbital projections are in green. At U = 2 eV and U = 5 eV the localized Fe bands are above and below the WSe_2 VBs respectively. At U = 3 eV and U = 4 eV resonances occur between a localized Fe band and the WSe_2 valence bands, interfering with the VB splitting. This results in the discontinuity in the monotonic decrease in the VB splitting with increasing U. The resonance between the localized Fe d

states and the top-most part of the WSe_2 VBs at U = 3 eV is so significant that a VB splitting cannot be defined.

6.10 Appendix II: Calculated Valence Band Eigenvalues

In order to calculate VB eigenvalues of the WSe_2 + Fe (Figure 6.11b) and of the MoS_2 + Fe (Figure 6.11c) systems, the electrostatic potential along the z-axis is calculated to determine the absolute vacuum level to use as a reference so that spurious changes in the Fermi energy as a result of occupied Fe states do not misconvey the TMD eigenvalue trends. The order of magnitude of the changes in the VB eigenvalues is substantially larger than the calculated J superexchange parameters indicating that the superexchange coupling cannot fully describe the changes in the eigenvalues. This is to be expected as additional coupling terms, such as a Hartree term, should also contribute to H_{TMD+Fe}. In our analysis we neglected such terms as they are expected to affect the eigenvalues at K and K' equally. Our perturbative approach should be sufficient to capture the dominant contributions that affect K and K' differently, leading to the observed VB splitting, which is the primary focus of this work. To fully understand the changes in the individual VB eigenvalues as a result of proximity to the Fe atom, a more detailed analysis would be necessary.

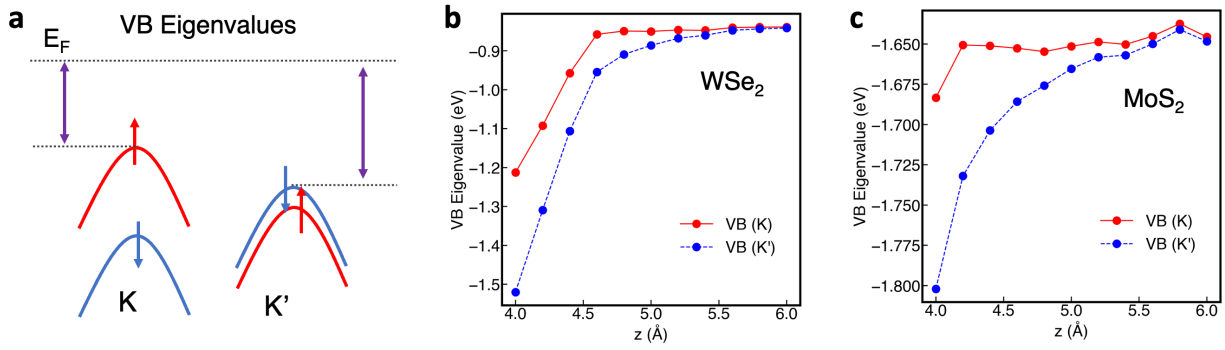


Figure 6.11: (a) Schematic of valence band eigenvalues measured relative to the Fermi energy (b) Variation in valence band eigenvalues of WSe_2 + Fe system at 100% coverage with varying W-Fe separation z (c) Variation in valence band eigenvalues of MoS_2 + Fe system at 100% coverage with varying Mo-Fe separation z.

6.11 Appendix III: Justification for taking perturbative approach to second order

At first order in perturbation theory, the VBM SOC splittings at K and K' are given by:

$$\begin{aligned}\Delta E^{SOC}_{VB,K} &= \langle K\uparrow|H_{TMD+Fe}|K\uparrow\rangle - \langle K\downarrow|H_{TMD+Fe}|K\downarrow\rangle \\ &= \Delta E^{SOC}_{VB,0} + (J_{K\uparrow K\uparrow} + J_{K\downarrow K\downarrow})M_s^{Fe} \end{aligned} \tag{6.15}$$

and

$$\begin{aligned}\Delta E^{SOC}_{VB,K'} &= \langle K'\downarrow|H_{TMD+Fe}|K'\downarrow\rangle - \langle K'\uparrow|H_{TMD+Fe}|K'\uparrow\rangle \\ &= \Delta E^{SOC}_{VB,0} - (J_{K'\downarrow K'\downarrow} + J_{K'\uparrow K'\uparrow})M_s^{Fe}, \end{aligned} \tag{6.16}$$

where it is understood that the relevant bands are the two SOC split valence bands and

$$\Delta E^{SOC}_{VB,0} = E^0_{K\uparrow} - E^0_{K\downarrow} = E^0_{K'\downarrow} - E^0_{K'\uparrow} \tag{6.17}$$

is the unperturbed TMD SOC splitting which is the same at K and K'. A subtle issue is that while in principle there are enough unique couplings appearing in Eqns. 6.15 and 6.16 to rationalize the asymmetry seen in Fig 6.6, in practice we expect the K and K' VBM SOC splitting predicted with these formulas to be very similar. For the unperturbed TMD the cell periodic part of the Bloch functions associated with each VB state $u_{K\uparrow}(r) \sim u_{K'\downarrow}(r) \approx u_{K'\uparrow}(r)$ where the $\sim$ denotes equal up to a phase. The first part of the above follows from time-reversal symmetry while the second part is only approximately true but becomes exact in the limit where SOC is turned off. The later can also be seen numerically and $u_{K'\uparrow}(r) \approx u_{K'\downarrow}(r)$ as can be seen by examining the calculated spherical harmonics projections in the K valleys (Figure 6.3). By this argument it is reasonable to assume $J_{K\uparrow K\uparrow} \approx J_{K'\uparrow K'\uparrow}$ and analogously that $J_{K\downarrow K\downarrow} \approx J_{K'\downarrow K'\downarrow}$. It is readily verified that in this limit $\Delta E^{SOC}_{VB,K} \approx -\Delta E^{SOC}_{VB,K'}$, i.e. the magnitude of the VBM SOC splitting is equivalent and we are unable to explain the asymmetric SOC splitting in the VBM seen in Fig. 6.6.

A solution appears if we continue the analysis at second order in perturbation theory where spin-flip processes are allowed. At this order in perturbation theory, we find an asymmetry appears even when all exchange coupling constants are taken equal, ie. $J_{K\uparrow K\uparrow} = J_{K'\uparrow K'\uparrow} = J_{K\downarrow K\downarrow} = J_{K'\downarrow K'\downarrow} = J$. The similarity in the Bloch functions, their equality in the absence of SOC, and the expectation that wave functions with similar spatial extent should overlap with Fe states similarly makes it reasonable to assume $J_{K\uparrow K\uparrow} \approx J_{K\downarrow K\downarrow}$ and $J_{K'\downarrow K'\downarrow} \approx J_{K'\uparrow K'\uparrow}$. Then the eigenvalues for the four VB states are

$$E_{K\uparrow} = E^0_{K\uparrow} + M_s^{Fe}J_{KK} + \sum_{\mathbf{k'}} |J_{K\mathbf{k'}}|^2 \left[\frac{(M_s^{Fe})^2}{E_{K\uparrow} - E_{\mathbf{k'}\uparrow}} + \frac{S(S+1) - M_s^{Fe}(M_s^{Fe}+1)}{E_{K\uparrow} - E_{\mathbf{k'}\downarrow}}\right]; \tag{6.18}$$

$$E_{K\downarrow} = E^0_{K\downarrow} - M_s^{Fe}J_{KK} + \sum_{\mathbf{k'}} |J_{K\mathbf{k'}}|^2 \left[\frac{(M_s^{Fe})^2}{E_{K\downarrow} - E_{\mathbf{k'}\downarrow}} + \frac{S(S+1) - M_s^{Fe}(M_s^{Fe}-1)}{E_{K\downarrow} - E_{\mathbf{k'}\uparrow}}\right]; \tag{6.19}$$

$$E_{K'\downarrow} = E^0_{K'\downarrow} - M_s^{Fe} J_{K'K'} + \sum_{\mathbf{k'}} |J_{K'\mathbf{k'}}|^2 \left[\frac{(M_s^{Fe})^2}{E_{K'\downarrow} - E_{\mathbf{k'}\downarrow}} + \frac{S(S+1) - M_s^{Fe}(M_s^{Fe}-1)}{E_{K'\downarrow} - E_{\mathbf{k'}\uparrow}} \right]; \quad (6.20)$$

and

$$E_{K'\uparrow} = E^0_{K'\uparrow} + M_s^{Fe} J_{K'K'} + \sum_{\mathbf{k'}} |J_{K'\mathbf{k'}}|^2 \left[\frac{(M_s^{Fe})^2}{E_{K'\uparrow} - E_{\mathbf{k'}\uparrow}} + \frac{S(S+1) - M_s^{Fe}(M_s^{Fe}+1)}{E_{K'\uparrow} - E_{\mathbf{k'}\downarrow}} \right] \quad (6.21)$$

The SOC splitting at K and K' become

$$\begin{aligned} \Delta E^{SOC}_{VB,K} \quad &= \Delta E^{SOC}_{VB,0} + 2M_s^{Fe} J + J^2 \{ (\alpha_{K\uparrow} - \alpha_{K\downarrow})(M_s^{Fe})^2 \\ &+ \beta_{K\uparrow}[S(S+1) - M_s^{Fe}(M_s^{Fe}+1)] - \beta_{K\downarrow}[S(S+1) - M_s^{Fe}(M_s^{Fe}-1)] \} \end{aligned} \quad (6.22)$$

and

$$\begin{aligned} \Delta E^{SOC}_{VB,K'} \quad &= \Delta E^{SOC}_{VB,0} - 2M_s^{Fe} J + J^2 \{ (\alpha_{K'\downarrow} - \alpha_{K'\uparrow})(M_s^{Fe})^2 \\ &+ \beta_{K'\downarrow}[S(S+1) - M_s^{Fe}(M_s^{Fe}-1)] - \beta_{K'\uparrow}[S(S+1) - M_s^{Fe}(M_s^{Fe}+1)] \} \end{aligned} \quad (6.23)$$

where α and β are as defined in Eqs. 6.10 and 6.11, namely the second order summations over same-spin and opposite-spin states in the unperturbed TMD band structure. By time-reversal symmetry $\beta_{K\uparrow} = \beta_{K'\downarrow}$ and $\beta_{K\downarrow} = \beta_{K'\uparrow}$ (where the former pair of βs is the same as the β appearing in the main text, with a top-most VB eigenvalue in the denominator and the latter differs in that it has a bottom VB eigenvalue in the denominator). However, $\beta_{K\uparrow} \neq \beta_{K'\uparrow}$ and $\beta_{K\downarrow} \neq \beta_{K'\downarrow}$. This is because (a) the dispersion of the top and bottom valence bands are not the same and (b) the summations differ by a sign. Due to this, it is clear that an asymmetry arises at second order, necessitating going to second order in the perturbative expansion of the valence band eigenvalues to explain the difference in the SOC splitting trends at K and K'.

6.12 Appendix IV: Derivation of Canted Spin VB Splitting

The coupling term in the Hamiltonian H_{TMD+Fe} can be rewritten

$$H_{TMD+Fe} = \sum_{\mathbf{kk'}} J_{\mathbf{kk'}} [S^z_{Fe}(c^+_{\mathbf{k}\uparrow} c_{\mathbf{k'}\uparrow} - c^+_{\mathbf{k}\downarrow} c_{\mathbf{k'}\downarrow}) + S^+_{Fe} c^+_{\mathbf{k}\downarrow} c_{\mathbf{k'}\uparrow} + S^-_{Fe} c^+_{\mathbf{k}\uparrow} c_{\mathbf{k'}\downarrow}] \quad (6.24)$$

where

$$S^z_{Fe} = \frac{1}{2}(c^+_{Fe\uparrow} c_{Fe\uparrow} - c^+_{Fe\downarrow} c_{Fe\downarrow}) \quad (6.25)$$

$$S^+_{Fe} = c^+_{Fe\uparrow} c_{Fe\downarrow} \quad (6.26)$$

$$S^-_{Fe} = c^+_{Fe\downarrow} c_{Fe\uparrow} \tag{6.27}$$

and

$$S^z_{Fe}|M^{Fe}_s >= M^{Fe}_s|M^{Fe}_s > \tag{6.28}$$

$$S^+_{Fe}|M^{Fe}_s >= \sqrt{S(S+1) - M^{Fe}_s(M^{Fe}_s+1)}|M^{Fe}_s + 1 > \tag{6.29}$$

$$S^-_{Fe}|M^{Fe}_s >= \sqrt{S(S+1) - M^{Fe}_s(M^{Fe}_s-1)}|M^{Fe}_s - 1 > . \tag{6.30}$$

When the magnetic moment M^{Fe}_s is rotated clockwise by an angle θ away from the z axis towards the x axis, the unperturbed eigenstates undergo the transformation

$$|\mathbf{k}\sigma; M^{Fe}_s > \rightarrow e^{-iS^y_{Fe}\theta}|\mathbf{k}\sigma; M^{Fe}_s > . \tag{6.31}$$

The Hamiltonian matrix elements become

$$< \mathbf{k}\sigma; M^{Fe}_s|e^{iS^y_{Fe}\theta} H_{TMD+Fe} e^{-iS^y_{Fe}\theta}|\mathbf{k'}\sigma'; M^{Fe}_s > . \tag{6.32}$$

To determine the first and second order perturbations to the eigenvalues arising from H_{TMD+Fe} we apply unitary rotation operators to the Hamiltonian H_{TMD+Fe}. Using the Baker-Campbell-Hausdorf equation:

$$e^A B e^{-A} = B + [A,B] + \frac{1}{2!}[A[A,B]] + \frac{1}{3!}[A,[A,[A,B]]] + ... \tag{6.33}$$

We find

$$e^{iS^y_{Fe}\theta} S^z_{Fe} e^{-iS^y_{Fe}\theta} = S^z_{Fe}\cos\theta - \frac{1}{2}(S^+_{Fe} + S^-_{Fe})\sin\theta, \tag{6.34}$$

$$e^{iS^y_{Fe}\theta} S^+_{Fe} e^{-iS^y_{Fe}\theta} = \frac{1}{2}S^+_{Fe}(\cos\theta + 1) + \frac{1}{2}S^-_{Fe}(\cos\theta - 1) + iS^z_{Fe}\sin\theta, \tag{6.35}$$

and

$$e^{iS^y_{Fe}\theta} S^-_{Fe} e^{-iS^y_{Fe}\theta} = \frac{1}{2}S^+_{Fe}(\cos\theta - 1) + \frac{1}{2}S^-_{Fe}(\cos\theta + 1) + iS^z_{Fe}\sin\theta. \tag{6.36}$$

Using these expressions we find the first and second order perturbations to the energy eigenvalues due to H_{TMD+Fe} are

$$E^{(1)}_{K\uparrow} = J_{KK} M^{Fe}_s \cos\theta \tag{6.37}$$

and

$$E^{(1)}_{K'\downarrow} = -J_{K'K'} M^{Fe}_s \cos\theta, \tag{6.38}$$

and

$$E^{(2)}_{K\uparrow} = \sum_{\mathbf{k'}} |J_{K\mathbf{k'}}|^2 \Bigg[\frac{(M_s^{Fe})^2 \cos^2\theta + \frac{1}{2}\sin^2\theta(S(S+1) - (M_s^{Fe})^2)}{E_{K\uparrow} - E_{\mathbf{k'}\uparrow}} + \frac{(M_s^{Fe})^2 \sin^2\theta + \frac{1}{2}(S(S+1) - (M_s^{Fe})^2)(\cos^2\theta + 1) - M_s^{Fe} cos\theta}{E_{K\uparrow} - E_{\mathbf{k'}\downarrow}} \Bigg] \tag{6.39}$$

and

$$E^{(2)}_{K'\downarrow} = \sum_{\mathbf{k'}} |J_{K'\mathbf{k'}}|^2 \Bigg[\frac{(M_s^{Fe})^2 \cos^2\theta + \frac{1}{2}\sin^2\theta(S(S+1) - (M_s^{Fe})^2)}{E_{K'\downarrow} - E_{\mathbf{k'}\downarrow}} + \frac{(M_s^{Fe})^2 \sin^2\theta + \frac{1}{2}(S(S+1) - (M_s^{Fe})^2)(\cos^2\theta + 1) + M_s^{Fe} cos\theta}{E_{K'\downarrow} - E_{\mathbf{k'}\uparrow}} \Bigg]. \tag{6.40}$$

We find the valence band splitting by taking the difference between the perturbations to the eigenvalues arising from H_{TMD+Fe}

$$E_{K\uparrow} - E_{K'\downarrow} = 2M_s^{Fe}\cos\theta(J - J^2\beta) \tag{6.41}$$

To confirm the validity of this approach, we can calculate corrections to the eigenvalues $E_{K\uparrow}$ and $E_{K'\downarrow}$ based on equations (6.37-6.40). We use J (Fig. 6.7b) and β calculated from the analysis in the main text for the 100% coverage case of WSe_2 and MoS_2. To determine α we first approximate the top and bottom valence bands at K and K' to be parabolic. We sum the expressions in Eq. 6.10 and 6.11 over **k'** points within $|K - \mathbf{k'}| < 0.16$, halfway between Γ and K. The weights $w(\mathbf{k'})$ are determined by comparing the fraction of orbital character at each **k'** that is Y_2^{+2} to the fraction of orbital character at K that is Y_2^{+2}. By taking the ratio of the sum over the top band and the sum over the bottom band we find the ratio $\frac{\alpha}{\beta}$ from which we can determine α, having already determined β from the fitting analysis in the main text. The DFT-PBE result for the magnetic moment of Fe is $3.1\mu_B$ so M_s^{Fe} and S are taken to be $\frac{3}{2}$. Using the same approximations as in the main text, $J = J_{KK} = J_{K'K'}$ and J can be removed form the second order sums, we plot the following expressions and compare to the DFT-PBE results for the eigenvalues.

$$E_{K\uparrow} = E_0 + JM_s^{Fe}\cos\theta + J^2\{[(M_s^{Fe})^2\cos^2\theta + \frac{1}{2}\sin^2\theta(S(S+1) - (M_s^{Fe})^2)]\alpha + [(M_s^{Fe})^2\sin^2\theta + \frac{1}{2}(S(S+1) - (M_s^{Fe})^2(\cos^2\theta + 1) - M_s^{Fe}\cos\theta]\beta\} \tag{6.42}$$

and

$$E_{K\uparrow} = E_0 - JM_s^{Fe}\cos\theta + J^2\{[(M_s^{Fe})^2\cos^2\theta + \frac{1}{2}\sin^2\theta(S(S+1) - (M_s^{Fe})^2)]\alpha + [(M_s^{Fe})^2\sin^2\theta + \frac{1}{2}(S(S+1) - (M_s^{Fe})^2(\cos^2\theta + 1) + M_s^{Fe}\cos\theta]\beta\}. \tag{6.43}$$

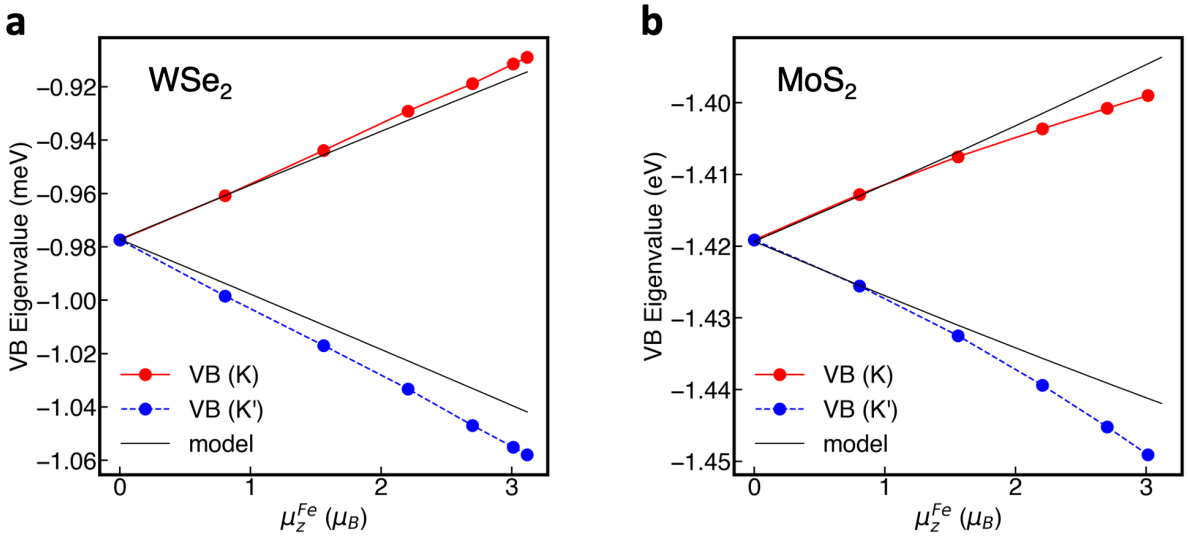


Figure 6.12: Comparison of the valence band eigenvalues of (a) WSe_2 and (b) MoS_2 calculated via DFT (red and blue) and calculated using Eq. 6.42 and 6.43 with the approximations outlined above. μ_z^{Fe} corresponds to $2M_s^{Fe}\cos\theta$

The fits between the model and the DFT-PBE results for the VB eigenvalues are qualitatively good. In particular, the slopes of the lines determined by the model are quite close to the slopes of the lines calculated via DFT-PBE, indicating that the parabolic approximation to the bands in order to determine α is relatively good.

Chapter 7

Exchange bias in a 2D metal-organic framework spin glass

This chapter is adapted from [145]. This work was done in collaboration with experimentalists in the Long group at UC Berkeley. In this dissertation, we summarize the experimentalists' findings then outline our theory contributions. We perform first-principles DFT calculations to determine the ground state magnetic ordering of the newly-discovered frustrated antiferromagnetic layered metal-organic framework (MOF) material $Mn_3(C_6S_6)$ which was synthesized by our experimental collaborators. We then calculat the band structure and density of states of this novel MOF for both its bulk and monolayer crystal structures. The calculated near-degeneracy of many of the magnetic orderings considered helps rationalize our experimental collaborators' findings that this MOF behaves as a spin glass at low temperatures.

7.1 Introduction

The discovery of conductive and magnetic two-dimensional (2D) materials is critical for the development of next generation spintronics devices. Coordination chemistry in particular represents a highly versatile, though underutilized, route toward the synthesis of such materials with designer lattices. Here, our experimental collaborators in the Long group at UC Berkeley report the synthesis of a conductive, layered 2D metal–organic kagomé lattice, $Mn_3(C_6S_6)$, using mild solution-phase chemistry. Strong geometric spin frustration in this system mediates spin freezing at low temperatures, which results in glassy magnetic dynamics consistent with a rare geometrically frustrated (topological) spin glass. Notably, they show that this geometric frustration engenders a large, tunable exchange bias of 1625 Oe in $Mn_3(C_6S_6)$, providing the first example of exchange bias in a coordination solid or a topological spin glass. Exchange bias is a critical component in a number of spintronics applications, but it is difficult to rationally tune, as it typically arises due to structural disorder. This work outlines a new strategy for engineering exchange bias systems using single-phase, crys-

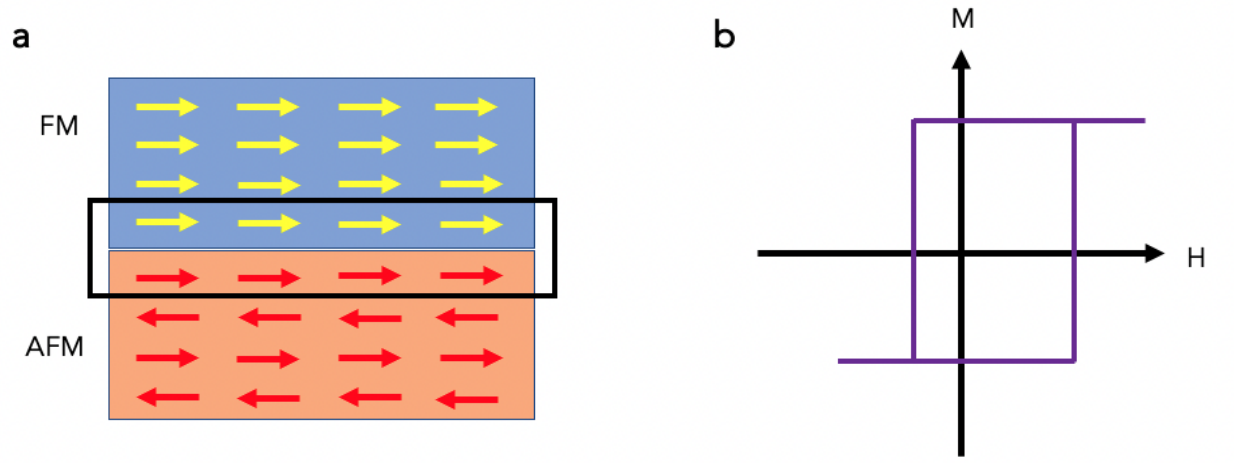


Figure 7.1: Illustration of exchange bias. (a) Schematic of FM/AFM interface in which exchange bias would be expected. (b) Schematic of a shifted hysteresis curve, indicating the presence of exchange bias.

talline lattices. More generally, these results demonstrate the potential utility of geometric frustration in the design of new nanoscale spintronic materials.

7.2 Exchange Bias

Exchange bias is a phenomenon that is generally associated with ferromagnetic (FM) and antiferromagnetic (AFM) interfaces (Figure 7.1a) [18]. Normally a FM material exhibits a hysteresis curve that is centered at 0, meaning that it does not prefer having its magnetic moments pointing in one or the other direction along its easy-axis. However, in proximity to an AFM material, the surface layer of magnetic moments of the AFM material can couple to those of the FM and generate a preferential orientation of the FM material's magnetic moments in one direction along its easy-axis. This phenomenon can be observed by measurement of the hysteresis curve of such a FM/AFM heterostructure. When exchange bias occurs, the center of the hysteresis curve shifts away from 0, which is the smoking gun that an exchange bias effect has occurred.

Because the applied field is not expected to flip the spins of the AFM material, exchange bias in FM/AFM heterostructures is unidirectional. Further, the magnitude of the exchange field, or the magnitude of the shift of the hysteresis curve, is generally fixed. Historical applications of exchange bias include production of permanent magnets and magnetic memory technology [18].

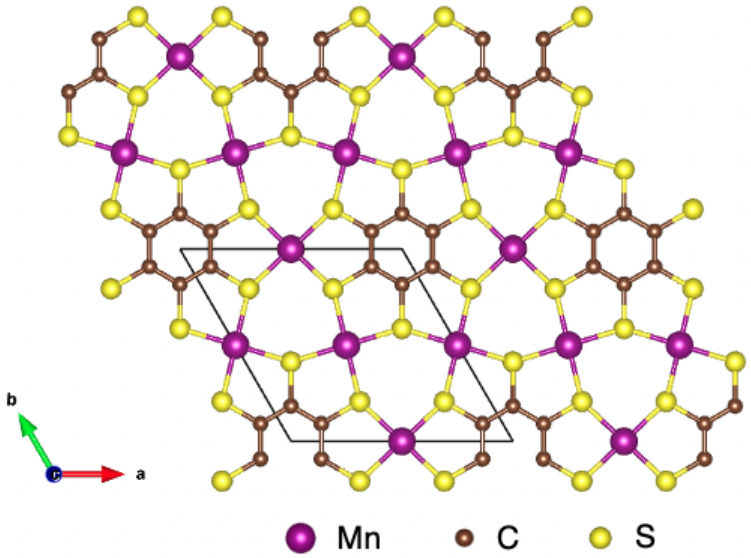


Figure 7.2: The crystal structure of a single layer of $Mn_3(C_6S_6)$.

For more modern applications, such as spintronics devices, tunable exchange bias is a desirable property that has proven challenging to realize.

7.3 Experimental Results

The experimentalists in the Long group at UC Berkeley synthesized a novel metal-organic framework material, $Mn_3(C_6S_6)$. Using synchrotron powder X-ray diffraction, the crystal structure was determined to be a layered structure. Each layer exhibits a kagomé lattice of Mn ions coordinated by cyclohexanehexathione (C_6S_6) linker ligands (Figure 7.2).

The magnetic susceptibility as a function of temperature was measured in order to study the magnetic ordering and perform a Curie-Weiss analysis. The susceptibility in the region above the critical temperature is expected to obey:

$$\chi = \frac{C}{T - \Theta_{CW}} \tag{7.1}$$

where χ is the molar magnetic susceptibility, C is the Curie constant, T is temperature, and Θ_{CW} is the Curie-Weiss temperature [69]. Projecting the trend in the inverse of the molar susceptibility versus temperature to the temperature axis, the intercept Θ_{CW} was found to be -268 K (Figure 7.3). Negative values of Θ_{CW} are characteristic of AFM materials [69]. Further, comparison of the critical temperature ($\sim$12 K) to Θ_{CW} revealed a Ramirez ratio

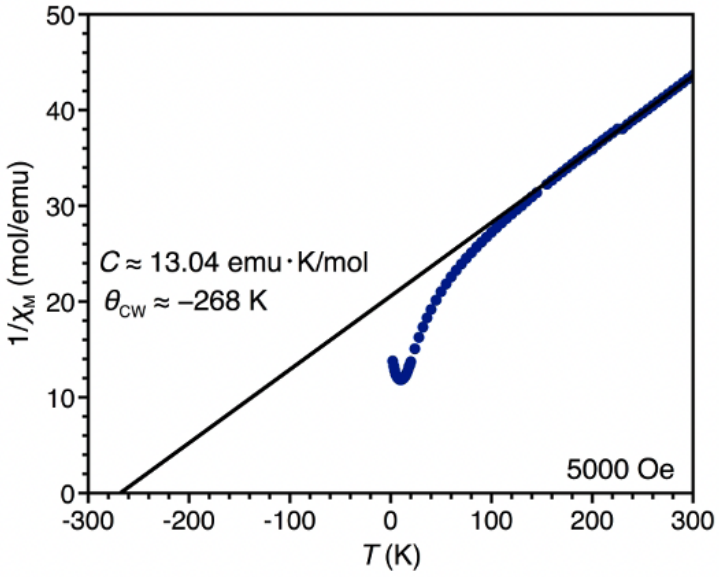


Figure 7.3: The inverse magnetic susceptibility of $Mn_3(C_6S_6)$ versus temperature.

$f = \frac{|\Theta_{CW}|}{T_N} \approx 22$. The Ramirez ratio is an indicator of spin frustration, meaning that the synthesized $Mn_3(C_6S_6)$ exhibits significant spin frustration and is likely a spin glass [146].

Variable-field magnetization data collected upon cooling with and without an applied field revealed that the hysteresis curves of $Mn_3(C_6S_6)$ exhibit an exchange bias. The center of the hysteresis curves shifts by 1625 Oe when field cooled with a 1 T applied field, with the shift moving in different directions depending on the orientation of the applied field (Figure 7.4).

This result is remarkable in that exchange bias is observed in a single-phase material, in the absence of a clear boundary between FM and AFM regions as is traditionally observed in cases of exchange bias.

7.4 First-principles calculations

In order to calculate the magnetic configuration and electronic structure of $Mn_3(C_6S_6)$, first-principles calculations of several candidate magnetic configurations are performed on monolayer $Mn_3(C_6S_6)$. Next, bulk calculations are performed with the magnetic configuration found to be most stable for the monolayer.

First-principles ionic and electronic structure calculations are performed using density functional theory with a plane-wave basis and projector augmented wave (PAW) potentials [61] as implemented by the Vienna *ab initio* simulation package (VASP) [62, 63]. All calculations are performed in the generalized gradient approximation as implemented by Perdew,

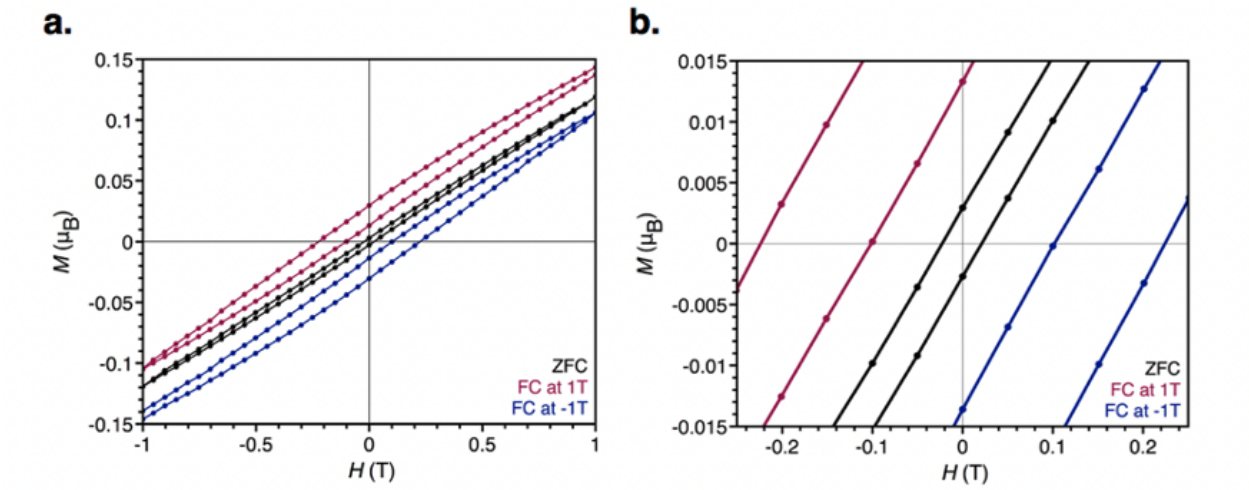


Figure 7.4: The hysteresis curves of $Mn_3(C_6S_6)$ when zero-field cooled (ZFC) and field cooled (FC) at ± 1 T. The center of the hysteresis curves shifts depending on the orientation of the applied field during cooling. (b) is a zoomed in version of the curves in (a) to make the shift more clearly visible.

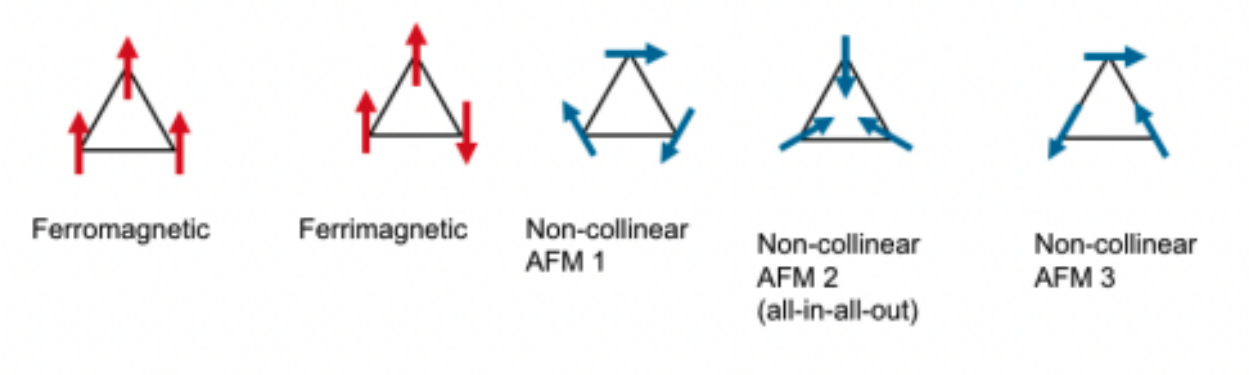


Figure 7.5: The five magnetic orderings considered for monolayer $Mn_3(C_6S_6)$.

Magnetic Configuration	Energy relative to most stable configuration (meV/atom)	Band Gap (eV)
Ferromagnetic	7.839	0.014
Ferrimagnetic	0.956	1.000
Non-collinear AFM 1	0.005	1.539
Non-collinear AFM 2 (all-in-all-out)	0.000	1.539
Non-collinear AFM 3	0.421	1.519

Table 7.1: The relative energies of different magnetic configurations for monolayer $Mn_3(C_6S_6)$.

Burke and Ernzerhof (PBE) [23], with the addition of a Hubbard U term (GGA+U) [28] to account for on-site localization on the Mn ions, using U = 4.0 eV. A planewave energy cut-off of 500 eV is used with a 10×10×1 Γ-centered k-point mesh. A 20 Å vacuum insertion is used to prevent interactions between monolayers. All forces are converged to < 1 meV/Å in the structural relaxations. For monolayer calculations, a 20 Å vacuum layer is inserted to prevent interactions between adjacent layers. In the calculated bulk crystal structure, individual layers are directly aligned along the c-axis and Grimme-D3 corrections are included to account for interlayer dispersion forces [37]. All forces are converged to < 1 meV/Å in the structural relaxations. Non-collinear spin polarized ionic relaxations, band structure, and density of states calculations are performed for all magnetic orderings considered for monolayers, and for the most stable conformation for the bulk structure, with spin-orbit coupling included.

Five magnetic configurations are studied for the monolayer, with the crystal structure relaxed independently for each magnetic configuration (Figure 7.5). The relative energies of each magnetic ordering are displayed in Table 7.1.

The FM magnetic ordering is significantly less stable than the ferrimagnetic and non-collinear AFM orderings, by ∼8 meV/atom. The non-collinear AFM magnetic orderings studied are nearly degenerate, with an energy difference per atom less than kT even at low temperature. This indicates that domains of different magnetic orderings that are nearly degenerate could exist in the ground state and supports the experimental observation of spin glassiness.

The band structure of the most stable non-collinear AFM ordering for monolayer $Mn_3(C_6S_6)$ (Figure 7.6) exhibits a direct band gap of ∼1.5 eV at the Γ point. The projected density of states (pDOS) shows that the VB edge has contributions from all three elements, indicating significant hybridization.

The band structure of bulk $Mn_3(C_6S_6)$ with an AA stacking pattern and the same non-collinear AFM magnetic ordering as that used in the monolayer electronic structure calcu-

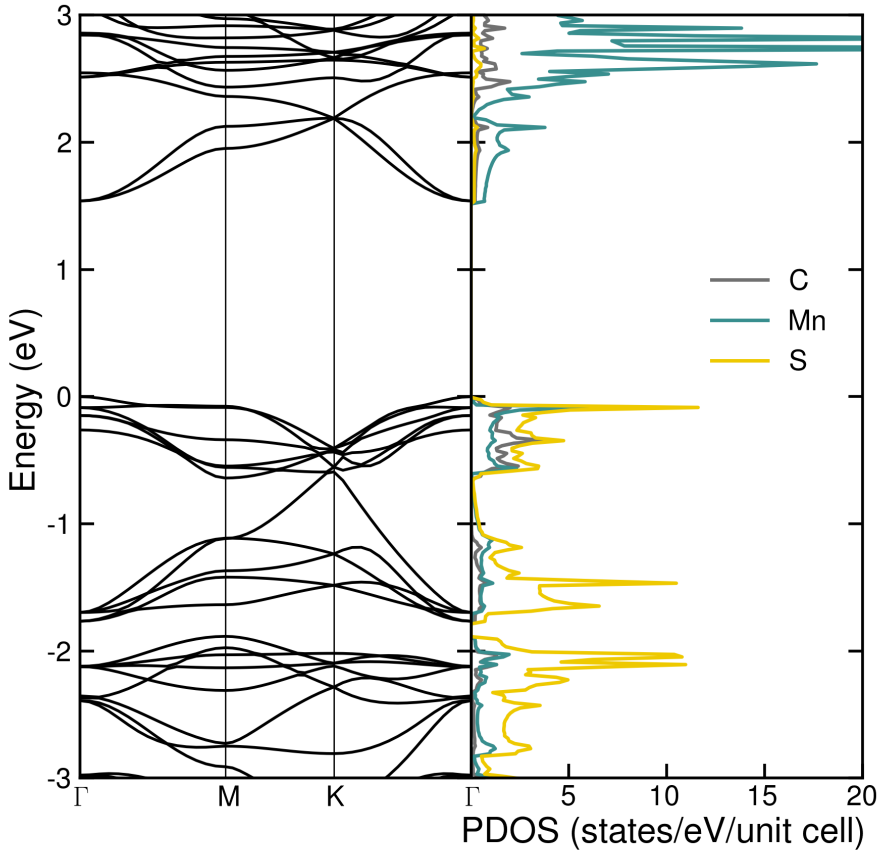


Figure 7.6: The band structure and element projected density of states for monolayer $Mn_3(C_6S_6)$ in the most stable AFM magnetic ordering.

lation (Figure 7.7) is similar to that of the monolayer, in that it also exhibits a direct band gap at the Γ point. The band gap, however, is reduced to ∼1 eV. The pDOS indicates that, while mixing of all three elements still occurs, the C and S contributions somewhat outweigh that of Mn.

7.5 Outlook

The combination of experimental and theory results in this study confirm that $Mn_3(C_6S_6)$ is a spin glass that exhibits a highly degenerate ground state. The observation of tunable exchange bias in a single-phase material is remarkable and indicates that geometric frustration of spins can be a driver of exchange bias. Indeed, this phenomenon has also been recently observed in another material with a frustrated kagomé lattice [147]. The mecha-

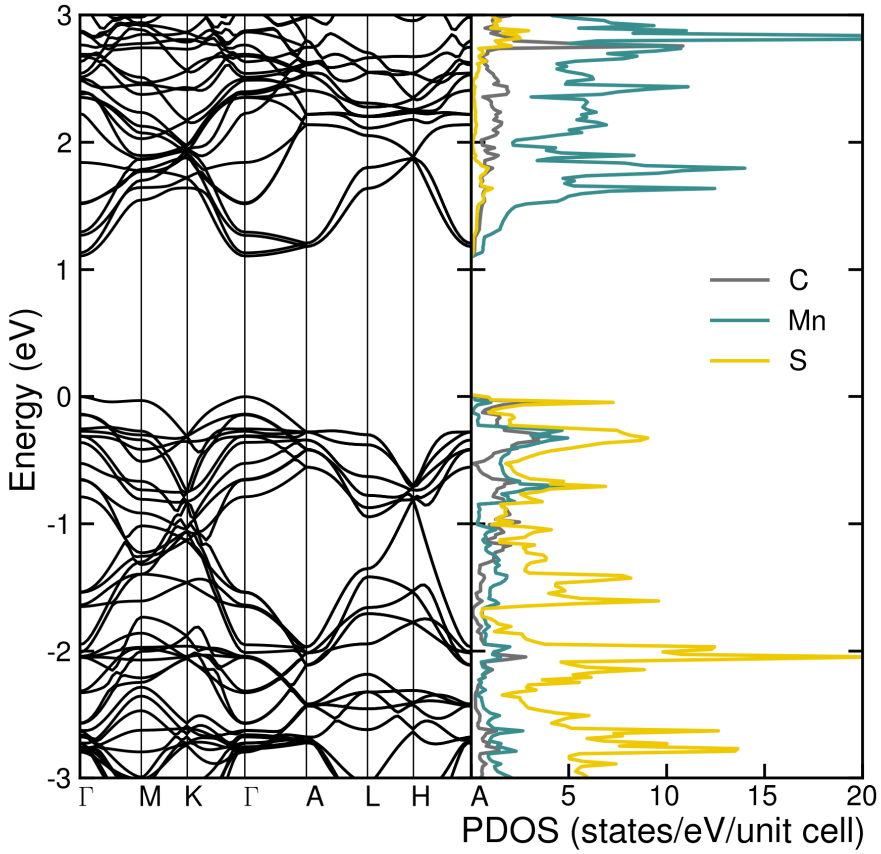


Figure 7.7: The band structure and element projected density of states for bulk $Mn_3(C_6S_6)$ in the most stable AFM magnetic ordering.

nism driving exchange bias in this class of materials is thought to be due to the creation of varying domains of different magnetic orderings when the material is cooled as the magnetic ground state ordering is highly degenerate. More study is needed, but the interplay between varying magnetic domains in frustrated AFM materials is an area of research ripe for further investigation for applications in novel memory devices.

Chapter 8

Conclusions and Outlook

In this dissertation we have used first-principles DFT calculations to study functional materials for applications in artificial photosynthesis and quantum information.

Our explorations of novel oxide and chalcogenide materials for photocatalysis applications have helped rationalize experimental observations and propose novel avenues for energy conversion and storage. In collaboration with experimentalists in the Gregoire group at Caltech, we have performed electronic structure and phase diagram calculations to shed light on the mechanism that may be driving high photovoltage in the novel photoanode material n-type $FeWO_4$. In collaboration with experimentalists in the Atwater group at Caltech, we have performed electronic structure calculations on a series of $MoS_{2(1-x)}Se_{2x}$ alloys in order to rationalize experimentally measured absolute band edge positions and shed light on the crystal structures that can be used for fine grained tuning of the band edges. We also explored the unexpected conduction band edge energy reduction in the case of small domains of $MoSe_2$ embedded in MoS_2. Our studies of Janus WSSe-ZnO heterostructures revealed that interfacial dipole effects can be harnessed to tune the absolute band edges of vdW heterostructures.

Our studies of materials hosting novel physics with quantum information applications have shed light on new methods for developing "Beyond Moore's Law" information technology. Our systematic study of valley splitting in TMDs by magnetic substrates revealed that this phenomenon can be understood in the context of a superexchange interaction occurring between the TMD's transition metal and the magnetic substrate's magnetic ions. Using these results we developed general design principles for designing heterostructures that can maximize valley splitting. We also performed calculations that set an upper bound on achievable valley splitting via magnetic oxide substrates. In collaboration with experimentalists in the Long group at UC Berkeley, we have performed a detailed analysis of the magnetic ordering of a novel 2D material that exhibits tunable exchange bias, with potential applications for spintronics technology. Several outstanding questions remain that offer exciting opportunities for future research.

We hypothesized that oxygen vacancies and electron polarons are responsible for the high photovoltage observed in n-type $FeWO_4$. A systematic study of the effect of oxygen vacancies

on the electronic structure of $FeWO_4$ would offer significant insight into the validity of this hypothesis. Further, comparison of these results to the electronic structure of $CuWO_4$ with oxygen vacancies, which are known to amplify the photoactivity of this material, would assist in determining if oxygen vacancies are a tool that can be leveraged in general in this class of materials for designing optimized photoanodes.

The dipole across the interface of small domains of $MoSe_2$ in MoS_2 is suspected to be responsible for the consistent reduction of the conduction band edge energy and the confinement of the CB state in the $MoSe_2$ region. This hypothesis could be further validated by additional study of these interfaces, via, for example, different geometries (e.g. stripes of $MoSe_2$ instead of triangles) or different chalcogens (e.g. an interface of MoS_2 and $MoTe_2$).

The generalizability of using strain to manipulate band edges in vdW heterostructures of materials with out-of-plane interfacial dipoles should be validated by study of other combinations of 2D materials. An obvious starting point would be to study two different Janus TMDs, such as MoSSe and WSSe. Further, study of this effect in the presence of defects, such as chalcogen vacancies would be valuable, as edge sites and chalcogen vacancies are known to be the primary catalytically active sites for HER and CO_2RR.

To identify magnetic substrates that can produce large valley splitting in monolayer TMDs *and* support in-situ switchable valley polarization, identification of a multiferroic substrate with strong magneto-electric coupling that meets the general design principles elucidated here would be invaluable. A high-throughput search of known multiferroics for materials with good lattice parameter matching and out-of-plane magnetic moments would be an excellent next step in the development of this technology.

By leveraging first-principles DFT calculations, a broad array of questions in condensed matter physics can be answered, ranging from the design of novel materials to the rationalization of experimental results. The methodology used in this dissertation is broadly applicable towards solving a wide range of studies with relevance to future energy and information technologies.

Bibliography

[1] L. Zhou *et al.* Bi-Containing n-$FeWO_4$ Thin Films Provide the Largest Photovoltage and Highest Stability for a Sub-2 eV Band Gap Photoanode. *ACS Energy Letters* **3**, 2769 (2018). eprint: https://doi.org/10.1021/acsenergylett.8b01514.

[2] P. Lianos. Review of recent trends in photoelectrocatalytic conversion of solar energy to electricity and hydrogen. *Applied Catalysis B: Environmental* **210**, 235 (2017). eprint: https://doi.org/10.1016/j.apcatb.2017.03.067.

[3] Z. Mei, Y. Li, X. Yang, W. Ren, S. Tong, N. Zhang, W. Zhao, Y. Lin, and F. Pan. Tuning nanosheet Fe2O3 photoanodes with C3N4 and p-type CoOx decoration for efficient and stable water splitting. *Catalysis Science and Technology* **8**, 3144 (2018). eprint: http://dx.doi.org/10.1039/C8CY00729B.

[4] J. K. Cooper, S. E. Reyes-Lillo, L. H. Hess, C.-M. Jiang, J. B. Neaton, and I. D. Sharp. Physical Origins of the Transient Absorption Spectra and Dynamics in Thin-Film Semiconductors: The Case of BiVO4. *The Journal of Physical Chemistry C* **122**, 20642 (2018). eprint: https://doi.org/10.1021/acs.jpcc.8b06645.

[5] K. S. Novoselov, A. K. Geim, S. V. Morozov, D. Jiang, Y. Zhang, S. V. Dubonos, I. V. Grigorieva, and A. A. Firsov. Electric Field Effect in Atomically Thin Carbon Films. *Science* **306**, 666 (2004). eprint: https://www.science.org/doi/pdf/10.1126/science.1102896.

[6] A. Geim and I. Grigorieva. Van der Waals heterostructures. *Nature* **499**, 419 (2013). eprint: https://doi.org/10.1038/nature12385.

[7] Y. Yu *et al.* Gate-tunable phase transitions in thin flakes of 1T-TaS2. *Nature Nanotechnology* **10**, 270 (2015). eprint: https://doi.org/10.1038/nnano.2014.323.

[8] K. S. Novoselov, A. K. Geim, S. V. Morozov, D. Jiang, M. I. Katsnelson, I. V. Grigorieva, S. V. Dubonos, and A. A. Firsov. Two-dimensional gas of massless Dirac fermions in graphene. *Nature* **438**, 197 (2005). eprint: https://doi.org/10.1038/nature04233.

[9] K. F. Mak, C. Lee, J. Hone, J. Shan, and T. F. Heinz. Atomically Thin MoS_2: A New Direct-Gap Semiconductor. *Physical Review Letters* **105**, 136805 (2010). eprint: https://link.aps.org/doi/10.1103/PhysRevLett.105.136805.

[10] H. Wang, Y. Zhao, Y. Xie, X. Ma, and X. Zhang. Recent progress in synthesis of two-dimensional hexagonal boron nitride. *Journal of Semiconductors* **38**, 031003 (2017). eprint: https://doi.org/10.1088/1674-4926/38/3/031003.

[11] D. Y. Qiu, F. H. da Jornada, and S. G. Louie. Optical Spectrum of MoS_2: Many-Body Effects and Diversity of Exciton States. *Physical Review Letters* **111**, 216805 (2013). eprint: https://link.aps.org/doi/10.1103/PhysRevLett.111.216805.

[12] J. Kang, S. Tongay, J. Zhou, J. Li, and J. Wu. Band offsets and heterostructures of two-dimensional semiconductors. *Applied Physics Letters* **102**, 012111 (2013). eprint: https://doi.org/10.1063/1.4774090.

[13] Y. Liang, J. Li, H. Jin, B. Huang, and Y. Dai. Photoexcitation Dynamics in Janus-MoSSe/WSe2 Heterobilayers: Ab Initio Time-Domain Study. *The Journal of Physical Chemistry Letters* **9**, 2797 (2018). eprint: https://doi.org/10.1021/acs.jpclett.8b00903.

[14] A. C. Riis-Jensen, M. Pandey, and K. S. Thygesen. Efficient Charge Separation in 2D Janus van der Waals Structures with Built-in Electric Fields and Intrinsic p-n Doping. *The Journal of Physical Chemistry C* **122**, 24520 (2018). eprint: https://doi.org/10.1021/acs.jpcc.8b05792.

[15] C. Long, Y. Dai, Z.-R. Gong, and H. Jin. Robust type-II band alignment in Janus-MoSSe bilayer with extremely long carrier lifetime induced by the intrinsic electric field. *Physical Review B* **99**, 115316 (2019). eprint: https://link.aps.org/doi/10.1103/PhysRevB.99.115316.

[16] K. F. Mak, K. He, J. Shan, and T. F. Heinz. Control of valley polarization in monolayer MoS_2 by optical helicity. *Nature Nanotechnology* **7**, 494 (2012). eprint: https://www.nature.com/articles/nnano.2012.96.

[17] Y. Li *et al.* Valley Splitting and Polarization by the Zeeman Effect in Monolayer $MoSe_2$. *Physical Review Letters* **113**, 266804 (2014). eprint: https://link.aps.org/doi/10.1103/PhysRevLett.113.266804.

[18] J. Nogués and I. K. Schuller. Exchange Bias. *Journal of Magnetism and Magnetic Materials* **192**, 203 (1999). eprint: https://doi.org/10.1016/S0304-8853(98)00266-2.

[19] M. L. Cohen and S. G. Louie. *Fundamentals of Condensed Matter Physics*. Cambridge University Press, (2016).

[20] P. Hohenberg and W. Kohn. Inhomogeneous Electron Gas. *Physical Review* **136**, B864 (1964). eprint: https://link.aps.org/doi/10.1103/PhysRev.136.B864.

[21] W. Kohn and L. J. Sham. Self-Consistent Equations Including Exchange and Correlation Effects. *Physical Review* **140**, A1133 (1965). eprint: https://link.aps.org/doi/10.1103/PhysRev.140.A1133.

[22] J. P. Perdew. Density-functional approximation for the correlation energy of the inhomogeneous electron gas. *Physical Review B* **33**, 8822 (1986). eprint: `https://link.aps.org/doi/10.1103/PhysRevB.33.8822`.

[23] J. P. Perdew, K. Burke, and M. Ernzerhof. Generalized Gradient Approximation Made Simple. *Physical Review Letters* **77**, 3865 (1996). eprint: `https://link.aps.org/doi/10.1103/PhysRevLett.77.3865`.

[24] J. P. Perdew, R. G. Parr, M. Levy, and J. L. Balduz. Density-Functional Theory for Fractional Particle Number: Derivative Discontinuities of the Energy. *Physical Review Letters* **49**, 1691 (1982). eprint: `https://link.aps.org/doi/10.1103/PhysRevLett.49.1691`.

[25] P. Mori-Sánchez and A. J. Cohen. The derivative discontinuity of the exchange-correlation functional. *Physical Chemistry Chemical Physics* **16**, 14378 (2014). eprint: `http://dx.doi.org/10.1039/C4CP01170H`.

[26] D. J. Griffiths. *Introduction to Quantum Mechanics (2nd Edition)*. 2nd. Pearson Prentice Hall, (2004). ISBN: 0131118927.

[27] J. Hubbard and B. H. Flowers. Electron correlations in narrow energy bands. *Proceedings of the Royal Society of London. Series A. Mathematical and Physical Sciences* **276**, 238 (1963). eprint: `https://royalsocietypublishing.org/doi/pdf/10.1098/rspa.1963.0204`.

[28] S. L. Dudarev, G. A. Botton, S. Y. Savrasov, C. J. Humphreys, and A. P. Sutton. Electron-energy-loss spectra and the structural stability of nickel oxide: An LSDA+U study. *Physical Review B* **57**, 1505 (1998). eprint: `https://link.aps.org/doi/10.1103/PhysRevB.57.1505`.

[29] M. Cococcioni and S. de Gironcoli. Linear response approach to the calculation of the effective interaction parameters in the LDA + U method. *Physical Review B* **71**, 035105 (2005). eprint: `https://link.aps.org/doi/10.1103/PhysRevB.71.035105`.

[30] M. Yu, S. Yang, C. Wu, and N. Marom. Machine learning the Hubbard U parameter in DFT+U using Bayesian optimization. *npj Computational Materials* **6** (2020). eprint: `https://doi.org/10.1038/s41524-020-00446-9`.

[31] A. D. Becke. A new mixing of Hartree-Fock and local density functional theories. *The Journal of Chemical Physics* **98**, 1372 (1993). eprint: `https://doi.org/10.1063/1.464304`.

[32] P. Borlido, T. Aull, A. W. Huran, F. Tran, M. A. L. Marques, and S. Botti. Large-Scale Benchmark of Exchange-Correlation Functionals for the Determination of Electronic Band Gaps of Solids. *Journal of Chemical Theory and Computation* **15**, 5069 (2019). eprint: `https://doi.org/10.1021/acs.jctc.9b00322`.

[33] J. Heyd, G. E. Scuseria, and M. Ernzerhof. Hybrid functionals based on a screened Coulomb potential. *The Journal of Chemical Physics* **118**, 8207 (2003). eprint: `https://doi.org/10.1063/1.1564060`.

[34] A. V. Krukau, O. A. Vydrov, A. F. Izmaylov, and G. E. Scuseria. Influence of the exchange screening parameter on the performance of screened hybrid functionals. *The Journal of Chemical Physics* **125**, 224106 (2006). eprint: https://doi.org/10.1063/1.2404663.

[35] G. F. von Rudorff, R. Jakobsen, K. M. Rosso, and J. Blumberger. Improving the Performance of Hybrid Functional-Based Molecular Dynamics Simulation through Screening of Hartree-Fock Exchange Forces. *Journal of Chemical Theory and Computation* **13**, 2178 (2017). eprint: https://doi.org/10.1021/acs.jctc.6b01121.

[36] K. Berland, V. R. Cooper, K. Lee, E. Schröder, T. Thonhauser, P. Hyldgaard, and B. I. Lundqvist. van der Waals forces in density functional theory: a review of the vdW-DF method. *Reports on Progress in Physics* **78**, 066501 (2015). eprint: https://iopscience.iop.org/article/10.1088/0034-4885/78/6/066501.

[37] S. Grimme, J. Antony, S. Ehrlich, and H. Krieg. A consistent and accurate ab initio parametrization of density functional dispersion correction (DFT-D) for the 94 elements H-Pu. *The Journal of Chemical Physics* **132**, 154104 (2010). eprint: https://doi.org/10.1063/1.3382344.

[38] S. Grimme, S. Ehrlich, and L. Goerigk. Effect of the damping function in dispersion corrected density functional theory. *Journal of Computational Chemistry* **32**, 1456 (2011). eprint: https://onlinelibrary.wiley.com/doi/pdf/10.1002/jcc.21759.

[39] H. Rydberg, B. I. Lundqvist, D. C. Langreth, and M. Dion. Tractable nonlocal correlation density functionals for flat surfaces and slabs. *Physical Review B* **62**, 6997 (2000). eprint: https://link.aps.org/doi/10.1103/PhysRevB.62.6997.

[40] M. Dion, H. Rydberg, E. Schröder, D. C. Langreth, and B. I. Lundqvist. Van der Waals Density Functional for General Geometries. *Physical Review Letters* **92**, 246401 (2004). eprint: https://link.aps.org/doi/10.1103/PhysRevLett.92.246401.

[41] S. A. Tawfik, T. Gould, C. Stampfl, and M. J. Ford. Evaluation of van der Waals density functionals for layered materials. *Physical Review Materials* **2**, 034005 (2018). eprint: https://link.aps.org/doi/10.1103/PhysRevMaterials.2.034005.

[42] L. Hedin. New Method for Calculating the One-Particle Green's Function with Application to the Electron-Gas Problem. *Physical Review* **139**, A796 (1965). eprint: https://link.aps.org/doi/10.1103/PhysRev.139.A796.

[43] M. S. Hybertsen and S. G. Louie. Electron correlation in semiconductors and insulators: Band gaps and quasiparticle energies. *Physical Review B* **34**, 5390 (1986). eprint: https://link.aps.org/doi/10.1103/PhysRevB.34.5390.

[44] G. Onida, L. Reining, and A. Rubio. Electronic excitations: density-functional versus many-body Green's-function approaches. *Reviews of Modern Physics* **74**, 601 (2002). eprint: https://link.aps.org/doi/10.1103/RevModPhys.74.601.

[45] M. Rohlfing and S. G. Louie. Electron-hole excitations and optical spectra from first principles. *Physical Review B* **62**, 4927 (2000). eprint: https://link.aps.org/doi/10.1103/PhysRevB.62.4927.

[46] P. G. Moses, M. Miao, Q. Yan, and C. G. Van de Walle. Hybrid functional investigations of band gaps and band alignments for AlN, GaN, InN, and InGaN. *The Journal of Chemical Physics* **134**, 084703 (2011). eprint: https://doi.org/10.1063/1.3548872.

[47] M. H. Richter *et al.* Band Edge Energy Tuning through Electronic Character Hybridization in Ternary Metal Vanadates. *Chemistry of Materials* **33**, 7242 (2021). eprint: https://doi.org/10.1021/acs.chemmater.1c01415.

[48] J. P. Perdew and M. Levy. Physical Content of the Exact Kohn-Sham Orbital Energies: Band Gaps and Derivative Discontinuities. *Physical Review Letters* **51**, 1884 (1983). eprint: https://link.aps.org/doi/10.1103/PhysRevLett.51.1884.

[49] A. Castellanos-Gomez, R. Roldán, E. Cappelluti, M. Buscema, F. Guinea, H. S. J. van der Zant, and G. A. Steele. Local Strain Engineering in Atomically Thin MoS2. *Nano Letters* **13**, 5361 (2013). eprint: https://doi.org/10.1021/nl402875m.

[50] D. Lloyd, X. Liu, J. W. Christopher, L. Cantley, A. Wadehra, B. L. Kim, B. B. Goldberg, A. K. Swan, and J. S. Bunch. Band Gap Engineering with Ultralarge Biaxial Strains in Suspended Monolayer MoS2. *Nano Letters* **16**, 5836 (2016). eprint: https://doi.org/10.1021/acs.nanolett.6b02615.

[51] C. V. Nguyen, V. V. Ilyasov, H. V. Nguyen, and H. N. Nguyen. Band gap and electronic properties of molybdenum disulphide under strain engineering: density functional theory calculations. *Molecular Simulation* **43**, 86 (2016). eprint: https://doi.org/10.1080/08927022.2016.1233549.

[52] X. Cheng, Y. Li, J. Shang, C. Hu, Y. Ren, M. Liu, and Z. Qi. Thickness-dependent phase transition and optical behavior of MoS2 films under high pressure. *Nano Research* **11**, 855 (2017). eprint: https://doi.org/10.1007/s12274-017-1696-y.

[53] Z. Peng, X. Chen, Y. Fan, D. J. Srolovitz, and D. Lei. Strain engineering of 2D semiconductors and graphene: from strain fields to band-structure tuning and photonic applications. *Light: Science and Applications* **9** (2020). eprint: https://doi.org/10.1038/s41377-020-00421-5.

[54] F. Bloch. Über die Quantenmechanik der Elektronen in Kristallgittern. *Zeitschrift für Physik* **52**, 555 (1929). eprint: https://doi.org/10.1007/BF01339455.

[55] D. R. Hamann, M. Schlüter, and C. Chiang. Norm-Conserving Pseudopotentials. *Physical Review Letters* **43**, 1494 (1979). eprint: https://link.aps.org/doi/10.1103/PhysRevLett.43.1494.

[56] P. E. Blöchl. Projector augmented-wave method. *Physical Review B* **50**, 17953 (1994). eprint: https://link.aps.org/doi/10.1103/PhysRevB.50.17953.

[57] S. Steiner, S. Khmelevskyi, M. Marsmann, and G. Kresse. Calculation of the magnetic anisotropy with projected-augmented-wave methodology and the case study of disordered $Fe_{1-x}Co_x$ alloys. *Physical Review B* **93**, 224425 (2016). eprint: `https://link.aps.org/doi/10.1103/PhysRevB.93.224425`.

[58] T. Björkman. Testing several recent van der Waals density functionals for layered structures. *The Journal of Chemical Physics* **141**, 074708 (2014). eprint: `https://doi.org/10.1063/1.4893329`.

[59] F. Tran, L. Kalantari, B. Traoré, X. Rocquefelte, and P. Blaha. Nonlocal van der Waals functionals for solids: Choosing an appropriate one. *Physical Review Materials* **3**, 063602 (2019). eprint: `https://link.aps.org/doi/10.1103/PhysRevMaterials.3.063602`.

[60] I. Hamada. van der Waals density functional made accurate. *Physical Review B* **89**, 121103 (2014). eprint: `https://link.aps.org/doi/10.1103/PhysRevB.89.121103`.

[61] G. Kresse and D. Joubert. From ultrasoft pseudopotentials to the projector augmented-wave method. *Physical Review B* **59**, 1758 (1999). eprint: `https://link.aps.org/doi/10.1103/PhysRevB.59.1758`.

[62] G. Kresse and J. Furthmüller. Efficiency of ab-initio total energy calculations for metals and semiconductors using a plane-wave basis set. *Computational Materials Science* **6**, 15 (1996). eprint: `https://www.sciencedirect.com/science/article/pii/0927025696000080`.

[63] G. Kresse and J. Furthmüller. Efficient iterative schemes for ab initio total-energy calculations using a plane-wave basis set. *Physical Review B* **54**, 11169 (1996). eprint: `https://link.aps.org/doi/10.1103/PhysRevB.54.11169`.

[64] R. G. Dickinson and L. Pauling. The crystal structure of molybdenite. *Journal of the American Chemical Society* **45**, 1466 (1923). eprint: `https://pubs.acs.org/doi/10.1021/ja01659a020`.

[65] N. E. Singh-Miller and N. Marzari. Surface energies, work functions, and surface relaxations of low-index metallic surfaces from first principles. *Physical Review B* **80**, 235407 (2009). eprint: `https://link.aps.org/doi/10.1103/PhysRevB.80.235407`.

[66] V. Stevanović, S. Lany, D. S. Ginley, W. Tumas, and A. Zunger. Assessing capability of semiconductors to split water using ionization potentials and electron affinities only. *Physical Chemistry Chemical Physics* **16**, 3706 (2014). eprint: `http://dx.doi.org/10.1039/C3CP54589J`.

[67] J. Neugebauer and M. Scheffler. Adsorbate-substrate and adsorbate-adsorbate interactions of Na and K adlayers on Al(111). *Physical Review B* **46**, 16067 (1992). eprint: `https://link.aps.org/doi/10.1103/PhysRevB.46.16067`.

[68] S. De Waele, K. Lejaeghere, M. Sluydts, and S. Cottenier. Error estimates for density-functional theory predictions of surface energy and work function. *Physical Review B* **94**, 235418 (2016). eprint: https://link.aps.org/doi/10.1103/PhysRevB.94.235418.

[69] C. Kittel. *Introduction to solid state physics*. 8th ed. John Wiley & Sons, (2004).

[70] S. Baroni, S. de Gironcoli, A. Dal Corso, and P. Giannozzi. Phonons and related crystal properties from density-functional perturbation theory. *Reviews of Modern Physics* **73**, 515 (2001). eprint: https://link.aps.org/doi/10.1103/RevModPhys.73.515.

[71] A. Togo and I. Tanaka. First principles phonon calculations in materials science. *Scripta Materialia* **108**, 1 (2015). eprint: https://www.sciencedirect.com/science/article/pii/S1359646215003127.

[72] A. K. Singh, K. Mathew, H. L. Zhuang, and R. G. Hennig. Computational Screening of 2D Materials for Photocatalysis. *The Journal of Physical Chemistry Letters* **6**, 1087 (2015). eprint: https://doi.org/10.1021/jz502646d.

[73] K. Sayama, A. Nomura, Z. Zou, R. Abe, Y. Abe, and H. Arakawa. Photoelectrochemical decomposition of water on nanocrystalline BiVO4 film electrodes under visible light. *Chemical Communications*, 2908 (2003). eprint: http://dx.doi.org/10.1039/B310428A.

[74] K. R. Tolod, S. Hernández, and N. Russo. Recent Advances in the $BiVO_4$ Photocatalyst for Sun-Driven Water Oxidation: Top-Performing Photoanodes and Scale-Up Challenges. *Catalysts* **7** (2017). eprint: https://www.mdpi.com/2073-4344/7/1/13.

[75] T. W. Kim, Y. Ping, G. A. Galli, and K.-S. Choi. Simultaneous enhancements in photon absorption and charge transport of bismuth vanadate photoanodes for solar water splitting. *Nature Communications* **6** (2015). eprint: https://doi.org/10.1038/ncomms9769.

[76] M. Kölbach, I. J. Pereira, K. Harbauer, P. Plate, K. Höflich, S. P. Berglund, D. Friedrich, R. van de Krol, and F. F. Abdi. Revealing the Performance-Limiting Factors in α-SnWO4 Photoanodes for Solar Water Splitting. *Chemistry of Materials* **30**, 8322 (2018). eprint: https://doi.org/10.1021/acs.chemmater.8b03883.

[77] J. C. Hill and K.-S. Choi. Synthesis and characterization of high surface area CuWO4 and Bi2WO6 electrodes for use as photoanodes for solar water oxidation. *Journal of Materials Chemistry A* **1**, 5006 (2013). eprint: http://dx.doi.org/10.1039/C3TA10245A.

[78] D. K. Lee, D. Lee, M. A. Lumley, and K.-S. Choi. Progress on ternary oxide-based photoanodes for use in photoelectrochemical cells for solar water splitting. *Chemical Society Reviews* **48**, 2126 (2019). eprint: http://dx.doi.org/10.1039/C8CS00761F.

[79] K. Sieber, K. Kourtakis, R. Kershaw, K. Dwight, and A. Wold. Preparation and photoelectronic properties of FeWO4. *Materials Research Bulletin* **17**, 721 (1982). eprint: https://doi.org/10.1016/0025-5408(82)90021-6.

[80] L. Kronik and Y. Shapira. Surface photovoltage phenomena: theory, experiment, and applications. *Surface Science Reports* **37**, 1 (1999). eprint: https://doi.org/10.1016/S0167-5729(99)00002-3.

[81] J. M. Gregoire, C. Xiang, X. Liu, M. Marcin, and J. Jin. Scanning droplet cell for high throughput electrochemical and photoelectrochemical measurements. *Review of Scientific Instruments* **84**, 024102 (2013). eprint: https://doi.org/10.1063/1.4790419.

[82] K. A. Persson. Materials Data on FeWO4 (SG:13) by Materials Project. *The Materials Project* (2014).

[83] A. Jain *et al.* Commentary: The Materials Project: A materials genome approach to accelerating materials innovation. *APL Materials* **1**, 011002 (2013). eprint: https://doi.org/10.1063/1.4812323.

[84] S. P. Ong, W. D. Richards, A. Jain, G. Hautier, M. Kocher, S. Cholia, D. Gunter, V. L. Chevrier, K. A. Persson, and G. Ceder. Python Materials Genomics (pymatgen): A robust, open-source python library for materials analysis. *Computational Materials Science* **68**, 314 (2013). eprint: https://www.sciencedirect.com/science/article/pii/S0927025612006295.

[85] S. P. Ong, A. Jain, G. Hautier, B. Kang, and G. Ceder. Thermal stabilities of delithiated olivine MPO4 (M=Fe, Mn) cathodes investigated using first principles calculations. *Electrochemistry Communications* **12**, 427 (2010). eprint: https://www.sciencedirect.com/science/article/pii/S1388248110000123.

[86] M. Chase. *NIST-JANAF Thermochemical Tables, 4th Edition.* en. American Institute of Physics, -1, (1998).

[87] K. Hoang. Polaron formation, native defects, and electronic conduction in metal tungstates. *Physical Review Materials* **1**, 024603 (2017). eprint: https://link.aps.org/doi/10.1103/PhysRevMaterials.1.024603.

[88] R. Fernández-Climent, S. Giménez, and M. García-Tecedor. The role of oxygen vacancies in water splitting photoanodes. *Sustainable Energy Fuels* **4**, 5916 (2020). eprint: http://dx.doi.org/10.1039/D0SE01305F.

[89] Y.-R. Lin *et al.* Band Edge Tailoring in Few-Layer Two-Dimensional Molybdenum Sulfide/Selenide Alloys. *The Journal of Physical Chemistry C* **124**, 22893 (2020). eprint: https://doi.org/10.1021/acs.jpcc.0c04719.

[90] H. Wang, C. Tsai, D. Kong, K. Chan, F. Abild-Pedersen, J. K. Nørskov, and Y. Cui. Transition-metal doped edge sites in vertically aligned MoS2 catalysts for enhanced hydrogen evolution. *Nano Research* **8**, 566 (2015). eprint: https://doi.org/10.1007/s12274-014-0677-7.

[91] G. Li *et al.* All The Catalytic Active Sites of MoS2 for Hydrogen Evolution. *Journal of the American Chemical Society* **138**, 16632 (2016). eprint: https://doi.org/10.1021/jacs.6b05940.

[92] M. Asadi *et al.* Robust carbon dioxide reduction on molybdenum disulphide edges. *Nature Communications* **5** (2014). eprint: https://doi.org/10.1038/ncomms5470.

[93] H.-P. Komsa and A. V. Krasheninnikov. Two-Dimensional Transition Metal Dichalcogenide Alloys: Stability and Electronic Properties. *The Journal of Physical Chemistry Letters* **3**, 3652 (2012). eprint: https://doi.org/10.1021/jz301673x.

[94] H. Terrones, F. López-Urías, and M. Terrones. Novel hetero-layered materials with tunable direct band gaps by sandwiching different metal disulfides and diselenides. *Scientific Reports* **3**, 1549 (2013). eprint: https://doi.org/10.1038/srep01549.

[95] T. Böker, R. Severin, A. Müller, C. Janowitz, R. Manzke, D. Voß, P. Krüger, A. Mazur, and J. Pollmann. Band structure of MoS_2, $MoSe_2$, and $\alpha - MoTe_2$: Angle-resolved photoelectron spectroscopy and ab initio calculations. *Physical Review B* **64**, 235305 (2001). eprint: https://link.aps.org/doi/10.1103/PhysRevB.64.235305.

[96] J. Kang, S. Tongay, J. Li, and J. Wu. Monolayer semiconducting transition metal dichalcogenide alloys: Stability and band bowing. *Journal of Applied Physics* **113**, 143703 (2013). eprint: https://doi.org/10.1063/1.4799126.

[97] A. K. Singh, J. H. Montoya, J. M. Gregoire, and K. A. Persson. Robust and synthesizable photocatalysts for CO2 reduction: a data-driven materials discovery. *Nature Communications* **10** (2019). eprint: https://doi.org/10.1038/s41467-019-08356-1.

[98] S. Yang, D. Prendergast, and J. B. Neaton. Tuning Semiconductor Band Edge Energies for Solar Photocatalysis via Surface Ligand Passivation. *Nano Letters* **12**, 383 (2012). eprint: https://doi.org/10.1021/nl203669k.

[99] J.-Q. Dai, X.-W. Wang, and T.-F. Cao. Large Band Offset in Monolayer MoS2 on Oppositely Polarized BiFeO3(0001) Polar Surfaces. *The Journal of Physical Chemistry C* **123**, 3039 (2019). eprint: https://doi.org/10.1021/acs.jpcc.8b12207.

[100] Q.-F. Yao, J. Cai, W.-Y. Tong, S.-J. Gong, J.-Q. Wang, X. Wan, C.-G. Duan, and J. H. Chu. Manipulation of the large Rashba spin splitting in polar two-dimensional transition-metal dichalcogenides. *Physical Review B* **95**, 165401 (2017). eprint: https://link.aps.org/doi/10.1103/PhysRevB.95.165401.

[101] A.-Y. Lu *et al.* Janus monolayers of transition metal dichalcogenides. *Nature Nanotechnology* **12**, 744 (2017). eprint: https://doi.org/10.1038/nnano.2017.100.

[102] J. Zhang *et al.* Janus Monolayer Transition-Metal Dichalcogenides. *ACS Nano* **11**, 8192 (2017). eprint: https://doi.org/10.1021/acsnano.7b03186.

[103] Y. C. Cheng, Z. Y. Zhu, M. Tahir, and U. Schwingenschlögl. Spin-orbit induced spin splittings in polar transition metal dichalcogenide monolayers. *Europhysics Letters* **102**, 57001 (2013). eprint: https://doi.org/10.1209/0295-5075/102/57001.

[104] L. Dong, J. Lou, and V. B. Shenoy. Large In-Plane and Vertical Piezoelectricity in Janus Transition Metal Dichalchogenides. *ACS Nano* **11**, 8242 (2017). eprint: https://doi.org/10.1021/acsnano.7b03313.

[105] Z. Zhou, X. Niu, Y. Zhang, and J. Wang. Janus MoSSe/WSeTe heterostructures: a direct Z-scheme photocatalyst for hydrogen evolution. *Journal of Materials Chemistry A* **7**, 21835 (2019). eprint: http://dx.doi.org/10.1039/C9TA06407A.

[106] C. Tusche, H. L. Meyerheim, and J. Kirschner. Observation of Depolarized ZnO(0001) Monolayers: Formation of Unreconstructed Planar Sheets. *Physical Review Letters* **99**, 026102 (2007). eprint: https://link.aps.org/doi/10.1103/PhysRevLett.99.026102.

[107] J. Yuhara, D. Kato, T. Matsui, and S. Mizuno. Structure of a zinc oxide ultra-thin film on Rh(100). *The Journal of Chemical Physics* **143**, 174701 (2015). eprint: https://doi.org/10.1063/1.4934918.

[108] H. T. Quang, A. Bachmatiuk, A. Dianat, F. Ortmann, J. Zhao, J. H. Warner, J. Eckert, G. Cunniberti, and M. H. Rümmeli. In Situ Observations of Free-Standing Graphene-like Mono- and Bilayer ZnO Membranes. *ACS Nano* **9**, 11408 (2015). eprint: https://doi.org/10.1021/acsnano.5b05481.

[109] H.-K. Hong *et al.* Atomic Scale Study on Growth and Heteroepitaxy of ZnO Monolayer on Graphene. *Nano Letters* **17**, 120 (2017). eprint: https://doi.org/10.1021/acs.nanolett.6b03621.

[110] C. Wang, S. Wang, S. Li, P. Zhou, J. Liang, and H. Wang. First Principles Study of Regulation of Monolayer ZnO and Vacancy Defects Equibiaxial Strain. *Journal of Superconductivity and Novel Magnetism* **35**, 925 (2022). eprint: https://doi.org/10.1007/s10948-021-06135-y.

[111] Y. Miao, Z. Wang, H. Zhao, Q. Chen, H. Wang, M. Wan, L. Chen, K. He, and Q. Wang. First principles studied tunable electronic and optical properties of 2D honeycomb ZnO monolayer engineered by biaxial strain and intrinsic vacancy. *Materials Science and Engineering B* **254** (2020). eprint: https://doi.org/10.1016/j.mseb.2020.114517.

[112] C. Tan, D. Sun, D. Xu, X. Tian, and Y. Huang. Tuning electronic structure and optical properties of ZnO monolayer by Cd doping. *Ceramics International* **42**, 10997 (2016). eprint: https://www.sciencedirect.com/science/article/pii/S0272884216303844.

[113] J. Lee, D. C. Sorescu, and X. Deng. Tunable Lattice Constant and Band Gap of Single- and Few-Layer ZnO. *The Journal of Physical Chemistry Letters* **7**, 1335 (2016). eprint: https://doi.org/10.1021/acs.jpclett.6b00432.

[114] M. Idrees, H. U. Din, S. U. Rehman, M. Shafiq, Y. Saeed, H. D. Bui, C. V. Nguyen, and B. Amin. Electronic properties and enhanced photocatalytic performance of van der Waals heterostructures of ZnO and Janus transition metal dichalcogenides. *Physical Chemistry Chemical Physics* **22**, 10351 (2020). eprint: `http://dx.doi.org/10.1039/D0CP01264E`.

[115] M. Topsakal, S. Cahangirov, E. Bekaroglu, and S. Ciraci. First-principles study of zinc oxide honeycomb structures. *Physical Review B* **80**, 235119 (2009). eprint: `https://link.aps.org/doi/10.1103/PhysRevB.80.235119`.

[116] J. Guo, C. Ke, Y. Wu, and J. Kang. Strain Engineering on the Electronic and Optical Properties of WSSe Bilayer. *Nanoscale Research Letters* **15** (2020). eprint: `https://doi.org/10.1186/s11671-020-03330-z`.

[117] S. Bertolazzi, J. Brivio, and A. Kis. Stretching and Breaking of Ultrathin MoS2. *ACS Nano* **5**, 9703 (2011). eprint: `https://doi.org/10.1021/nn203879f`.

[118] M. Sharma, A. Kumar, P. K. Ahluwalia, and R. Pandey. Strain and electric field induced electronic properties of two-dimensional hybrid bilayers of transition-metal dichalcogenides. *Journal of Applied Physics* **116**, 063711 (2014). eprint: `https://doi.org/10.1063/1.4892798`.

[119] H.-J. Jin, W. Y. Yoon, and W. Jo. Control of work function of MoS2 with ferroelectric polarization in honeycomb-like heterostructure. *Applied Physics Letters* **110**, 191601 (2017). eprint: `https://doi.org/10.1063/1.4983204`.

[120] T. Shinagawa and K. Takanabe. Towards Versatile and Sustainable Hydrogen Production through Electrocatalytic Water Splitting: Electrolyte Engineering. *ChemSusChem* **10**, 1318 (2017). eprint: `https://chemistry-europe.onlinelibrary.wiley.com/doi/pdf/10.1002/cssc.201601583`.

[121] K. A. Persson, B. Waldwick, P. Lazic, and G. Ceder. Prediction of solid-aqueous equilibria: Scheme to combine first-principles calculations of solids with experimental aqueous states. *Physical Review B* **85**, 235438 (2012). eprint: `https://link.aps.org/doi/10.1103/PhysRevB.85.235438`.

[122] A. K. Singh, L. Zhou, A. Shinde, S. K. Suram, J. H. Montoya, D. Winston, J. M. Gregoire, and K. A. Persson. Electrochemical Stability of Metastable Materials. *Chemistry of Materials* **29**, 10159 (2017). eprint: `https://doi.org/10.1021/acs.chemmater.7b03980`.

[123] A. M. Patel, J. K. Nørskov, K. A. Persson, and J. H. Montoya. Efficient Pourbaix diagrams of many-element compounds. *Physical Chemistry Chemical Physics* **21**, 25323 (2019). eprint: `http://dx.doi.org/10.1039/C9CP04799A`.

[124] E. A. Peterson, J. B. Haber, and J. B. Neaton. Superexchange-induced valley splitting in two-dimensional transition metal dichalcogenides: A first-principles study for rational design. *Physical Review B* **104**, 205421 (2021). eprint: `https://link.aps.org/doi/10.1103/PhysRevB.104.205421`.

[125] A. Srivastava, M. Sidler, A. V. Allain, D. S. Lembke, A. Kis, and A. Imamoglu. Valley Zeeman effect in elementary optical excitations of monolayer WSe_2. *Nature Physics* **11**, 141 (2015). eprint: https://www.nature.com/articles/nphys3203.

[126] G. Aivazian, Z. Gong, A. M. Jones, R.-L. Chu, J. Yan, D. G. Mandrus, C. Zhang, D. Cobden, W. Yao, and X. Xu. Magnetic control of valley pseudospin in monolayer WSe_2. *Nature Physics* **11**, 148 (2015). eprint: https://www.nature.com/articles/nphys3201.

[127] D. MacNeill, C. Heikes, K. F. Mak, Z. Anderson, A. Kormányos, V. Zólyomi, J. Park, and D. C. Ralph. Breaking of Valley Degeneracy by Magnetic Field in Monolayer $MoSe_2$. *Physical Review Letters* **114**, 037401 (2015). eprint: https://link.aps.org/doi/10.1103/PhysRevLett.114.037401.

[128] C. Zhao *et al.* Enhanced valley splitting in monolayer WSe_2 due to magnetic exchange field. *Nature Nanotechnology* **12**, 757 (2017). eprint: https://www.nature.com/articles/nnano.2017.68.

[129] D. Zhong *et al.* Van der Waals engineering of ferromagnetic semiconductor heterostructures for spin and valleytronics. *Science Advances* **3**, e1603113 (2017). eprint: https://advances.sciencemag.org/content/3/5/e1603113.

[130] T. Norden, C. Zhao, P. Zhang, R. Sabirianov, A. Petrou, and H. Zeng. Giant valley splitting in monolayer WS_2 by magnetic proximity effect. *Nature Communications* **10**, 4163 (2019). eprint: https://www.nature.com/articles/s41467-019-11966-4.

[131] K. Zollner, P. E. Faria Junior, and J. Fabian. Giant proximity exchange and valley splitting in transition metal dichalcogenide/hBN/(Co, Ni) heterostructures. *Physical Review B* **101**, 085112 (2020). eprint: https://link.aps.org/doi/10.1103/PhysRevB.101.085112.

[132] J. Qi, X. Li, Q. Niu, and J. Feng. Giant and tunable valley degeneracy splitting in $MoTe_2$. *Physical Review B* **92**, 121403 (2015). eprint: https://link.aps.org/doi/10.1103/PhysRevB.92.121403.

[133] Y. Ominato, J. Fujimoto, and M. Matsuo. Valley-Dependent Spin Transport in Monolayer Transition-Metal Dichalcogenides. *Physical Review Letters* **124**, 166803 (2020). eprint: https://link.aps.org/doi/10.1103/PhysRevLett.124.166803.

[134] X. Liang, L. Deng, F. Huang, T. Tang, C. Wang, Y. Zhu, J. Qin, Y. Zhang, B. Peng, and L. Bi. The magnetic proximity effect and electrical field tunable valley degeneracy in MoS2/EuS van der Waals heterojunctions. *Nanoscale* **9**, 9502 (2017). eprint: http://dx.doi.org/10.1039/C7NR03317F.

[135] D. Zhong *et al.* Layer-resolved magnetic proximity effect in van der Waals heterostructures. *Nature Nanotechnology* **15**, 187 (2020). eprint: https://www.nature.com/articles/s41565-019-0629-1.

[136] Z. Zhang, X. Ni, H. Huang, L. Hu, and F. Liu. Valley splitting in the van der Waals heterostructure WSe_2/CrI_3: The role of atom superposition. *Physical Review B* **99**, 115441 (2019). eprint: https://link.aps.org/doi/10.1103/PhysRevB.99.115441.

[137] W. J. Schutte, J. L. De Boer, and F. Jellinek. Crystal structures of tungsten disulfide and diselenide. *Journal of Solid State Chemistry* **70**, 207 (1987). eprint: https://www.sciencedirect.com/science/article/pii/0022459687900570.

[138] I. Sosnowska, W. Schäfer, W. A. Kockelmann, and I. O. Troyanchuk. Neutron Diffraction Studies of the Crystal and Magnetic Structures of $BiMn_xFe_{1-x}O_3$ Solid Solutions. *Materials Science Forum* **616**, 378 (2001).

[139] T. Cao *et al.* Valley-selective circular dichroism of monolayer molybdenum disulphide. *Nature Communications* **3**, 887 (2012). eprint: https://www.nature.com/articles/ncomms1882.

[140] D. Xiao, G.-B. Liu, W. Feng, X. Xu, and W. Yao. Coupled Spin and Valley Physics in Monolayers of MoS_2 and Other Group-VI Dichalcogenides. *Physical Review Letters* **108**, 196802 (2012). eprint: https://link.aps.org/doi/10.1103/PhysRevLett.108.196802.

[141] Q. Zhang, S. A. Yang, W. Mi, Y. Cheng, and U. Schwingenschlögl. Large Spin-Valley Polarization in Monolayer $MoTe_2$ on Top of EuO(111). *Advanced Materials* **28**, 959 (2016). eprint: https://onlinelibrary.wiley.com/doi/abs/10.1002/adma.201502585.

[142] P. W. Anderson. New Approach to the Theory of Superexchange Interactions. *Physical Review* **115**, 2 (1959). eprint: https://link.aps.org/doi/10.1103/PhysRev.115.2.

[143] G. D. Mahan. *Many-Particle Physics*. Plenum Press, (1981).

[144] C. Ederer and N. A. Spaldin. Weak ferromagnetism and magnetoelectric coupling in bismuth ferrite. *Physical Review B* **71**, 060401 (2005). eprint: https://link.aps.org/doi/10.1103/PhysRevB.71.060401.

[145] R. A. Murphy *et al.* Exchange Bias in a Layered Metal-Organic Topological Spin Glass. *ACS Central Science* **7**, 1317 (2021). eprint: https://doi.org/10.1021/acscentsci.1c00568.

[146] R. Moessner and A. Ramirez. Geometrical frustration. *Physics Today* **59**, 24 (2006). eprint: https://doi.org/10.1063/1.2186278.

[147] E. Lachman, R. A. Murphy, N. Maksimovic, R. Kealhofer, S. Haley, R. D. McDonald, J. R. Long, and J. G. Analytis. Exchange biased anomalous Hall effect driven by frustration in a magnetic kagome lattice. *Nature Communications* **11** (2020). eprint: https://doi.org/10.1038/s41467-020-14326-9.